MAX PLANCK INSTITUTE FOR POLYMER RESEARCH

JOHANNES GUTENBERG UNIVERSITÄT MAINZ

Degradation and Device Physics of Organic Light-Emitting Diodes

Kumulative Dissertation

zur Erlangung des Grades

"Doktor der Naturwissenschaften"

am Fachbereich Physik, Mathematik und Informatik

der Johannes Gutenberg-Universität

in Kooperation mit

dem Max-Planck-Institut für Polymerforschung

in Mainz

Theun Sebastiaan van der Zee

Geboren in Drachten,

Mainz, 2022

Tag der mündlichen Prüfung:

Hauptreferent: Prof. Paul W. M. Blom

Korreferent: Prof. Dr. Jairo Sinova

Abstract

The success story of organic light-emitting diodes (OLEDs) has led to today's multi-billion market that is based around its display technology. Despite OLEDs being an established technology, there is continuous innovation and drive to find new emitters, since commercial OLEDs left us with a significant drawback: the use of an environmentally unfriendly heavy-metal dopant. The most promising research effort to overcome this is a class of materials known as thermally activated delayed fluorescence (TADF) emitters. They, instead of a heavy-metal, use thermal energy to attain high efficiencies.

It goes to show that the commercial as well as the research interest in OLEDs is still highly active, but for established polymer LEDs (PLEDs) and new and emerging TADF emitters alike, several unsolved issues exist. Two core challenges are the emitter degradation under electrical driving and the decrease in efficiency at higher brightness (commonly known as 'roll-off'). In order to tackle these aforementioned problems, an understanding of the degradation physics as well as OLED device physics is indispensable. The focus of this thesis lies exactly there, often aided by numerical modelling we aim to gain a deeper fundamental understanding about OLED degradation and the device physics of OLEDs, the latter mostly in relation to the roll-off of TADF OLEDs.

The root causes of both degradation and roll-off are often linked to interactions involving excitons. Manipulating excitons is thus key, which is what chapter 3 of this thesis shows in the context of PLED degradation and efficiency. By systematically varying exciton populations it is observed that from the two types of excitons, triplets are the ones responsible for the degradation of PLEDs through their interaction with charge carriers. Furthermore, we are able to quantify bimolecular annihilation effects in operating PLEDs.

Before turning our attention to the degradation of TADF OLEDs, first the device operation in the undegraded state should be properly understood. In chapter 4 we develop an analytical formula for the efficiency of a TADF OLED. We show the applicability of our formulas, and how straightforward analytical theory can be used to prove that the bimolecular annihilation between triplets is the dominant contribution to the roll-off.

With the new insight regarding the roll-off we continue in chapter 5 to construct a full numerical device model for TADF OLEDs, which will greatly aid in understanding the device operation. We validate our model against a practically ideal TADF emitter and show that we are able to describe the full operation of a TADF OLED.

The device model allows us to now quantitatively study the degradation of TADF OLEDs. In chapter 6 we investigate the degradation characteristics and by employing our recently constructed device model we find that triplet-charge interactions are the driving force behind the degradation of TADF OLEDs.

Zusammenfassung

Die Erfolgsgeschichte der organischen Leuchtdioden (OLEDs) hat zu dem heutigen Milliardenmarkt geführt, der auf ihrer Display-Technologie basiert. Obwohl OLEDs eine etablierte Technologie sind, gibt es kontinuierliche Innovationen und Bestrebungen, neue Emitter zu finden, da die bereits kommerziell erhältlichen OLEDs einen erheblichen Nachteil aufweisen: Diese verwenden ein umweltschädliches Schwermetall als Dotierungsmittel. Die vielversprechendste Forschungsanstrengungen, um diese zu ersetzen, ist eine Klasse von Materialien, die als Emitter mit thermisch aktivierter, verzögerter Fluoreszenz (TADF) bekannt sind. Diese nutzen thermische Energie anstelle eines Schwermetalls, um hohe Wirkungsgrade zu erreichen.

Sowohl das kommerzielle als auch das Forschungsinteresse an OLEDs ist immer noch sehr hoch, aber im Falle der etablierten Polymer-LEDs (PLEDs) als auch für neue und aufkommende TADF-Emitter gibt es mehrere ungelöste Probleme. Zwei zentrale Herausforderungen sind der Emitterabbau (Degradation) bei elektrischem Betrieb und die Abnahme der Effizienz bei höherer Helligkeit (allgemein bekannt als „Roll-off“). Um diese oben genannten Probleme in Angriff nehmen zu können, ist ein genaueres Verständnis der Physik des Emitterabbaus sowie der OLED-Geräte unerlässlich. Der Fokus dieser Arbeit liegt genau dort, oft unterstützt durch numerische Modellierung wollen wir ein tieferes, grundlegendes Verständnis über die OLED-Degradation und die Gerätephysik von OLEDs gewinnen, letzteres hauptsächlich in Bezug auf den Roll-Off-Effekt von TADF-OLEDs.

Die Hauptursachen sowohl für die Degradation als auch für den Roll-off-Effekt stehen meistens im Zusammenhang mit Wechselwirkungen, an denen Exzitonen beteiligt sind. Die Manipulation von Exzitonen ist daher der Schlüssel für ein tiefer gehendes Verständnis der vorliegenden Prozesse, was in Kapitel 3 dieser Arbeit im Kontext von PLED-Degradation und -Effizienz gezeigt wird. Durch systematische Variation der Exzitonenpopulationen wird beobachtet, dass von den beiden Arten von Exzitonen Tripletts diejenigen sind, die für die Degradation von PLEDs durch ihre Wechselwirkung mit Ladungsträgern verantwortlich sind. Darüber hinaus sind wir in der Lage, bimolekulare Auslöschungseffekte beim Betrieb von PLEDs zu quantifizieren.

Bevor wir uns der Degradation von TADF-OLEDs zuwenden, sollte zunächst der Gerätebetrieb im nicht degradierten Zustand richtig verstanden werden. In Kapitel 4 entwickeln wir eine analytische Formel für die Effizienz einer TADF-OLED. Wir zeigen die Anwendbarkeit unserer Formeln und wie einfache analytische Theorie verwendet werden kann, um zu beweisen, dass die bimolekulare Vernichtung zwischen Tripletts der dominierende Beitrag zum Roll-off-Effekt ist.

Mit der neuen Einsicht in Bezug auf den Roll-off-Effekt fahren wir in Kapitel 5 fort, ein vollständiges numerisches Gerätemodell für TADF-OLEDs zu konstruieren, das das Verständnis des Gerätebetriebs erheblich unterstützen wird. Wir validieren unser Modell gegen einen praktisch idealen TADF-Emitter und zeigen, dass wir in der Lage sind, den vollständigen Betrieb einer TADF-OLED zu beschreiben.

Das Gerätemodell ermöglicht es uns nun, die Degradation von TADF-OLEDs quantitativ zu untersuchen. In Kapitel 6 untersuchen wir die Degradationseigenschaften und finden unter Verwendung unseres kürzlich konstruierten Gerätemodells heraus, dass Triplett-Ladungs-Wechselwirkungen die treibende Kraft hinter der Degradation von TADF-OLEDs sind.

Table of contents

Chapter 1: Introduction

This chapter introduces the reader to the basic concepts in the fascinating field of organic semiconductor physics, with a focus on organic light-emitting diodes (OLEDs). It will become clear that organic semiconductors show, in terms of physics, remarkable differences to what is found in their classical inorganic counterparts. This chapter will provide the knowledge that further chapters in this thesis build on, but it is written to be more comprehensive than that, giving context and more detailed explanations about various core ideas.

1.1 General background

OLEDs have become an indispensable part of our everyday life as numerous commercial products such as smartphones and televisions rely on its display technology. As scientists today we can draw upon a wealth of knowledge coming from over 60 years of research, ever since Pope et al. fabricated in 1963 a direct-current-driven OLED using anthracene as light-emitting material.[1] That OLED was driven at >100 Volts, still far from sufficient for commercial applications. Development of OLEDs really took off after the first evaporated small molecule OLED by Tang and Van Slyke in 1987.[2] An OLED based on conjugated polymers was demonstrated only three years later, in 1990.[3] Both laid the foundation for the 'first generation' of OLEDs, where light is generated solely through fluorescence. A major boost in OLED efficiency came in 1998, when for the first time heavy metal complexes were used to generate light via phosphorescence. [4,5] OLEDs based on this principle belong to the second generation and almost all commercially available OLEDs today fall into this class. In 2012 the scientific interest in OLEDs was renewed due to the demonstration of highly efficient OLEDs, without the use of an additional heavy metal dopant.[6,7] Instead, this third OLED generation relies on the mechanism of 'thermally activated delayed fluorescence' (TADF), and they are seen as candidates for next generation display applications. Although OLEDs are commercially the most successful product,[8] organic semiconductors have been used in various other disciplines like organic photovoltaics (OPV),[9] organic field-effect transistors (OFETs),[10] and more recently organic thermoelectrics (OTEs).[11,12]

1.2 The interest and material classes in organic electronics

Organic electronics present an interesting alternative to the well-established inorganic semiconductor technology. Organic atoms such as carbon and hydrogen are used as building blocks for molecules that exhibit semiconducting properties. The materials used for organic electronics are commonly divided into two classes: *conjugated polymers* and *small molecules*, each with their own benefits and drawbacks. I shortly will outline the place of these two classes in the context of OLEDs, after giving a general introduction into the theory behind conjugation.

1.2.1 An introduction to conjugation

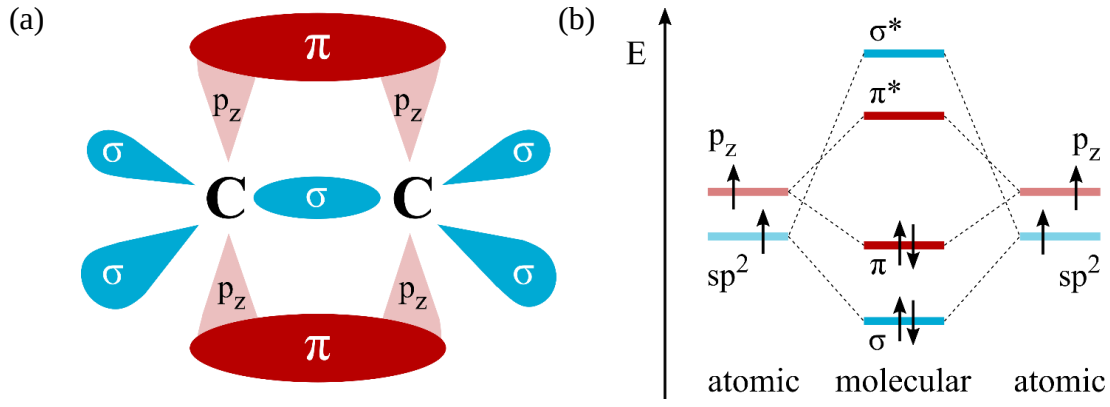

Figure 1.1: (a) schematic of the orbitals in ethene, where for clarity the hydrogen atoms are omitted. (b) Bonding between the two carbon atoms in ethene depicted in an energy level diagram. ↑ and ↓ represent electrons. Modified from reference.[13]

Many parts, or in Greek, *polymers* are chains of a repeating monomer units. The class that show semiconducting properties are called *conjugated polymers*. The backbone of a conjugated polymer consists mainly out of carbon and hydrogen atoms, but other common building blocks include various low atomic number elements like nitrogen (N), oxygen (O) and sulphur (S). To illustrate bond formation in a conjugated polymer let's consider a small fragment, namely the homonuclear diatomic molecule ethene (C_2H_4). A carbon atom, with a coordination number of four, has in the case of ethene three electrons in sp^2 hybridized *atomic* orbitals which form σ-/σ*-bonds with other carbon and hydrogen atoms, as illustrated in figure 1.1(a) & (b). These shared *molecular* orbitals are commonly referred to as the bonding (σ) and anti-bonding (σ*) orbitals.[14] Looking at this from a quantum mechanical perspective, the wavefunction of an electron in an atomic orbital can be found by solving the time independent Schrödinger equation. When moving from atomic to molecular orbitals, one can approximate the molecular orbitals as a linear combination of atomic orbitals (LCAOs).[15] This leads to constructive or destructive interference between the two atomic wavefunctions. The enhancement/reduction in electron density between the two nuclei results in a bonding or anti-bonding orbital respectively. The time independent Schrödinger equation is given by:

$$\hat{H}\psi = \hat{H}E. \tag{1.1}$$

Here the wavefunction (ψ) is a function of the electronic coordinates ($\vec{r}$) as well as the nuclear coordinates ($\vec{R}$): $\psi = \psi_{el}(\vec{r}, \vec{R})$. $\hat{H}$ is the Hamiltonian, which is a function of both the potential and kinetic energy of the system, and E are the energy eigenstates. The energy includes Coulombic attraction between the nucleus and electron on the other atom, it also includes the extent of the overlap of the two wavefunctions, plus it contains the exchange interaction.[13,15] The exchange interaction is the interaction between one nucleus and the combined electron density of the two electrons resulting from wavefunction overlap. The energy splitting between bonding and antibonding orbitals is mainly determined by this exchange interaction and the splitting therefore scales with the overlap between the electron wavefunctions.

The σ-bonds lay in-plane and configure themselves as in an equilateral triangle. This leaves one free electron per carbon atom to occupy a p_z orbital, which lies out-of-plane, perpendicular to the sp^2 hybrid orbitals (fig. 1.1 (a)). Electrons from the p_z-orbital form π-/π*-bonds, but since the overlap electron density is further from the nucleus, the exchange energy between electrons in the p_z-orbitals is lower than for electrons in the sp^2 hybrid orbitals and therefore the splitting between the π-/π*-bonds is reduced compared to the σ-/σ*-bonds, as depicted in figure 1.1(b) The conjugation in a polymer arises from the mutual overlap of the π-bonds, and it is these delocalized π-bonds that govern many of a conjugated polymer's fascinating properties like charge carrier conduction and their interaction with light.

Early developed models viewed a conjugating polymer as a 1D chain of atoms,[16] however this is very often a too restricted view. More realistically the polymer contains kinks and defects

such that the conjugation does not extent over the whole chain, but there are conjugated segments.[17]

In the ground state, all bonding orbitals are filled up until the frontier orbital. The frontier orbital in a delocalized π-band is named the highest occupied molecular orbital (HOMO), whereas for a π*-band this energy level is called the lowest unoccupied molecular orbital (LUMO), the energy splitting between the two being the electrical bandgap. A typical electrical bandgap amounts to ~1.5 to 3 eV for organic semiconductors, subtracting the exciton binding energy (~0.4 eV) one arrives at the optical bandgap,[18] meaning that emission $\left(E = \frac{hc}{\lambda}\right)$ is generally in the visible range. Note that the HOMO and LUMO bear similarities to the classical valence and conduction band from inorganic semiconductor physics.

1.2.2 Light-emitting conjugated polymers and small molecules

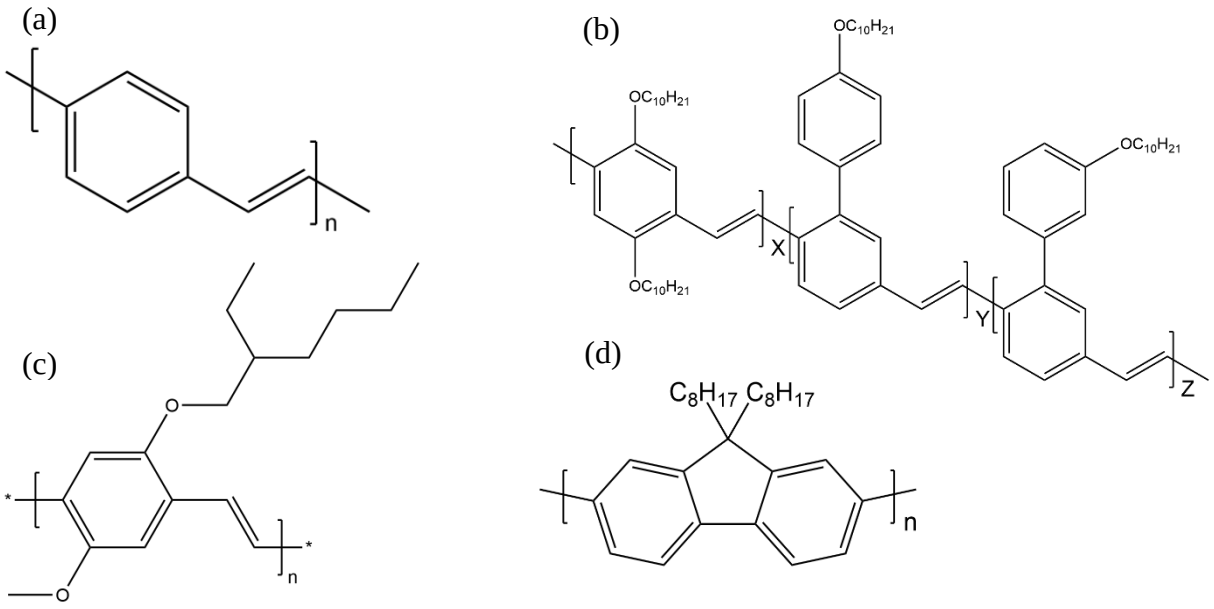

Figure 1.2: Examples of light emitting polymers.

In early stages, light-emitting polymers started out as (a combination of) aromatic hydrocarbons (e.g. benzene) and hydrocarbon chains (e.g. ethene), leading to polymers such as poly-phenylene vinylene (PPV), for which the chemical structure is presented in figure 1.2(a). PPV is the polymer that was used in the first polymer LED (PLED).[3] The opto-electronic properties of the PPV class polymers were later enhanced through the incorporation of various sidechains, leading to for example MEH-PPV and SY-PPV,[19,20] both well-studied red- and yellow-emitting polymers respectively (figure 1.2(b) & (c)). Compared to bare PPV, the added alkoxy sidechains of MEH-PPV and SY-PPV enhance solubility in organic solvents. An example of a well-studied blue-emitting polymer is polyfluorene (PFO), its chemical structure is in figure 1.2(d).[21] These three polymers became 'workhorse' polymers, and they allowed for the elucidation of the majority of the device physics in 1st generation PLEDs.

The benefits of conjugated polymers are numerous. The opto-electronic properties of a polymer allow for extensive customization in a straightforward way through the modification of the chemical structure, in particular through variation of their side chains. Furthermore, their non-rigid structure makes them suitable for processing in various organic solvents like toluene and chlorobenzene. Solution processing allowing for easy-to-use deposition techniques like bar- or spin-coating, and opens the possibility to use flexible substrates. In short, polymers combine low-cost with facile and large area fabrication.[22]

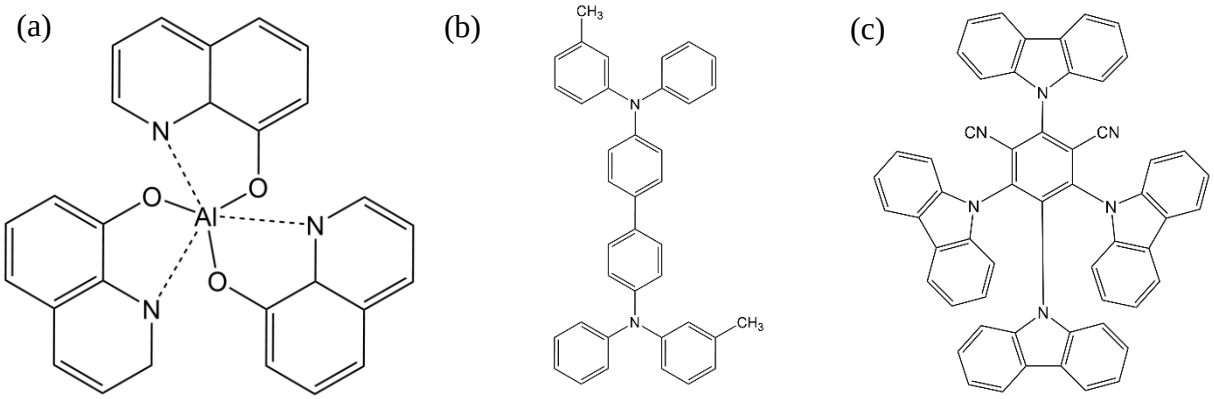

Figure 1.3: Examples of small molecules used in OLEDs.

Like conjugated polymers, small molecule organic semiconductors can form a conjugated system as well. Due to their lower size, however, the preferred deposition technique is no longer spin-coating, but thermal evaporation. This generally produces more ordered morphologies as compared to spin-coating, which is beneficial for charge transport. However, evaporating is also more expensive, fabrication wise more demanding and the requirement to do it under high-vacuum makes it less suitable for larger areas.

That didn't stop small molecule OLEDs from finding success however. The first OLED was made up out of a combination of two small molecules, namely Alq_3 and TPD (figure 1.3(a) & (b).[2] Also most 2nd and 3rd generation OLEDs use small molecules as an active layer, e.g. 4CzIPN (figure 1.3 (c)) is a well-studied TADF material.[7]

1.3 Charge transport in organic semiconductors

Charge transport in organic semiconductors is fundamentally different to what is found in classical inorganic crystals. Since molecular materials are used to transport charge, there is an intricate link between the transport and the underlying structure of the molecule as well as the molecular packing in the solid state.[23–25] Organic semiconductors are disordered, such that when going form crystalline inorganic semiconductors to amorphous organic semiconductors, the conduction and valance band are replaced by a density of states (DOS) that follow a Gaussian distribution in order to reflect the inherent randomness in the semiconducting material.[26,27] The Gaussian formula ($g(x)$), with an energy (ε) below the middle, is given by:

$$g(x) = \frac{1}{\sqrt{2\pi\sigma^2}} exp\left(-\frac{\epsilon}{2\sigma^2}\right). \quad (1.2)$$

The energetically distributed transport sites are linked to the concept of disorder through the width of the Gaussian DOS (σ). I will present a general introduction into hopping transport followed by a description of the mobility model used in this work.

1.3.1 Hopping transport

The low dielectric constant of $\varepsilon \approx 3$ found in molecular semiconductors means columbic effects and electron interactions play a role in the charge transport, whereas for inorganic crystals the high dielectric screening ensures that carriers are effectively free at room temperature.[13] Strong covalent bonding holds the lattice of an inorganic semiconductor together, resulting in delocalized Bloch electrons.[28] This is in stark contrast to the much weaker van der Waals interactions that are found between organic molecules. Strong orbital interactions producing well defined and broad bands are thus absent in organic semiconductors, which drastically shortens the carrier's mean free path and makes carriers localized in specific energy states. Transport between localized sites requires wavefunction overlap and it proceeds via a *hop* of one site to the next (schematically depicted in figure 1.4, to the right), which is mediated by phonons.[29,30] In conjugated polymers this hopping transport is a combination of inter- and intra-chain hopping between conjugated segments.[31] The localization in organic semiconductors means carriers are thus not 'free', as in the classical sense, which is reflected in a much lower mobility (μ, [$cm^2/m^2\ V^{-1}\ s^{-1}$]). The room temperature mobility of silicon (Si) is around 1000 $cm^2\ V^{-1}\ s^{-1}$ at relevant doping concentrations.[32] In contrast, high mobility organic semiconductors show values of $\mu \approx$ 1-20 $cm^2\ V^{-1}\ s^{-1}$,[23] which is often connected with their crystalline-like stacking behaviour. The transport in high mobility organic semiconductors show localization effects, but on short timescales only.[33,34] The bulk mobility (at no electric field/no charge carrier density) of most organic semiconductors used for OLEDs however is well below this, on the order of 10^{-7}-10^{-4} $cm^2\ V^{-1}\ s^{-1}$,[35–37] meaning we are dealing fully with localized transport.

In early developed models the localization is brought about by a local distortion of the surrounding atoms as a response to the addition of a charge carrier.[38] The quasi-particle associated with the carrier and the surrounding distorted environment is named a 'polaron'.[39] Following Emin's formulation,[39] we encounter only small polarons in the organic semiconductors used in this thesis, i.e. polarons with a small spatial extent. Note that the terms (charge) carrier and polaron are used interchangeably in this thesis. The existence of a polaron requires a (strong) coupling between electrons and phonons and the disorder that originates solely from the deformation of the lattice due to this coupling is sometimes referred to as 'dynamic disorder'.[40] When an electron moves from one site to the next there is an adjustment in bond lengths since the electron distribution changes, so in the polaron picture the distortion moves with the carrier.[13] In pure polaronic transport the distortion is connected to the geometric relaxation energy (λ) the two sites have to undergo.[13] Although polaronic models found some success, it is agreed upon that they are unable to fully explain the charge transport in organic semiconductors.

The kinks and defects in the microenvironment of organic semiconductors give rise to disorder as well, and this morphological disorder is often referred to as 'static disorder'.[27] With the assumption of weak electron-phonon coupling, Miller and Abrahams proposed an elegant equation for the transition rate of hopping (W_{ij}) from initial site *i* to final site *j* with energies ε_i and ε_j respectively:[41]

$$W_{ij} = \nu_0 exp(-2\alpha R_{ij}) \begin{cases} exp\left(-\frac{\varepsilon_j - \varepsilon_i}{k_B T}\right), & \varepsilon_j \geq \varepsilon_i \\ 1 \quad . & \varepsilon_j < \varepsilon_i \end{cases} \tag{1.3}$$

Where ν_0 is the attempt to hop frequency, α the inverse localization length and R_{ij} the physical distance between the two sites. The first term in equation (1.3) captures the decrease of the wave function overlap with increasing distance whereas the second term accounts for the temperature dependence of jumps upward in energy. Although not used in this work, I would like to mention that for larger electron-phonon couplings the semi-classical Marcus expression can be used to describe the hopping rates, which uses the geometric relaxation energy as input parameter.[42] A noticeable difference between the Miller-Abrahams (MA) and Marcus hopping rate is that for $\varepsilon_i > \varepsilon_j$ (downward hopping) the MA rate is always constant, whereas the Marcus rate decreases when the energy difference becomes larger than the reorganization energy, which is known as the 'Marcus inverted regime'. Recently, a full quantum treatment of the charge carrier hopping applied to a series of amorphous molecules showed that the simpler MA rates provide a good description of the mobility in organic semiconductors nonetheless.[43] Neglecting polaronic effects has been found experimentally and proven theoretically, for a discussion on this, the reader is referred to the following reference.[27]

The ability of organic semiconductors to transport charges is generally not given in terms of a hopping rate, rather it is given by the mobility. The mobility is an important metric to optimize since it affects, amongst other things, the maximum sustainable current in an OLED and the recombination of holes and electrons that produces light.[44] We will explore the mobility of organic semiconductors more in depth in the next paragraph.

1.3.2 Extending the Gaussian Disorder Model

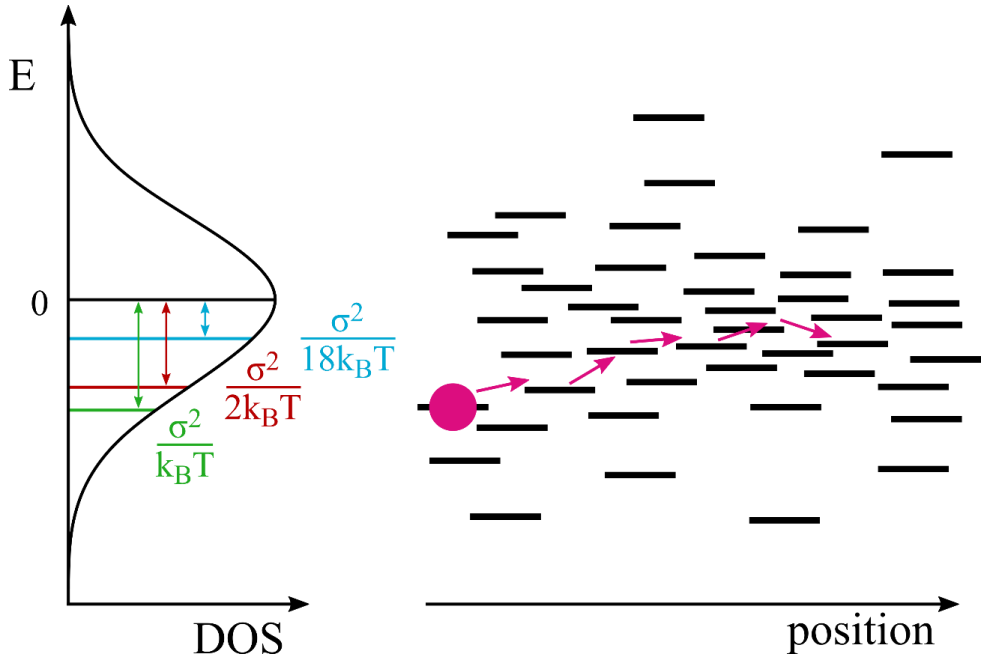

Figure 1.4: Hopping in a Gaussian DOS. Gaussian DOS of the material (left) with the relevant energy levels. These coloured energy levels lie at a certain spacing below the middle of the DOS. The spacing between the middle of the DOS and the relevant energy level is colour coded and corresponds to the corresponding expression $\frac{\sigma^2}{xk_BT}$, $x = [1,2,18]$, of the same colour. The process of hopping conduction is schematically depicted to the right.

Using MA hopping rates and a Gaussian distribution with uncorrelated energy sites, Bässler carried out Monte Carlo simulations to obtain a theoretical expression for the mobility:[45]

$$\mu = \mu_\infty \exp\left[-\left(\frac{2}{3}\hat{\sigma}\right)^2\right]\begin{cases} exp\left[C(\hat{\sigma}^2 - \Sigma^2)\sqrt{E}\right]; & \Sigma \geq 1.5, \\ exp\left[C(\hat{\sigma}^2 - 2.25)\sqrt{E}\right]; & \Sigma < 1.5. \end{cases} \quad (1.4)$$

E is the electric field strength, $\hat{\sigma} \equiv \frac{\sigma}{k_BT}$, Σ is the amount of positional disorder and μ_∞ is the mobility in the infinite temperature limit. An important consequence of using a Gaussian DOS is that most carriers that contribute to the transport will centre on a level $E_a = \frac{\sigma^2}{2k_BT}$ below the middle of the DOS (E_0),[46] which is the result of a trade-off. On the one hand a carrier would like to lose its energy and relax to the equilibrium level $\frac{\sigma^2}{k_BT}$ below the middle of the DOS.[45] In the tail of the DOS however there are fewer states with the same energy, meaning the average distance between energetically equal sites increases. Furthermore, hopping to other states is more likely to be upward in energy. Looking at equation (1.3) we see that both factors would decrease the average hopping rate. On the other hand, in order to be effectively transported through the material, carriers would like to be at the transport energy located $\frac{\sigma^2}{18k_BT}$ below the middle of the DOS, where there are plenty of states available. From the statistics between free and trapped carriers it was deduced that a compromise is found at $\frac{\sigma^2}{2k_BT}$, and consequently the

temperature activation comes from the jump that carriers have to make to the transport level,[46,47] as is schematically depicted on the left side of figure 1.4.

Equation (1.4) directly shows us features of hopping transport that can be experimentally verified by measuring the mobility. Focusing on the temperature dependence first, we see that the temperature activation manifests itself in the mobility through $\ln \mu \propto \frac{1}{T^2}$, a totally different situation compared to what is found in inorganic semiconductors, where freezing out phonon vibrations causes the mobility to increase when the temperature decreases. The temperature dependence reflects that E_a shifts into the tail of the DOS with decreasing temperature, making the jump upwards in energy to the transport level increasingly more difficult. Next to the temperature dependence we see a field-dependent mobility scaling given by:

$$\mu \propto exp\left(\sqrt{E}\right). \tag{1.5}$$

This electric field dependence is a signature of hopping in a Gaussian DOS, but interestingly the same dependence on E was found experimentally already before and described by the empirical Poole-Frenkel mobility:

$$\mu_{PF} = \mu_0 \exp\left(\gamma * \sqrt{E}\right). \tag{1.6}$$

With μ_0 being the zero-field mobility and γ an empirical parameter to describe the field activation. The Poole-Frenkel formula was, for example, often used to explain mobilities found via Time-of-Flight (TOF) experiments.[44]

One important point that is overlooked in Bässler's Gaussian Disorder Model (GDM) is the dependence of the mobility on the charge carrier density (n for electrons, p for holes, both [m^{-3}]).[48,49] Filling the DOS with more charges results on average in a smaller separation between the carrier's energy and the transport energy, which is reflected in a higher hopping rate and concomitantly a higher mobility. This explained for example the apparent mobility enhancement in thin organic diodes (<100 nm), where diffusion of charges from the contacts increases the average carrier density and thereby the mobility.[50] It also explained the discrepancy between the apparent mobility found in OLEDs versus OFETs, as the charge carrier density in OFETs tends to be orders of magnitude higher.[48]

Including the effect of the mobility on temperature T [K], electric field strength E [eV] and n/p, one arrives at the Extended Gaussian Disorder Model (EGDM) developed by Pasveer et al. and used throughout this thesis.[51] The mobility is parameterized by three fit parameters: μ_0 [$m^2 V^{-1} s^{-1}$] is a prefactor reflecting the electronic coupling, σ [eV] is the disorder that mostly controls the temperature dependence and a [nm] the average hopping distance that mostly influences the electric field dependence. When considering a conjugated polymer, 'average' here reflects the average between inter- and intra-chain hopping. The density- and field-dependence are split up into separate formulas since the two are uncorrelated at not extremely high fields and densities. The EGDM description of the mobility is given as:[51]

$$\mu_n(T, n, E) \approx \mu_n(T, n) f(T, E), \tag{1.7}$$

$$\mu_n(T,n) = \mu_0(T) exp\left[\frac{1}{2}(\hat{\sigma}^2 - \hat{\sigma})(2na^3)^{\delta}\right]. \quad (1.8a)$$

With:

$$\mu_0(T) = \mu_0 c_1 exp[-c_2\hat{\sigma}^2], \quad (1.8b)$$

$$\delta = 2\frac{\ln(\hat{\sigma}^2 - \hat{\sigma}) - \ln(\ln 4)}{\hat{\sigma}^2}, \quad (1.8c)$$

$$f(T,E) = exp\left\{0.44\left(\hat{\sigma}^{3/2} - 2.2\right)\left[\sqrt{1 + 0.8\left(\frac{Eqa}{\sigma}\right)^2} - 1\right]\right\}. \quad (1.9)$$

The constant c_1 is 1.8x10^{-9} and c_2 is 0.42, $\mu_0(T)$ is the mobility in the zero-field and zero-carrier density limit. The above equations for the EGDM are for electrons, naturally, the equations used for holes are obtained by replacing *n* by *p*. At low densities the $\ln \mu \propto \frac{1}{T^2}$ scaling is found, however, for sufficient charge carrier densities that start to fill up the DOS, the temperature scaling modifies to $\ln \mu \propto \frac{1}{T}$, an Arrhenius behaviour.[52–54] The EGDM predicts the charge carrier density dependence dominates at room temperature, whereas at lower temperatures and at high fields the field dependence becomes important.[49,51] The EGDM has successfully described the mobility a wide array of organic semiconductor materials, and it was found to be in good agreement with more complex models.[49,55–63]

With the theoretical description of the mobility done, let's discuss the device structure needed to characterize the mobility of each charge carrier species in a reliable way.

1.4 Single carrier devices

It is important to characterize hole and electron transport separately from each other, but their individual contribution is hard to discern from a double carrier device like an OLED, where both electrons and holes are injected simultaneously. Thus we turn to single carrier devices, for which I will discuss their design and device characteristics in this section, making the link between the current and mobility.

1.4.1 Hole only and electron only device design

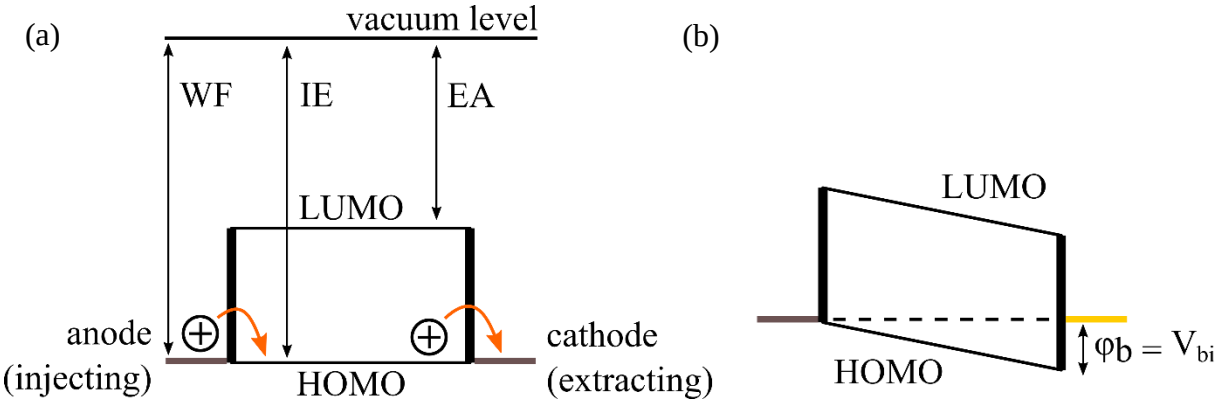

Figure 1.5: Schematic symmetric HO (a) and asymmetric HO (b) device design. In the symmetric HO the injection and extraction of holes into the HOMO is depicted, whereas in the asymmetric HO an injection barrier is shown. All acronyms are explained in the text.

Ensuring that effectively only one carrier species is present in the organic material requires some engineering as to which electrode materials to use. As a first design rule, the work function (WF) of both the metal electrodes, i.e., the energy required to liberate a carrier from a solid into vacuum, should align either with the HOMO or LUMO of the organic material. Matching or having even higher electrode WFs than the HOMO on both sides of the semiconductor leads to efficient hole injection and extraction, while at the same time the large injection barrier to the LUMO ensures that practically no electrons are present in the device (see figure 1.5(a)). Of course, which electrode is classified as 'injecting' and which one as 'extracting' depends on the direction of the applied electric field. In figure 1.5(a) the WF matches the ionization energy (IE), which is the energy required to liberate an electron from the HOMO to the vacuum level, but of course this does not have to be the case, for example when an injection barrier is present (figure 1.5(b)). Analogously the energy to liberate an electron from the LUMO into vacuum is the electron affinity (EA). Such a 'hole-only' (HO) device requires materials (metals) with a high WF: ITO, Au or transition metal oxides like MoO_3 are popular.[35,64] Similarly, an 'electron-only' (EO) device (not shown) uses low WF materials (metals) like Ba, LiF or Ca to inject electrons in the LUMO.[36] The full device is almost always made on glass for support and with an aluminium capping layer to ensure good contact to the measurement setup. How to fabricate single carrier devices is outlined in methods section 2.3.

Two Ohmic contacts result in no rectifying properties, but often one of the contacts is non-Ohmic due to different WFs of the two electrodes. One electrode can have a lower (higher) WF than the HOMO (LUMO), resulting in an injection barrier (φ_b) on one side of the device (figure 1.5(b)). A contact with a barrier automatically results in a difference between the WF of the metal and the IE of the HOMO (in case of a HO). In the case of a barrier it is thermodynamically favourable to align the chemical potential through the device, which results in a build-in voltage (V_{bi}) that needs to be overcome before effectively injecting charge.

1.4.2 Injection from metals into organic semiconductors

Charge carriers are not generated intrinsically in OLEDs, in fact, the intrinsic carrier concentration is very low, because of the significant bandgap, and they are overshadowed by extrinsically generated charges such as by injection in OLEDs or photo generation in OPVs.[13] Efficient charge injection is thus a prerequisite to a well-functioning OLED. For injection (and extraction) we always strive to obtain Ohmic contacts, which means that the device current is limited by the number of carriers that the material can sustain and transport, not by what the electrodes can inject.

Matching WFs of the electrode to the HOMO/LUMO of the organic semiconductor comes close, but does not provide a fully Ohmic contact. When the organic semiconductor comes in contact with the metal electrode, charge transfer across the interface occurs to establish equilibrium of the chemical potential.[65–67] In addition, other rearrangements of charge at the interface, including those coming from chemical reactions between the metal and the organic, can lead to additional dipoles at the interface.[68] The charges that transfer from the metal into the organic layer get transferred into the tail states of the DOS first, leading to pinning of the Fermi level to these states that extent into the bandgap.[69,70] The film formation in the first few nanometers depends heavily on the preparation conditions of the metal/semiconductor contact,[70] thus it has even been suggested that the DOS near the interface is different from the bulk DOS.[67] The combined result is that the potential at the interface is shifted into the bandgap and away from the bulk potential, such that the bending of the potential energy bands effectively forms an injection barrier. This band bending effect (although strictly speaking there are no bands present here) will extend over a few nm into the organic layer and generally amounts to 0.3-0.4 eV.[65,69] Band bending will reduce V_{bi}, such that V_{bi} is not simply the difference in work function between the two electrodes (ΔWF) , but given by $V_{bi} = \Delta WF - b$, with b the band bending parameter.[71] There is one more related effect I would like to mention, namely the transferred charges interact with their attractive image charge in the metal, as in the classical Richardson-Schottky model.[32] The image force tends to draw the electrons back into the metal, effectively rounding off the corners and in combination with an applied field it results in a field-dependent lowering of the potential barrier.[72]

Eliminating these injection barriers is crucial for the elucidation of the working of the device and for elucidation of a material's charge transport parameters. Too large injection barriers result in a heavily injection limited current. This is not the actual current through the material ,and analysing it does not give correct values of, for example, the mobility. Moreover, any field and temperature dependence of the current is controlled by the injection process rather than the intrinsic material properties.

One way to eliminate this injection barrier is electrostatically decoupling the organic semiconductor from the electrode, which can be achieved by inserting a thin interlayer (~ 4 nm) between the organic emitter and the metal.[70,73] In order for holes to efficiently tunnel through the interlayer, the IE of the interlayer needs to be below that of the semiconductor. For electron injection the EA needs to be lower than that of the organic material. These design rules have shown to lead to truly ohmic contacts to organic semiconductors.[74] It should be noted that not every material/interlayer combination works as some interlayers can cause non-closed layers

and aggregation close to crystal boundaries, especially when used in combination with more crystalline semiconductors.[75]

1.4.3 Trap-free single carrier diodes

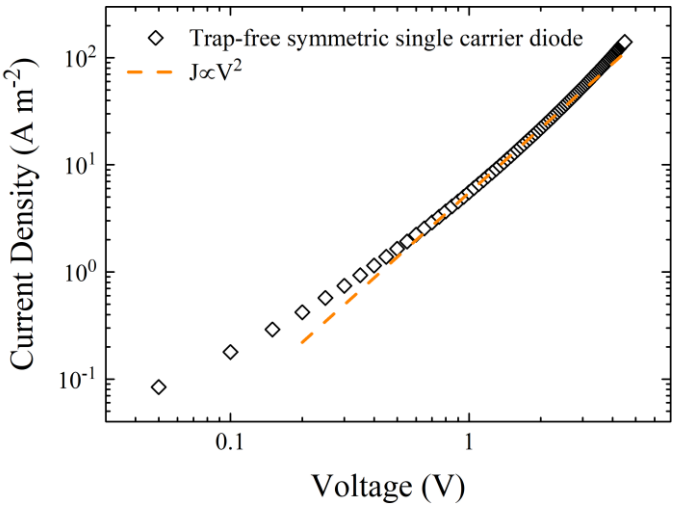

Figure 1.6: Simulated *J-V* of a trap-free symmetric single carrier diode (see **1.6.6**). The orange dashed line corresponds to a quadratic scaling with voltage.

The simplest case is a symmetric single carrier device, let's consider a HO diode, for which a typical *J-V* curve is given in figure 1.6. The absence of a build-in voltage means holes get injected immediately after applying a voltage, however at low applied voltages the diffusion of carriers dominates. Carriers diffuse from the contacts into the organic layer, this diffusion is controlled by the charge carrier gradient across the organic layer and the resulting diffusion current depends linearly on the voltage and inversely on third power of the thickness.[72,76]

At higher applied voltage the internal field promotes the injection of holes into the device and the current becomes drift-dominated, since the injected charges outnumber the charges from diffusion. In case of a single carrier device the charges are uncompensated by their opposite carrier species. The injected charges build-up in the organic material, and since they are uncompensated they create an electric field in the semiconductor.[47] This build-up of space charge throughout the device saturates when the space charge limited current (SCLC) is reached, which is the maximum current a HO or EO can sustain. Typical for the SCLC regime is the quadratic dependence on voltage in agreement with the classical Mott-Gurney equation:[77,78]

$$J_{SCLC} = \frac{9}{8}\varepsilon_0\varepsilon_r\mu\frac{V^2}{L^3}. \tag{1.10}$$

Here (L) is the device thickness. The thickness dependence of $J \propto L^{-3}$ is important to verify the occurrence of a SCLC current as is the quadratic scaling with the voltage. It is the thickness criterion that is used to distinguish a SCLC from an injection limited current, since the latter scales only inversely with thickness.[79] The Mott-Gurney equation is often used to extract the mobility of organic semiconductors,[78] however it should be used with care. It does not factor

in the density and field dependence of the mobility, and can thus overestimate the mobility if carelessly used in regimes where it is not applicable, for example at too high voltages where the field dependence has a big impact on the current.

For an asymmetric HO, one non-ohmic contact drastically reduces the carrier density at that contact. Equilibration of the chemical potential throughout the whole device results in a build-in voltage. The build-in voltage ensures injection is not favoured at $V<V_{bi}$, such that diffusion dominates in that regime. An analytical expression for the diffusion current of an asymmetric diode exists, showing that the diffusion current exhibits an exponential dependence on V below V_{bi} and a linear dependence above V_{bi}.[71,76] One further thing to note here is that the level where most carriers contribute to the transport ($E_a = \frac{\sigma^2}{2k_BT}$) is temperature dependent, so that any injection barrier resulting from a non-ohmic contact will also scale with temperature.

1.4.4 Trap limited transport in single carrier diodes

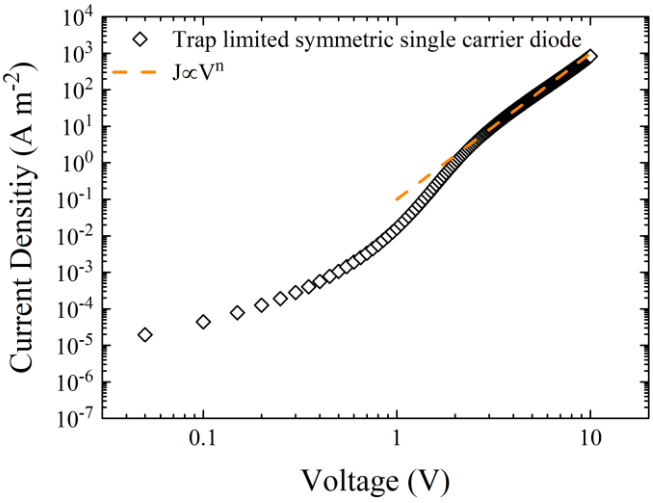

Figure 1.7: Simulated *J-V* of a trap limited symmetric single carrier diode (see **1.6.6**). The orange dashed line corresponds to a V^n scaling, with n>2.

One typical reason a single carrier device will not show SCL transport is the presence of additional lower lying states in the bandgap of the organic material. These are referred to as (charge) traps, and it is energetically favourable for charge carriers to go to these sites. Whereas the density of transport sites is generally around 10^{26} m^{-3} the trap density is lower, on the order of $10^{22\text{-}23}$ m^{-3},[47] but nevertheless they can have a big impact on the device characteristics. Once carriers are trapped, generally no hopping between traps can take place as they are spatially too far apart. Furthermore, since normal transport sites are too far up in energy, trapped carriers don't contribute to the device current. Figure 1.7 shows the typical behaviour of a symmetric trap-limited diode. We see the trap filling at lower voltages that changes into a trap-filled regime at higher voltages.

Figure 1.7 shows the theoretical curve during the forward scan only, but during a whole scan cycle of a trap-limited single carrier device, the current in a forward scan (e.g., 0 to 5 V)

generally does not follow the same path when scanning back immediately after (5 to 0 V in this case). When scanning a trap-limited sample for the first time, in the forward scan carriers fill up the charge traps, but they are not released in the back scan and consequently the overall current is lower there, i.e. hysteresis appears in the *J-V*.[80]. If one would scan such a sample a second time, the forward scan will follow the back scan of the previous scan cycle as the carriers remain trapped.

In the case that the traps are exponentially distributed in energy, Mark and Helfrich proposed the following equation for the current:[81]

$$J_{MH} = N_c q \mu_{n/p} \left(\frac{\varepsilon_0 \varepsilon_r}{q N_t}\right)^r \left[\left(\frac{2r+1}{r+1}\right)^{r+1} \left(\frac{r}{(r+1)}\right)^r\right] \frac{V^{r+1}}{L^{2r+1}}. \quad (1.11)$$

With N_c the density of states in the conduction band and r a constant that depends on the trap distribution. The value of r can be determined from the slope of the *J-V* curve on a double-logarithmic plot. From equation (1.11) we see that the fingerprints of trap-limited currents are a stronger field dependence in the *J-V* characteristics compared to the SCLC case (see fig. 1.5) and furthermore, the thickness dependence is also stronger, providing a way to distinguish trap-limited currents from SCLC or injection-limited currents.

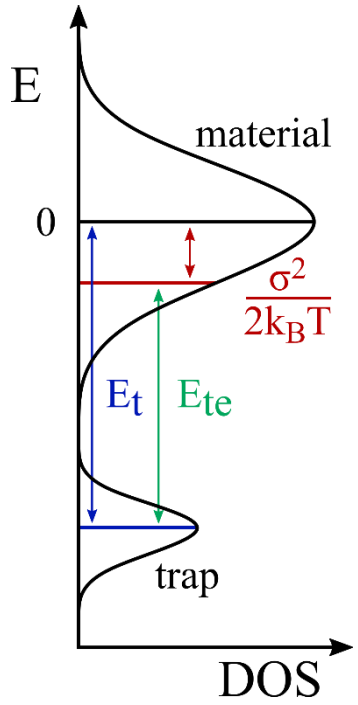

Figure 1.8: Gaussian trap DOS below the material DOS (LUMO) including the relevant energy levels.

The analytical expression above already explains a lot of the trap-limited physics, but two modifications were later made to Mark and Helfrich's expression. The first relates to the fact that Mark and Helfrich considered trapping below a single conduction band edge which remained constant with temperature. However, as we've seen in section 1.3.2, the DOS follows a Gaussian profile and the energy level where most carriers contribute to the transport is $E_a = \frac{\sigma^2}{2k_B T}$ below the middle of the DOS (E_0). The trapped carriers therefore need to make the jump

to E_a only, in other words E_a can be seen as an effective conduction band edge here.[82] The relevant energy levels are depicted in figure 1.8, showing that an effective trap depth (E_{te}) can be defined as:[83]

$$E_{te} = E_t - E_a. \tag{1.12}$$

Where E_t is the original trap depth w.r.t. E_0. Not only will the effective trap depth be lower than the original trap depth, but through E_a it will also depend on disorder and temperature. The most notable effect of a temperature dependent trap depth is that with decreasing temperature the effective trap depth will become smaller, as was experimentally verified.[82]

The second modification is that the trap level itself also has a Gaussian profile. Even though for analytical solutions the exponential distribution can be used to approximate a Gaussian profile,[84,85] nevertheless, the disorder creates different microenvironments for the traps, making the surrounding of a trap not uniquely defined. In this way the energy level of a trap is smeared out, making a Gaussian distribution most appropriate and intuitive.[83–86]. The Gaussian trap is also the one employed throughout this thesis, even when not explicitly stated.

The precise origin of charge traps proved difficult to ascertain, although screening many materials hinted that there exists two universal trap levels, sitting at -3.6 eV below the vacuum level for electrons and -6 eV for holes.[87] Through analyzing single carrier diodes, small molecules and conjugated polymers with an EA below 3.6 eV and an IE above 6 eV were indeed found to be trap free, and theoretical calculations showed that oxygen/water clusters provided an explanation for the common origin of these traps.[87,88] Most fluorescent polymers like MEH-PPV and SY-PPV contain this universal trap, but emitters that have energy levels within this energy window were found to be (almost) trap free.[89] Other origins of charge trapping that are sometimes pointed at include kinks and defects in the polymer chain, left-over impurities from the chemical synthesis and environmental contaminations.[90–92]

1.5 Light emission in organic semiconductors

Let's shift gears for a bit and concern ourselves with how organic semiconductors can be used as light-emitting materials. Excitons play a central role in the light emission of OLEDs, which is why this paragraph covers their most important concepts. We'll start from their formation, and slowly work our way towards interacting excitons.

1.5.1 Formation of excitons

The low dielectric constant of organic semiconductors means that electrons and holes can effectively form a bound state and the quasiparticle associated with a bound electron-hole pair is called an *exciton*.[28] When an exciton decays to the ground state, i.e. the electron and hole recombine, photons are generated. Excitons are efficiently generated in OLEDs after double carrier injection, but this is not the only way to create excitons in organic materials. Excitons can also be formed optically, by pumping the organic material with photons from a lamp or

laser. The excitons encountered in organic semiconductors are almost exclusively of the Frenkel type.[91,93] That means they are located on the same molecule, have a significant binding energy (0.4-1 eV) and a small spatial radius.[94]

Electrons and holes are fermions and thus both carry spin (s) $|s| = \frac{1}{2}$ with spin quantum number m_s, either oriented upwards (↑, s = ½, m_s = ½) or downwards (↓, s = -½, m_s = -½). To describe a molecular state the total wave function (Ψ) is a combination of a spatial wavefunction, which we encountered in section 1.2.1, and the spin wavefunction (ψ_s): $\Psi = \psi_{el}(\vec{r}, \vec{R}) * \psi_s$.[13,93] Following the Aufbau principle (lower molecular orbitals get filled first) and Pauli's exclusion principle, the orbitals up and until the HOMO are filled with anti-parallel spins. The frontier orbitals are the ones that play a role in carrier conduction and thus exciton formation, as the states that lie below the frontier orbitals are stronger bound and with total spin (the sum of all spins, S) equal to 0, rendering them practically inert. Like $\psi(\vec{r}, \vec{R})$ follows the Schrödinger equation, ψ_s in the one-electron case needs to obey the length of the spin angular momentum operator ($\hat{S}$) and its z-component: $\hat{S}^2$ and $\hat{S}_z$.[95] The eigenvalues are s(s+1)$\hbar$ and $m_s\hbar$ respectively. Analogously, a two-electron system needs to obey $\hat{S}^2 = (\widehat{S_1^2} + \widehat{S_2^2})$. The multiplicity ($M$) of a given total spin state is $M = 2S+1$ according to the different values the total spin quantum number M_s can take. A two-electron system obeying these operators will have 4 allowed wavefunctions (for the excitons), which we can denote in Dirac notation as $|S, M_s\rangle$. Depending on the pairing of ↑ and ↓ we obtain:[13,15]

$$|1,1\rangle = \uparrow\uparrow, \tag{1.13a}$$

$$|1,0\rangle = \frac{1}{\sqrt{2}}(\uparrow\downarrow + \downarrow\uparrow), \tag{1.13b}$$

$$|1,-1\rangle = \downarrow\downarrow, \tag{1.13c}$$

$$|0,0\rangle = \frac{1}{\sqrt{2}}(\uparrow\downarrow - \downarrow\uparrow). \tag{1.13d}$$

Consider an occupied HOMO that is filled with two holes with their spins configured in anti-parallel fashion. In that state $S = 0$, making $M_s = 0$, which is a *singlet* state. Since it is the lowest energy configuration, more specifically it is the singlet ground state (S_0). An exciton is in this picture one hole in the HOMO bound to one electron in the LUMO. Their spins can be again anti-parallel, making the spin of the exciton also $S = 0$ ($m_s = 0$), but since the electron is a molecular orbital higher in energy, this is the first singlet excited state (S_1), as in eq. (1.13d). The spin in both HOMO and LUMO can also be oriented parallel to each other, in which case $S = 1$ ($m_s = -1, 0, 1$), making it a *triplet* first excited state (T_1), as given in eq. (1.13a-c). Higher excited states such as S_2 or T_2 are also possible, it requires a hole bound to an electron in the LUMO + 1 energy level.

The four wavefunctions of the exciton associated with the two-electron system can thus be divided into one of singlet character and three with a triplet character. Via Pauli's principle, the total wavefunction must be anti-symmetric such that if the spin wavefunction is anti-symmetric, as for singlets, the spatial part is symmetric (and vice versa for triplets.) This property is ensured

by the antisymmetizer operator.[95] The anti-symmetry in the spatial wavefunction for triplets means physically that one electron is located in another orbital. The separation of the electrons reduces their wavefunction overlap and electron-electron repulsion as compared to singlets. Another way to look at this is to invoke the concept of exchange interaction again (paragraph 1.2.1), which increases the energy level of singlets, but decreases it for triplets. The result is that the triplet energy level lies lower than the singlet one, and that the gap between singlet and triplet level is determined by the exchange energy.[13]

1.5.2 Transitions involving singlet and triplet states

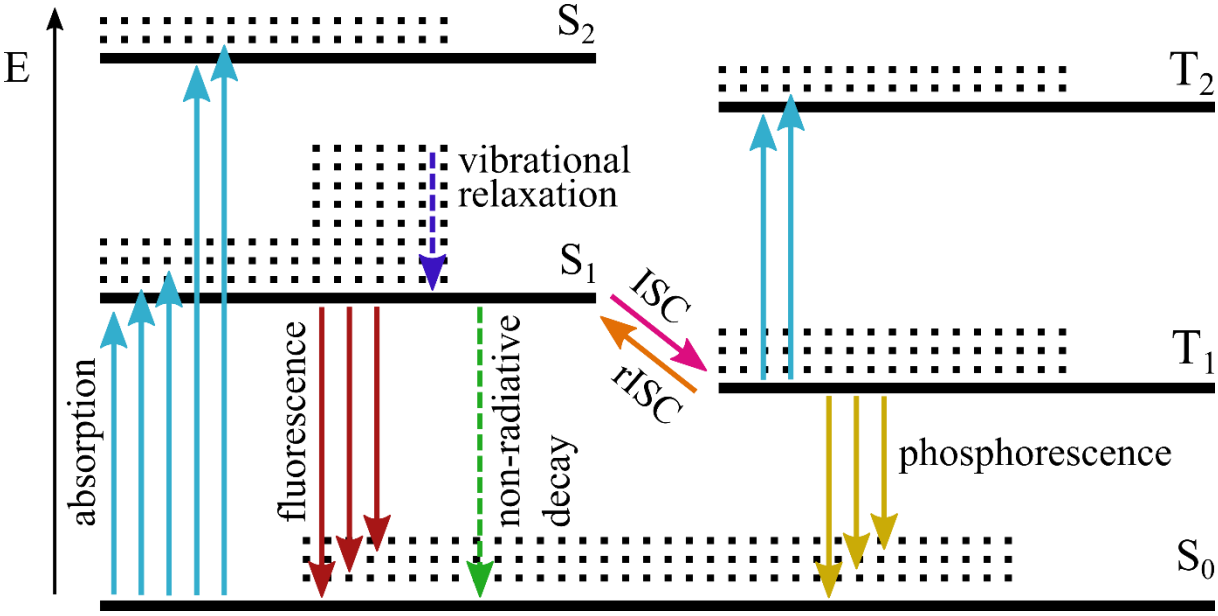

Figure 1.9: Jablonski diagram depicting electronic/vibrational levels as solid/dotted horizontal black lines. The transitions between electronic states are denoted as vertical lines and coloured according to their process. The dashed vertical transitions correspond to non-radiative transitions. Modified from reference.[96]

Optical transitions are conveniently depicted in a Jablonski diagram (figure 1.9). It is good to keep in mind that all processes shown in figure 1.9 have rate constants (k) associated with them, the radiative rate for fluorescence, k_f, for example, as this will be relevant when constructing a kinetic model for the exciton populations later. Before discussing the transitions depicted in figure 1.9, I would first like to mention the general expression for the rate of an optical transition, which is given by Fermi's golden rule:[13]

$$k = \frac{2\pi}{\hbar}\left|\langle \Psi_f|\widehat{H'}|\Psi_i\rangle\right|^2 \rho. \qquad (1.14)$$

Where ρ is the density of the final state, (k) is the rate of the transition from the initial state (i) to the final state (f) by the coupling element $\langle \Psi_f|\widehat{H'}|\Psi_i\rangle$. H' is the perturbing Hamiltonian, which is for optical transitions the transition dipole operator $e\vec{r}$.

Recall the separation of the spatial and spin-part of the total wavefunction. Until now we did not consider nuclear motion, but molecules and by extension nuclei are not stationary entities. Nuclei can vibrate, and this behaviour is best described considering coupled harmonic oscillators, which naturally have a set of quantized energy levels associated with them. These vibrational levels lie within the electronic energy levels and electrons can use these vibrational levels to relax, in other words, they dissipate energy via heat, which is a non-radiative process. The oscillating behaviour means every horizontal line in the Jablonski diagram (figure 1.9) can be seen as an asymmetric parabola, with the vibrational energy levels filling it up. Since nuclear motion is negligible compared to electronic motion (Born-Oppenheimer approximation) the transitions between electronic energy levels are always depicted as vertical lines (the Franck-Condon principle) as to maximize their vibrational overlap and leave the nuclear coordinate unchanged.[15] The Born-Oppenheimer approximation allows us to decouple the nuclear from the electronic motion and write the total wavefunction as a combination of an electronic, a spin, and a vibrational part ($\psi_{vib}(\vec{R})$).

$$\Psi = \psi_{el}(\vec{r}, \vec{R}) * \psi_s * \psi_{vib}(\vec{R}). \tag{1.15}$$

Note that we omit the rotational component since its energies are almost always too small to be of relevance. With the separation of wavefunctions we write Fermi's golden rule as:[13]

$$k = \frac{2\pi}{\hbar} \left|\langle \psi_{el,f} | e\vec{\boldsymbol{r}} | \psi_{el,i} \rangle\right|^2 \left|\langle \psi_{s,f} | \psi_{s,i} \rangle\right|^2 \left|\langle \psi_{vib,f} | \psi_{vib,i} \rangle\right|^2 \rho. \tag{1.16}$$

The dipole operator only acts on the electronic wavefunction, and the rate of the electronic transition scales with the overlap between the two wavefunctions of the initial and final state. The spin part in eq. (1.16) means that if the initial and final state have equal spin character, the transition is spin-allowed, otherwise this factor becomes zero, and the transition becomes forbidden.

As we've seen, the ground state in organic semiconductors carries a singlet character, such that via Fermi's golden rule (eq. (1.16)) an exciton in S_1 is quantum mechanically allowed to fall back to S_0. While doing so it emits its energy as a photon, and this process is called fluorescence, which usually occurs on the order of a few ns in light-emitting polymers.[97] The converse process is called singlet absorption. Absorptions to higher vibrational levels can occur, but this is followed by (non-radiative) vibrational relaxation to the lowest excited state, as via Kasha's rule we know that photon emission occurs most strongly from the lowest excited state. Kasha's rule holds when vibrational relaxation is much faster than emission or non-radiative decay, which is usually the case. We can reason that the absorption is therefore redshifted as compared to the emission, which is known as a Stokes shift. A competing process for fluorescence is non-radiative decay from S_1 to S_0, which scales with vibrational wavefunction overlap of the two energy levels. According to the well-known 'energy gap law' the non-radiative decay rate scales as $\propto exp(-\Delta E_{S0,S1})$, with $\Delta E_{S0,S1}$ here being the energy difference between S_1 and S_0.[98] This means non-radiative decay is in red emitters particularly challenging to overcome.

The spin-flip that needs to be made when an exciton in T_1 wants to fall back to the ground state is quantum mechanically forbidden, however on the order of μs-ms triplets can radiate via

phosphorescence, albeit generally with low probability. This can occur because only the total angular momentum, being the sum of orbital and spin angular momentum, needs to be conserved during the transition. The two angular momenta can couple, so called spin-orbit coupling, such that the triplet gains some singlet character, making the spin flip an allowed process.[93] Since the strength of spin-orbit coupling scales with the fourth power of the atomic number, incorporating a heavy metal in your emissive material increases spin-orbit coupling and phosphorescence can occur on faster timescales because of this.[4,99,100] The 2nd generation of OLEDs is based on this principle, however, as already mentioned, this does mean that phosphorescent OLEDs require an expensive, environmentally unfriendly heavy-metal complex in the active layer.

In absence of any coupling between S_1 and T_1, optically only singlets are generated. However, photophysical transitions between singlet and triplet excited states can occur, and since this involves a spin flip the transition is again mediated by spin-orbit coupling. The transition from S_1 to T_1 is called intersystem crossing (*ISC*) and from T_1 to S_1 is reverse intersystem crossing (*rISC*). This is what TADF materials exploit without using heavy-metals, as we will see in the next paragraph.

1.5.3 Photophysics of TADF materials

In 2012 the Adachi group found a way to harvest triplets without the use of an additional heavy metal dopant, but instead created organic emitters that used thermal energy to convert the triplet back to the singlet state. This mechanism is known as thermally activated delayed fluorescence (TADF).[7]

Until now, we did not assume anything about the distribution of the exciton over a molecule. For conjugated polymers, for example, excitons are localized to one part of the molecule, but this does not necessarily have to be the case. As a first design rule, donor-acceptor (D-A) type TADF materials have separate moieties for hole and electron transport, often oriented nearly orthogonal with respect to each other. As a consequence, the exciton has a significant dipole associated with it and is strictly speaking not of the Frenkel type anymore, but of the charge transfer (CT) type. One would denote this as ^{1}CT for singlet and ^{3}CT for triplet excitons. This has consequences for the energetics of these excitons, most notably CT excitons are very sensitive to the polarity of the environment. This leads to the observance of solvatochromism in D-A type TADF molecules for example.[101] Since the HOMO-LUMO overlap is significantly reduced by spatially separating the D and A moieties, the exchange integral (section 1.2.1) is reduced.[102] A reduction in exchange energy means the energy splitting between singlet and triplet state (ΔE_{ST}) is reduced, often to the order of only tens of meV.[103] The small singlet-triplet gap promotes rISC, and this is exactly what presents a way to harvest triplet states. In addition, the D-A design introduces more structural relaxation of the first excited state, leading to broad emission spectra.[104] From Fermi's golden rule we can reason that another drawback of small wavefunction overlap is that the radiative rate is reduced as well, which is reflected by intrinsic singlet lifetime values on the order of 100 ns, much longer than the few ns found in fluorescent polymers.[105,106]

Thus, crucial for the performance of a TADF material is rISC. A simple dependence for k_{rISC} is given by:[103]

$$k_{rISC} \propto exp\left(\frac{-\Delta E_{ST}}{k_B T}\right). \quad (1.17)$$

From equation (1.17) we see that rISC is a temperature dependent process. One way to thus experimentally confirm TADF behaviour is to check if it disappears when moving to lower temperatures, for example in an ultrafast optical experiment.[101] Another often employed method to check for TADF behaviour is to measure the PLQY in an O_2-environemnt versus an N_2-environment. Since oxygen quenches the triplet state, an increase in PLQY under nitrogen hints at TADF behaviour, however one must be careful to draw quantitative conclusions from these experiments, since it depends heavily on the permeability of oxygen into the thin film.[107] Whereas rISC needs thermal energy, ISC is a downhill process and one would thus not necessarily expect a strong temperature dependence. Indeed, ISC seems to be only weakly temperature dependent in some cases.[108,109]

The rISC process is accompanied by a spin flip and thus must be mediated by spin-orbit coupling to be quantum mechanically allowed, however there are no heavy-atoms to enhance the coupling, as in phosphorescent OLEDs. Till now we assumed that both singlet and triplet are of the CT character, but this would make the spin flip forbidden, as was confirmed by theoretical calculations,[110] since the electrons have the same spatial occupation. A change in spin can in this case not be compensated by a change in orbital angular momentum to conserve the total angular momentum. Thus the importance of additional locally excited (*LE*) states for rISC was recognized.[108,111–114] The ^{3}CT and ^{3}LE states switch character, or 'mix', until they reach equilibrium. The mixing was suggested to be driven by the vibronic coupling between the two triplet states and happens on timescales faster than the occurrence of rISC.[115–117] From the ^{3}LE state the spin flip can be readily made to the ^{1}CT and since they are of different orbital type the change in spin becomes much easier (this is known as El-Sayed's rule). The full spin flip is thus mediated by spin-orbit coupling as well as vibronic coupling. The approximation that we can decouple the electronic, spin and vibronic wavefunction as introduced earlier (eq. (1.16)) is therefore not fully correct for TADF emitters.

Reliable extraction of the photophysical parameters is key for the development of high performance TADF materials. Standard practice is to obtain the rate constants for (r)ISC and the lifetimes by biexponential fitting or kinetic modelling of time-dependent photoluminescent decays.[118] In an optical transient photoluminescence (TrPL) experiment, only singlets are generated, but there is coupling to the triplet state via (r)ISC. In a TrPL curve this leads to the normal prompt fluorescence (PF) and singlets coming from the triplet state contribute to the light as delayed fluorescence (DF). In Appendix C, figure C.1 there is an example of such a TrPL decay.

Before TADF emitters can come to the stage of commercialization there are still several issues that need to be resolved and a better understanding of the TADF mechanism needs to be gained.[119] One issue is finding an efficient and stable blue emitter.[120] Another issue is that since the exciton is of the CT type, the different microenvironments with slightly different

polarizations result in a broad emission spectrum. In other words, the colour purity is not optimal. One final issue I would like to mention is the operational stability in general, which is still far from sufficient for commercial applications.

Recently some of these issues have been addressed. The development of hyperfluorescent devices is an example, where a fluorescent dopant is mixed with a TADF emitter. Hyperfluorescence is trying to get the best of both worlds in the sense that triplets can be converted to emissive singlets on the TADF molecule for 100% internal quantum efficiency and thereafter be transferred to the fluorescent molecule to radiate with higher colour purity.[121] Another, more recent, approach is multi-resonance TADF, where the classic D-A structure is absent, but the separation of HOMO and LUMO is achieved on the same molecule.[104] The more rigid structure of multi-resonance emitters allows for greater coupling to the ground state and less structural relaxation, leading to smaller full-width half-maxima (FWHM) for the emission spectrum as well.[104] Also for these more novel approaches, it has to be mentioned that lifetime remains one of the biggest issues.

1.5.4 Exciton transfer mechanisms

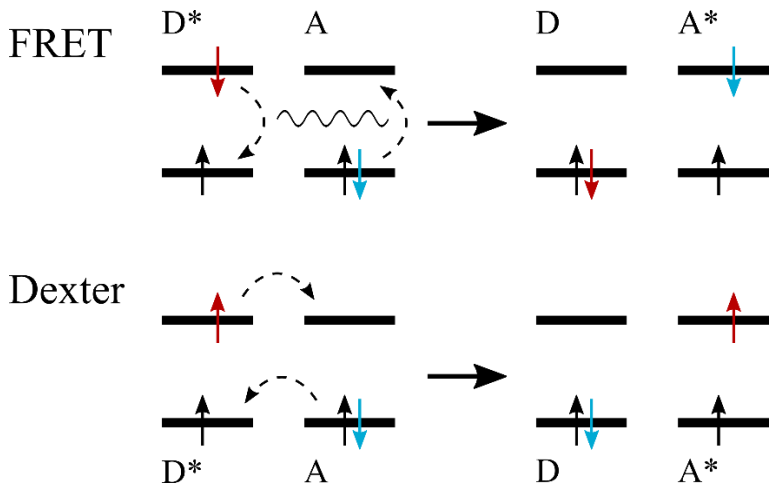

Figure 1.10: Illustration of the FRET and Dexter process. 'D' and 'A' refers to donor and acceptor, a '*' indicates an excited state.

Despite being fairly localized, excitons can move by diffusion or they can transfer between two molecules. Diffusion is a temperature dependent process, with higher temperatures resulting in faster diffusion. Another consideration is that the material is disordered. Increasing disorder slows diffusion down, as was measured for various polymers, for example.[97]

Singlets predominantly move around by transfer of energy from an initial to a final molecule, or from the donor to an acceptor, by Förster resonance energy transfer (FRET),[122,123] either via a single step transfer or via a multistep process.[93] The FRET process is efficient when the emission of the donor overlaps with the absorption of the acceptor and since the Förster mechanism is based on dipole-dipole interactions it depends on the spacing between the donor and acceptor (r) proportional to r^{-6}.[122] Triplets on the other hand mostly transfer and diffuse based on the Dexter mechanism,[124] which involves the physical transfer of an electron and

therefore requires overlap between the wavefunctions of two molecules. Both FRET and Dexter transfer are illustrated in figure 1.10. The total spin is conserved during the Dexter process and the dependence of Dexter transfer on the spacing between donor and acceptor is as $\propto \exp(-r)$. It follows form the distance dependencies that Dexter transfer is a short-range process (~1-2 nm), whereas FRET can occur over several nanometres (~5-8 nm). Also relevant here is that the lifetime of singlets is in most cases far shorter than the lifetime of triplets, such that the actual diffusion length (L_D) of the two can depend strongly on the material that is used.

More complicated models for Dexter transfer exist, viewing the Dexter process as double electron transfer instead and applying the established models for electron transfer, such as Holstein's, Marcus and Miller-Abrahams theories.[94] Another possibility is employing Monte Carlo (MC) simulations to study the complex interplay of all processes triplets can undergo during their lifetime. This can give more fundamental insight in for example the temperature dependence of Dexter transfer.[125]

1.5.5 Interaction processes involving excitons

The ability for an exciton to move around correlates with the probability that it will find another particle with which it can undergo an interaction, meaning diffusion underlies most of the interactions excitons can undergo. Here I discuss the ones most relevant for OLEDs: triplet-triplet annihilation (*TTA*)[126–134], triplet-polaron annihilation (*TPA*)[135–140] ,and singlet-triplet annihilation (*STA*)[135,141,142].

Triplet-triplet annihilation

Two interacting triplets means we are considering a four-electron system and much like the two-electron system we encountered earlier, only certain allowed wavefunctions for a four-electron system obey the spin operators (section 1.5.1). When two triplets interact they will form an intermediate state, denoted ^{x}(TT) where *x* here denotes the character (singlet, triplet or quintet).[143] One triplet will give its energy to the other, promoting one to a higher lighting excited state (denoted by the subscript *n*) and demoting the other to the ground state.

The first possibility when two triplets (S=1) interact is that they create a quintet state (*Q*, where S=2):

$$T_1 + T_1 \rightarrow {}^{5}(TT) \rightarrow Q_1 + S_0. \tag{1.18}$$

However, the quintet state is generally too high in energy to be accessible at room temperature ,[144] thus the intermediate will break apart into two triplets again, effectively making this a scattering event. The remaining process of TTA can be expressed as:[141,143]

$$T_1 + T_1 \begin{cases} \xrightarrow{0.25*k_{TTA}} {}^{1}(TT) \rightarrow S_0 + S_n \rightarrow S_0 + S_1, \\ \xrightarrow{0.75*k_{TTA}} {}^{3}(TT) \rightarrow S_0 + T_n \rightarrow S_0 + T_1. \end{cases} \tag{1.19}$$

One triplet transfers its energy to the other, thereby relaxing to the ground state. The other exciton is promoted to a higher lying excited state, after which it will rapidly thermalize to the first excited state. We can see from (1.19) that next to being a loss process for triplets, TTA generates singlets, which is not spin forbidden since only the total spin needs to be conserved.

k_{TTA} is the TTA rate constant, a measure of the interaction strength for TTA. When not considering any explicit dependence, k_{TTA} implicitly depends on diffusion, temperature, triplet density, time etc..[132,145] This means that in ultrafast optics experiment for example, the use of a constant k_{TTA} is not always accurate,[146] but can be employed as a first approximation. This holds for the rate constants of STA and TPA as well. Since $[\mathrm{T}] \propto \mathrm{J}$ it follows that $[\mathrm{T}] * [\mathrm{T}] \propto \mathrm{J}^2$ or alternatively one can exchange the current density here with the optical excitation density. As a consequence, TTA becomes relevant at high current densities or higher laser powers. The singlet generation through TTA means TTA can cause delayed fluorescence, but the quadratic dependence on the incident laser power means, in an optical experiment, it can be distinguished from fluorescence, TADF or phosphorescence, since these all show a linear dependence on the excitation dose.[103]

Triplet-polaron annihilation

Alternatively, a triplet can give its energy to a polaron, quenching the triplet, which is commonly referred to as TPA. This processes is denoted by:[143]

$$\mathrm{T}_1 + \mathrm{p/n} \xrightarrow{\mathrm{k_{TPA}}} \mathrm{S}_0 + \mathrm{p/n}^* \rightarrow \mathrm{S}_0 + \mathrm{p/n}. \tag{1.20}$$

Where k_{TPA} is the TPA annihilation constant. Since $[\mathrm{T}] \propto \mathrm{J}$ and $\mathrm{n/p} \propto \mathrm{J}^{1/2}$ it follows that $[\mathrm{T}] * \mathrm{n/p} \sim \mathrm{J}^{3/2}$, a slightly reduced scaling with J as compared to TTA.

Singlet-triplet annihilation

The last process I discuss here is the interaction between a singlet and a triplet which is written as:[143]

$$\mathrm{S}_1 + \mathrm{T}_1 \xrightarrow{\mathrm{k_{STA}}} \mathrm{S}_0 + \mathrm{T}_\mathrm{n} \rightarrow \mathrm{S}_0 + \mathrm{T}_1. \tag{1.21}$$

This is a two-exciton interaction like TTA, but whereas TTA negatively impacts the triplet population, STA has a negative impact on the singlet population. Again, the scaling with current density is quadratic.

We see that all of these processes result in the loss of excitons, making them unfavourable in OLEDs. Therefore, several strategies have been put forth to supress annihilation processes. Three common ones are controlling the distribution of excitons inside the active layer, to dope the emitter in a conductive host and to reduce the exciton lifetime.[147–152] Not piling all excitons onto one part of the active layer naturally helps to reduce their interaction. Reducing the exciton lifetime, for example by increasing k_{rISC} in TADF materials, also helps to alleviate annihilation.

With electrical as well as optical processes understood we can move towards the complete OLED device, where the two come together.

1.6 Double carrier diodes

An OLED is inherently a double carrier diode, meaning both carrier types contribute to the total device current. We have seen the injection, transport and recombination mechanisms in previous sections, now, it is time to combine the knowledge of previous sections in order to understand the full OLED device operation. In this paragraph we will see the device design and the device characteristics of OLEDs in more detail. Electrical and optical characteristics will be treated as well as the efficiency of an OLED. At the end the numerical model used in this thesis is introduced.

1.6.1 OLED device design

The simplest OLED one can envision has an emitting layer sitting between two metals. Upon the application of a positive bias voltage, electrons and holes are injected in the organic emitter. The charges are transported towards each other under the influence of this applied electric field. Excitons will form when the carriers meet, and the excitons will eventually recombine, producing light that needs to escape the OLED.[153]

To inject both carrier types, in an OLED the anode WF needs to be matched with the HOMO of the semiconductor on one side of the device and the cathode WF with the LUMO on the other side. One of the electrodes has to be transparent in order to let light out of the OLED, usually this is the anode. One can achieve finer control of the OLED properties by adding additional layers. Hole- and electron-injection layers (HIL/EIL) are used for smooth injection, by minimizing the energy barrier from the WF of the metal to the HOMO/LUMO of the next semiconductor. Hole- and electron-transport layers (HTL/ETL) ensure proper transport to the emissive layer, and hole- and electron-blocking layers (HBL/EBL) ensure no carriers leave the emitter layer, such that the maximum amount of light can be emitted from the device.

1.6.2 Electrical characteristics of OLEDs

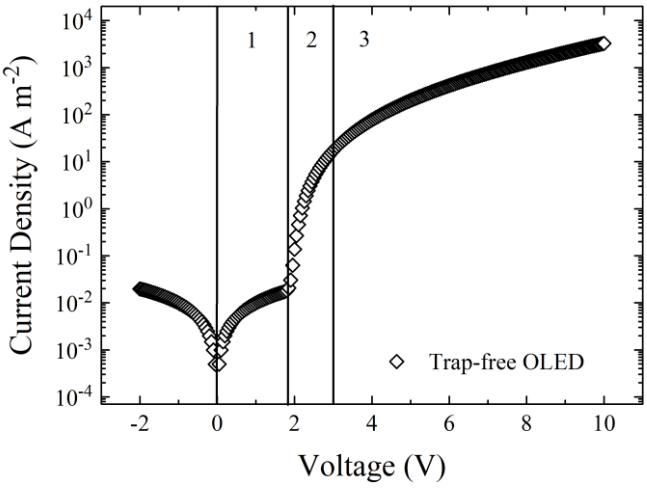

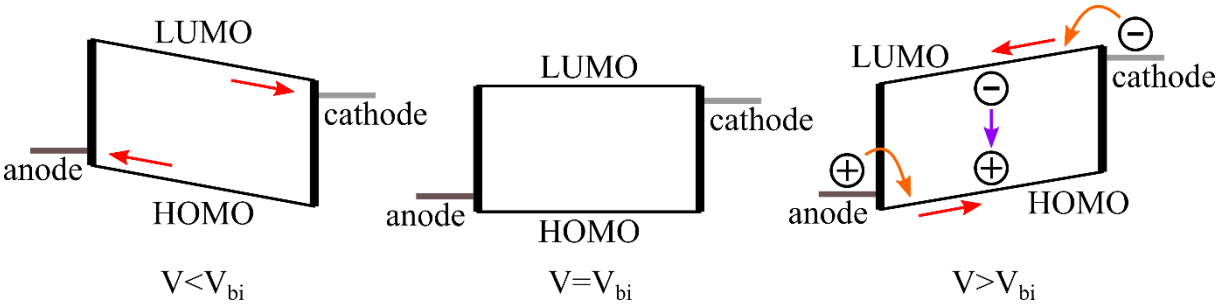

Figure 1.11: (a) Typical *J-V* of a trap-free OLED. (b) Three regimes of OLED operation with *V* respect to V_{bi}. The coloured arrows represent injection (orange), transport of carriers due the build-in electric field (red) and recombination (purple). The red arrows represent the direction of the drift current due to the electric field in the device, note that the diffusion current points in the opposite direction.

Figure 1.11(a) shows the typical *J-V* of a trap-free OLED device, from which three regimes can be distinguished. The *J-V* characteristics of an OLED can be explained using band diagrams, such as in figure 1.11(b), where we have three scenarios depending on the value of *V* with respect to V_{bi}.[47] Due to the alignment of the chemical potential throughout the device, there exists a build-in voltage across the OLED. We encountered this situation for asymmetric HO devices already (section 1.4.1), but for OLEDs the build-in voltage is larger due to the larger offset in WFs of the two electrodes. The electric field points towards the contacts for $V < V_{bi}$, and efficient injection will not take place. The direction of the diffusion points opposite to the internal electric field, and in this regime there is diffusion of carriers into the active layer, however the diffusion current is overshadowed by the leakage current that originates from local shorts.[54] This leads to regime 1 in figure 1.11(a), which is referred to as the leakage regime. The leakage current is temperature independent and obeys Ohm's law: a linear current-voltage relationship. Generally, we want the leakage current to be as low as possible, such that we see our actual device current clearly. The carrier density in the bulk of the organic semiconductor (as opposed to at the contacts) is low at these low electric fields, thus upon approaching V_{bi} the current can vary substantially with small differences in applied voltage. Around V_{bi} the diffusion current starts to dominate, which gives the exponential current-voltage dependence, as seen in regime 2 of figure 1.11(a). Exactly At $V = V_{bi}$ we have the flat-band condition, where there is no internal field over the device. Here the transition from the diffusion to the drift regime takes place. In figure 1.11(a) the line between regime 2 and 3 corresponds to V_{bi}. At $V > V_{bi}$ we are in the drift regime, regime 3 in fig. 1.8 (a). For a trap-free OLED the SCLC formula now includes the mobility of both carriers:[154]

$$J = \left(\frac{9\pi}{8}\right)^{1/2} \varepsilon_0 \varepsilon_r \left(\frac{2q\mu_p\mu_n(\mu_p+\mu_n)}{\varepsilon_0\varepsilon_r B}\right)^{1/2} \frac{V^2}{L^3}. \tag{1.22}$$

With *B* the bimolecular recombination constant (see section 1.6.3).

Different from single carrier diodes is that holes and electrons electrostatically compensate each other, meaning the charge carrier density in a double carrier device always exceeds the density found in a single carrier diode.[47] Another difference is that the 'sink' for electrons and holes

in an OLED is not the counter electrode anymore, as for single carrier devices, but their recombination, which is the topic we will explore next.

1.6.3 Recombination in OLEDs

Excitons falling back to the ground state, or equivalently, recombination of electrons and holes, is the process by which photons are generated in an OLED. This emissive or bimolecular recombination in an OLED is of the Langevin type (denoted by subscript *L*),[155–158] where both types of carriers diffuse towards each other. The expression for the Langevin recombination rate R_L [m^{-3}] is as follows:

$$R_L = \frac{q}{\varepsilon_0 \varepsilon_r}(\mu_n + \mu_p)(np - n_i^2). \tag{1.23}$$

Where n_i is the intrinsic carrier concentration, which is given by $n_i^2 = N_{CV} exp(-E_{gap}/k_B T)$ and with N_{CV} the density of states in the valence and conduction band. The dependence on the mobility in equation (1.23) means that finding a carrier of the opposite species gets easier with higher mobilities.

Besides Langevin recombination, OLEDs can also exhibit trap-assisted or Shockley-Read-Hall (SRH) recombination when a carrier falls in a trap and recombines with a free carrier of the other species.[159,160] Normally SRH recombination is non-radiative, making this is a loss-process in the device. Trapped carriers can in principle be promoted to the conduction/valence band again, i.e. de-trap, but this happens only on short timescales. On timescales relevant for a *J-V* measurement it is generally assumed that there is an equilibrium between trapping, de-trapping and recombination of trapped carriers with free carriers.[72] Under these equilibrium conditions the formula for R_{SRH} is given by:[159,160]

$$R_{SRH} = \frac{C_p C_n N_t}{C_n(n+n_1)+C_p(p+p_1)}(np - n_i^2). \tag{1.24}$$

With the capture coefficients given as $C_{n/p} = \frac{q}{\varepsilon_0 \varepsilon_r}\mu_{n/p}$ and $n_i^2 = n_1 p_1$, the product under equilibrium.

Formula (1.24) is for electron traps, for hole traps, N_t is simply replaced by P_t. The two recombination mechanisms can be distinguished for the light from a luminance-voltage (*L-V*) or for the current from a (*J-V*) plot through the ideality factor:

$$\eta = \left(\frac{k_B T}{q}\frac{\partial \ln(J/L)}{\partial V}\right)^{-1}. \tag{1.25}$$

The ideality factor amounts to 2 for SRH recombination and it is 1 for Langevin recombination.[161]

Note that in equation (1.23) there is an inverse dependence on the dielectric constant. As we've established in section 1.3, physically this means that in low dielectric constant materials electrons and holes effectively 'feel' each other's mutual coulomb field over a larger distance

as compared to higher dielectric constant materials. The Coulomb attraction occurs over such a spatial extent that in OLED materials there is a very high probability that electrons and holes will recombine instead of pass each other by. However, they don't interact with each other to such an extent that when they would meet, they immediately recombine (this is known as the plasma limit). Consequently there is not a plane of recombination, but rather a more spread out recombination zone.[162] Equation (1.23) shows that the Langevin recombination depends on the mobility, meaning that if there is a situation where the electron mobility exceeds the hole mobility, there would be a shift in the recombination zone towards the anode side of the OLED. Similarly, traps can cause an imbalance in the current and for e.g. electron traps there would be shift in the recombination zone towards the cathode side.

1.6.4 Optical outcoupling in OLEDs

Not all generated photons will escape from the OLED stack and emerge as useful light, the ones that do have 'outcoupled to air'. From classical ray optics the estimate is that about 20% of the photons couples to air, i.e. the outcouping efficiency (η_{out}) is around 20%.[163] A major contributor to the loss of about 80% of the light is the differences in refractive indices (n) between the organic material (n_{org} = 1.7), the glass of the substrate (n_{glass} = 1.5) and air (n_{air} = 1). When moving to a less dense optical medium, total internal reflections occur at the interface. The result is that light can get trapped in a waveguided mode at the organic-glass interface and a substrate mode at the glass-air interface.[164] Furthermore, photons can couple to electrons that reside in the metallic cathode via plasmonic coupling, via which photons get lost as surface plasmon polaritons (SPP),[165] i.e. travelling waves at the organic-metal interface. There is another deleterious effect for excitons associated with the metallic cathode and that is non-radiative exciton transfer to the metal, which only happens in regions close (~10 nm) to the metallic cathode.[166,167] Exciton quenching by a metal electrode is aggravated by imbalanced transport that pushes the recombination zone to the cathode side, especially if there is no spacer inserted between the cathode and the emitting material. Another factor relevant for outcoupling is the dipole orientation of the emitter, which can be assessed through variable-angle spectroscopic ellipsometry (VASE) or angular electroluminescence (EL) measurements. An arrangement such that the dipole moment lies in parallel to the substrate is wanted, since photons are mostly emitted perpendicular to the dipole orientation.[168] To take all effects into account simultaneously, outcoupling models have been developed, which give quantitative insight into the dissipation of the light to various channels.[169–171].

1.6.5 OLED efficiency

One of the most important metrics for OLED efficiency is the external quantum efficiency (*EQE*), which is the ratio of the amount of outcoupled photons divided by the number of injected (and diffused) charges. The *EQE* [%] is expressed as a combination of four factors, which we will discuss one by one:[13,172]

$$\mathrm{EQE} = \gamma * \eta_{S/T} * \Phi_{PL} * \eta_{out}. \tag{1.26}$$

Here γ is the charge balance factor that indicates how many excitons are formed from the injected charges, rather than being discharged at the electrodes or participate in SRH recombination. As discussed in **1.6.3**, Langevin recombination is very efficient such that in a trap free OLED with balanced mobilities $\gamma \approx 1$. In contrast, conjugated polymers containing electron traps reach $\gamma \approx 0.8$ at higher voltages.[172]

$\eta_{S/T}$ is the spin factor that represents the emissive exciton ratio. It is of paramount importance to make triplets emissive, since they comprise a far larger population in an OLED as compared to singlets. Following spin-statistics and assuming every spin state has equal probability to be created, for every singlet, three triplet states are created. Their population under electrical operation is thus divided into 25% singlets versus 75% triplets. The first generation of OLEDs uses only fluorescence and to first order $\eta_{S/T} = 0.25$ in fluorescent polymers. In phosphorescent and TADF OLEDs $\eta_{S/T} = 1$, where (ideally) 100% of the excitons are emissive. It was recognized however that this value of 0.25 does not always hold for PLEDs, since TTA has the ability to generate singlets.[126,173–175] Let's look in more detail at the efficiency of singlet generation via TTA.

We start with the TTA process as in equations (1.18), assuming the quintet route is inaccessible. It is convenient to assume that we start with 18 triplets, such that 10 triplets are recycled via the quintet route, 3 triplets remain via the triplet intermediate (and 3 get lost), and 1 singlet is gained via the singlet intermediate (and 1 triplet gets lost). The singlet yield is $\frac{1}{18}$ for the first cycle, but the 13 remaining triplets can again participate in TTA and from that second cycle again the singlet generation would be $\frac{1}{18}$. Thus we can write after an infinite amount of cycles:[126]

$$\sum_{n=0}^{\infty} \frac{1}{18} \cdot \left(\frac{13}{18}\right)^n = \frac{1}{18} \cdot \frac{1}{1 - \frac{13}{18}} = 0.2 \tag{1.27}$$

Where we use the properties of a converging geometric series with r = 13/18. Equation (1.27) means the efficiency of the TTA process is 20%, therefore the total electrical efficiency can at maximum be raised to:

$$\eta_{total} = 0.25 + 0.75 * 0.2 = 0.4. \tag{1.28}$$

TTA thus has the potential to elevate $\eta_{S/T}$ to 40%. In the special case that ^{3}(TT) cannot reach T_2, the triplet intermediate will dissociate again into $2*T_1$ leaving only the formation of singlet excitons as an allowed process. This is called triplet fusion, which is found in rubrene or certain anthracene derivatives,[176,177] and (following the same derivation) it has the potential to raise the maximum value of $\eta_{S/T}$ to 62.5%.

The ratio of the radiative decay rate to the total decay rate (radiative + non-radiative) defines the photoluminescence quantum yield (*PLQY*) value (Φ_{PL}) [%] as:[172]

$$PLQY = \frac{k_{rad}}{k_{rad} + \sum_i k_{nonrad,i}}. \quad (1.29)$$

The constants k_{rad} and k_{nonrad} are the radiative and nonradiative rate. The nonradiative rates are written as a sum since there are several contributions, a.o. vibrational relaxation, but also exciton quenching at trap sites.[97,178]

For completion I mention here that η_{out} is the outcoupling value, as introduced in section 1.6.4.

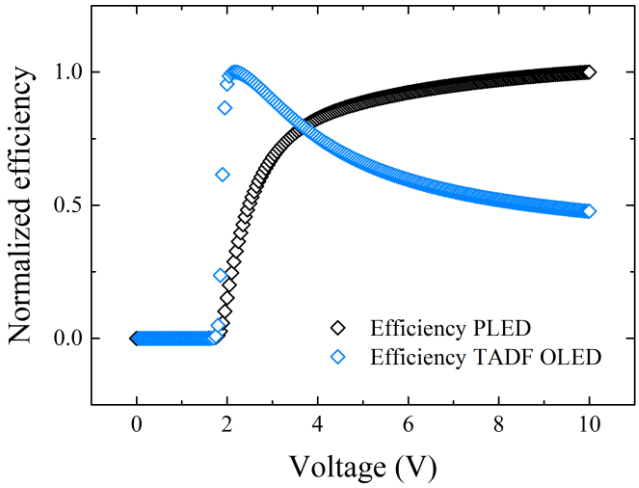

Figure 1.12: Simulated typical efficiency curves of a trap containing PLED and a trap-free TADF OLED.

Figure 1.12 shows a typical normalized efficiency curve versus voltage of an electron trap containing PLED and a trap free TADF OLED. Below V_{bi} the measurement equipment is generally not sensitive enough to detect the low amount of light coming out of the OLED, which at those low voltages results from diffusion of charges into the organic layer.[179] Furthermore, the leakage current, not the actual device current, dominates, leading to an observed efficiency that is practically zero. Around V_{bi} when the injection of charges starts to become relevant, and the light becomes experimentally detectable, the efficiency will shoot up, straight to one in a trap free case, as shown for the TADF OLED in figure 1.12. If the active material contains traps, these will be filled at low voltages and the SRH recombination will compete with Langevin recombination.[47,161] This leads to efficiency curves typical for PLEDs (figure 1.12), where the efficiency solely increases with voltage. At higher voltages a plateau is reached for the PLED efficiency in contrast to what is seen for TADF OLEDs. In TADF OLEDs the efficiency decreases with increasing voltage, which is commonly referred to as 'roll-off' and it is associated with annihilation processes like TTA, TPA and STA that remove otherwise radiative excitons.

1.6.6 Numerical drift-diffusion model part 1, electrical modelling

The analytical formulas for the trap-free or trap-containing single carrier current can provide useful insights, but inherently the current is a superposition of both drift and diffusion, which cannot be solved analytically. A numerical approach, namely the well-known drift-diffusion

modelling,[62,63,180] is used instead throughout this thesis. At first it may seem questionable not to consider the hopping nature of the electrons directly in order to describe their transport. However, we consider device sizes far exceeding the hopping distance and a large number of particles. The carriers are assumed to be non-interacting particles, and their densities are treated as a 'continuum', in this case drift-diffusion was found to be suitable for describing charge transport. Of course, other modelling approaches exist. These come in various levels of complexity, for example, we've seen analytical formulas already, which rely more on fitting parameters rather than underlying physical processes to describe macroscopic observables. Analytical theories often provide less detail, but also more complex methods than 1D drift diffusion are being used. Popular alternatives that provide more physical detail are the statistical Monte Carlo methods, like kinetic Monte Carlo (KMC), however these come at the cost of significantly more computation time. These MC methods often consider the various rates directly, for example MC can consider the probability of hopping via the Marcus rate equation, instead of relying on an analytic expression for the mobility as is done in the EGDM. For even more microscopic detail one can resort to atomistic simulations to generate a morphology of the system from first principles.[181] This way one does not need to consider the idealized picture of a lattice. However, such an approach needs to be combined with, say, Monte Carlo simulations, to link the underlying morphology to macroscopic parameters.[55,181] Drift-diffusion sits somewhere comfortably in the middle when it comes to the tradeoff between the underlying physics and the link between macroscopic observables. Nevertheless, 1D drift-diffusion has been verified using more extensive methods, like MC, which showed little variation between them.[79,182]

The drift-diffusion model makes a 1D grid on which the Poisson and current continuity equations are solved iteratively and in a position dependent fashion in order to obtain the charge carrier densities in the device.[180] The mobility then follows according to the EGDM framework, which is used to calculate the current. The Poisson equation:[154]

$$\frac{\varepsilon_0 \varepsilon_r}{q} \frac{dE(x)}{dx} = p(x) - n(x) + P_t(x) - N_t(x). \tag{1.30}$$

relates the electric field to the trapped and free (space) charge in the device while the continuity equation:[154]

$$\frac{1}{q}\frac{dJ_n}{dx} = -\frac{1}{q}\frac{dJ_p}{dx} = R_L + R_{SRH}, \tag{1.31}$$

ensures that the carriers that contribute to the current also recombine. The formulas for R_L and R_{SRH} are given in section 1.6.3. We see that traps enter via the Poisson equation. In the case of the Gaussian trap distribution we need to evaluate the occupation of holes and electrons, which is given by the Fermi-Dirac distribution, for a Gaussian trap DOS. In this case an approximation by Paasch and Scheinert is used.[183]

In order to solve equations (1.30) and (1.31) numerically on a given set of grid points, one needs to discretize the equations, and treat the differential terms as combinations of linear functions, i.e. approximate derivatives as the difference between two grid points.[184] For a full device we

need to consider interfaces on both sides, for which the boundary conditions in the model are of the Dirichlet type, meaning the charge carrier densities are fixed at the electrodes.

The total current is a combination of drift and diffusion, plus, we need to relate the current to the carrier densities and electric field in the device.[180] This is done by the current flow equation for the electron current (J_n) and hole current (J_p) separately. These are:

$$J_n = q\mu_n nE + qD_n \frac{dn}{dx}. \tag{1.32a}$$

$$J_p = q\mu_p pE - qD_p \frac{dp}{dx}. \tag{1.32b}$$

Where the total current is the sum of J_n and J_p and $D_{n/p}$ is the carrier diffusion coefficient, which is related to the mobility by the Einstein relation: $D_{n/p} = \frac{\mu_{n/p} k_B T}{q}$.[185]

Using temperature dependent J-V measurements of single carrier diodes, the drift-diffusion solver can give the parameters of the mobility and trap density for both carrier species separately. The double carrier current follows from solving Poisson and continuity equations simultaneously, by combining the mobility parameters obtained from the single carrier devices.

I would like to note that we model our single carriers and OLEDs exclusively in steady state. This means carriers have enough time to equilibrate in the material DOS and that carrier populations, but also exciton populations, do not vary with time anymore. For commercial OLEDs transient effects will be relevant, as these applications are often electrically driven with a certain refresh rate, meaning the OLED operates in pulsed mode. This leads to transient effects, relating to for example carrier relaxation within the Gaussian DOS,[186,187] but these effects lie outside the relevance of this thesis.

1.6.7 Numerical drift-diffusion model part 2, exciton modelling

To describe the light output and concomitantly the efficiency of an OLED it is useful to get a description of the exciton population inside the device. This can be difficult, since, as we saw in section 1.5, there are many processes that an exciton can undergo during its lifetime, all with various rates. Kinetic equations are a popular approach to calculate exciton populations and they are also used throughout this thesis.[105,118,188] The singlet and triplet population under electrical excitation might be written as follows:

$$\frac{d[S(x,t)]}{dt} = 0.25 \cdot G(x,t) - \frac{[S(x,t)]}{\tau_s}. \tag{1.33a}$$

$$\frac{d[T(x,t)]}{dt} = 0.75 \cdot G(x,t) - \frac{[T(x,t)]}{\tau_t}. \tag{1.33b}$$

With τ_s the singlet lifetime and τ_t the triplet lifetime. Where the dependence on position inside the device x and time t are considered. The generation rate $G(x,t)$ is equal to the emissive recombination as discussed in section 1.6.3. Equations of this type can be solved for the exciton density using a finite element method, in steady state or even analytically.[189]

Annihilation processes are readily incorporated into the rate equations. Using TTA as an example, two triplets get lost with a probability of $0.25*k_{TTA}$, but a singlet is gained with the same probability. Next to that, one triplet is lost with a probability of $0.75*k_{TTA}$. The total effect can be described as a gain of

$$+0.25 \cdot k_{TTA} \cdot [T(x,t)]^2 \tag{1.33c}$$

to the singlet rate equation (1.33a) and a factor of:

$$-1.25 \cdot k_{TTA} \cdot [T(x,t)]^2 \tag{1.33d}$$

added to the triplet rate equation (1.33b). In similar fashion TPA, STA and any other interaction, such as those outlined in section 1.5.2 can be incorporated. Solving such an expression in steady state (equating it to 0) then gives the singlet and triplet population.

Knowing the optical and electrical part we can calculate the efficiency as:

$$\eta = \left(\frac{[S(x)]}{\tau_s}\right) \Big/ G(x). \tag{1.34}$$

With the full device operation described both optically and electrically, we can move to one of the focal points of this thesis, namely degradation of OLEDs.

1.7 Degradation

The focus of this PhD thesis lies on the investigation of how OLEDs behave under continuous electrical operation. Electrical degradation continues to be one of the most challenging subjects for OLEDs today, hindering the commercialization of new OLED materials as well as plaguing already commercial OLEDs. Historically, much focus has been on understanding the OLED from an electrical perspective or focusing on the outcoupling problem. In comparison to what we learned in those fields, our fundamental understanding on OLED degradation is still fairly limited, although good progress has been made. It goes without saying that it is extremely worthwhile to investigate this subject.

1.7.1 Intrinsic and extrinsic degradation

Before moving on, a clear distinction should be made between extrinsic and intrinsic effects. Extrinsic degradation refers to failure of the OLED due to for example water, oxygen or UV radiation,[190,191] whereas the term intrinsic degradation is used to describe what happens during prolonged *electrical* driving of an OLED. It is the intrinsic degradation we are interested in, as extrinsic effects can be perfectly controlled by encapsulation, and working in a glovebox and cleanroom environment.[192,193] When I hereafter refer to degradation, the intrinsic variant is always implied unless explicitly stated otherwise.

1.7.2 Degradation tests

To reliably assign degradation effects to the emitting layer, the working of an OLED must be assessed prior to running a degradation test on it. It usually suffices to confirm that the *J-V* and *EQE* curves are what one would expect in terms of shape and values.

During degradation experiments the OLED is kept under forward bias conditions, and the voltage and light output are monitored in time. For the purpose of comparing different OLEDs, there are two common routes to study degradation. The first approach is aging several OLEDs at the same initial luminance. Especially for OLEDs of the same thickness this is a good standardized method to probe the stability and it is often adopted in literature. For mechanistic investigations, however, it can be convenient to switch to degrading at the same aging current density (J_{age}) instead, which is what we do most of the time in the further chapters of this thesis. An advantage of the second method compared to the first approach is that the differences in optical outcoupling will not give variations in J_{age}, which is an inevitable result of aging at the same initial luminance. The standardized way to report the lifetime is via their '*LT*-value', where LT_{80} would mean the point in time where the sample reached 80% of its initial luminance.

1.7.3 Degradation mechanisms in OLEDs

Let's review our understanding of OLED degradation at present. One of the first papers on degradation by Parker et al. reported that if an OLED is kept at a constant current for an extended period of time, the voltage at which the OLED is operated increases, whereas simultaneously the light output decreases.[194] Soon after the observations of Parker et al. it was found that this drifting voltage and luminance behaviour were intrinsically linked, namely by the formation of charge traps during degradation. An increasing number of trapped carriers mean an ever higher voltage is needed to sustain the same current while the extra SRH recombination introduced through the traps explains at the same time the light decrease.[195] The trap formation in degraded PLEDs was later verified and even quantified numerically through analyzing *J-V* curves of degraded SY-PPV OLEDs.[196] Furthermore, traps were found in degraded phosphorescent OLEDs by MC simulations.[197] Later it was realized that traps also act as exciton quenchers, which is generally assessed by the change in PLQY from before and after degradation.[198] In PLEDs and single layer TADF OLEDs it is assumed that this effect becomes relevant at high trap densities only.

What actually happens to the emitter molecule during degradation depends on the chemical structure, more specifically, which chemical bonds the emitter consists of. Chemically we think of degradation as the breaking of (weak) bonds in molecules, effectively fragmenting the molecule.[199] The fragmented degradation products are likely to be radicals that attach to other molecules, in turn these can act as exciton quenchers and/or traps.[199–201] To dissociate a covalent bond one must supply an energy greater than the bond strength. Which bond gets dissociated and what the degradation products are in the end will determine the characteristics of the traps, such as the trap depth and the amount. There is the possibility that multiple degradation products exist with multiple trap depths. Some elegant studies used mass

spectrometry or time-of-flight techniques in order to identify these fragmented degradation products, which can provide valuable design rules for new stable emitters.[202–205]

Many underlying reasons for trap formation, or for OLED degradation in general, have been postulated. Most of them are associated with mechanisms that are able to produce high-energy particles, so that chemical bonds can be broken. Popular degradation mechanisms in this direction include TTA and TPA (or a combination),[135,202,206–214] but also degradation of the interface has been an extensive research topic.[191,193,208,215] Charge injecting and transporting layers have been reported to influence degradation in a variety of ways, for example through the accumulation of charges,[216–219] or via their triplet energy levels.[220] Furthermore, the same emitter degrades very differently in different types of hosts.[148,221] The situation is made even more complex in multilayered OLEDs, where there can be degradation of the many individual layers or interfaces, all in conjunction to the emitter degradation. Degradation is in itself already an extremely complex phenomenon, and we have to rely on measuring the effects of degradation indirectly in order to find out what is occurring inside the device. Assigning a degradation mechanism is only made more complicated by multilayer device architectures as well as doped systems. Drawing general conclusions or modelling degradation is held back by all these considerations and degradation studies would benefit tremendously from a simple device structure, as found in PLEDs, where the emitting layers sits between two electrodes of different work function, without any additional blocking or transport layers.

Having TTA or TPA as the main driving force behind degradation brings us to several general conclusions about degradation already. The fact that excitons play a role in degradation implies that higher energy excitons have the ability to break higher energy chemical bonds and therefore as a first rule blue emitters are the most unstable, in agreement with the generally observed trend.[214] Another implication is that exciton induced degradation happens in the bulk of the emitter, thus the lifetime should vary if the emitter thickness is changed. This criterion is often used to distinguish bulk degradation from interfacial degradation, since the latter shows no dependence on emitter layer thickness.[193]

To alleviate degradation many of the same strategies that we saw to counter roll-off can also be used to extend the lifetime. Therefore we can say that controlling the triplet distribution, for example by broadening the emission zone, is key to reach long lifetime OLEDs.[148,222–224]

1.8 Scope of this thesis

This thesis aims to further the understanding of OLED device physics and degradation, focussing mostly on TADF OLEDs. As mentioned already in **1.7**, a more fundamental insight into degradation processes is needed in order to prolong the stability of OLEDs, which is important for new as well as existing emitter materials.

In chapter 3 we address the role of triplets in PLED degradation and efficiency, both experimentally and using a device model. There is an open question in the mechanism of PLED degradation, namely which type of exciton (singlet or triplet) leads to trap formation. Furthermore, the effect of TTA on the efficiency has been found, but not properly quantified.

Experimentally, we judiciously blend various molecules in our active layer in order to control the singlet and triplet density separately. Numerically, we expand our rate equation model to include TTA for PLEDs. We prove the involvement of *triplet* excitons in the degradation of PLEDs, through trap formation via the triplet-polaron interaction. Regarding PLED efficiency we successfully quantify the role that TTA plays and we demonstrate the basic principles of rate equation modelling. This work forms the basis for further studies on more complex systems like TADF OLEDs.

Before moving to the degradation of TADF OLEDs, first, more insight into their device physics needs to be obtained. One major problem for TADF OLEDs, and one with a much-debated source, is the roll-off. In chapter 4 we carefully study the shape of the efficiency curve and complement it with a straightforward analytical theory. It is demonstrated that the roll-off is due to TTA only, and we are able to extract the corresponding quenching constant just from simple *J-V* and efficiency measurements.

Of course, an analytical formula is handy for physical insights, but the full device operation is a complex interplay of various processes, and for a full quantitative description of a TADF OLED, a numerical device model must be developed. This is what chapter 5 is about. The electrical part of the model is grounded in a position dependent numerical drift-diffusion solver commonly used for organic semiconductors, but it is coupled here for the first time with rate equations relevant to TADF materials. This turns out to be a powerful approach, as we are able to describe the voltage, temperature and thickness dependence of the current density and the efficiency. Through efficiency modelling we are able to extract a k_{TTA} value that coincides very well with an optically determined TTA rate constant.

In chapter 6 we use the predictive power of this comprehensive device model to study the degradation characteristics of TADF OLEDs. We show that the degradation characteristics can be consistently modelled by trap formation due to triplet-polaron annihilation, with a similar trap formation constant as was found for PLEDs. Our model allows us to quantitatively predict the effect of a broadened triplet distribution inside the active layer. With this understanding we fabricate a device that shows unprecedented stability for single-layer TADF OLEDs.

References

[1] M. Pope, H. P. Kallmann, P. Magnante, *J. Chem. Phys.* **1963**, *38*, 2042.

[2] C. W. Tang, S. A. Vanslyke, *Appl. Phys. Lett.* **1987**, *51*, 913.

[3] J. H. Burroughes, D. D. C. Bradley, A. R. Brown, R. N. Marks, K. Mackay, R. H. Friend, P. L. Burns, A. B. Holmes, *Nature* **1990**, *347*, 539.

[4] M. A. Baldo, D. F. O'Brien, Y. You, A. Shoustikov, S. Sibley, M. E. Thompson, S. R. Forrest, *Nature* **1998**, *395*, 151.

[5] C. Adachi, M. A. Baldo, M. E. Thompson, S. R. Forrest, *J. Appl. Phys.* **2001**, *90*, 5048.

[6] K. Goushi, K. Yoshida, K. Sato, C. Adachi, *Nat. Photonics* **2012**, *6*, 253.

[7] H. Uoyama, K. Goushi, K. Shizu, H. Nomura, C. Adachi, *Nature* **2012**, *492*, 234.

[8] G. Hong, X. Gan, C. Leonhardt, Z. Zhang, J. Seibert, J. M. Busch, S. Bräse, *Adv. Mater.* **2021**, *33*.

[9] G. Yu, J. Gao, J. C. Hummelen, F. Wudl, A. J. Heeger, **1995**, 1789.

[10] H. Klauk, *Chem. Soc. Rev.* **2010**, *39*, 2643.

[11] M. Lindorf, K. A. Mazzio, J. Pflaum, K. Nielsch, W. Brütting, M. Albrecht, *J. Mater. Chem. A* **2020**, *8*, 7495.

[12] O. Bubnova, X. Crispin, *Energy Environ. Sci.* **2012**, *5*, 9345.

[13] A. Köhler, H. Bässler, *Electronic Processes in Organic Semiconductors: An Introduction*, Wiley-VCH Verlag GmbH & Co. KGaA, Weinheim, **2015**.

[14] P. Atkins, J. de Paula, *Physical Chemistry*, W. H. Freeman Company, New York, **2006**.

[15] P. Atkins, R. Friedman, *Molecular Quantum Mechanics*, Oxford University Press, **2012**.

[16] W. P. Su, J. R. Schrieffer, A. J. Heeger, *Phys. Rev. Lett.* **1979**, *42*, 1698.

[17] A. Köhler, S. T. Hoffmann, H. Bässler, *J. Am. Chem. Soc.* **2012**, *134*, 11594.

[18] J. L. Bredas, *Mater. Horizons* **2014**, *1*, 17.

[19] H. Spreitzer, H. Becker, E. Kluge, W. Kreuder, H. Schenk, R. Demandt, H. Schoo, *Adv. Mater.* **1998**, *10*, 1340.

[20] D. Braun, A. J. Heeger, *Appl. Phys. Lett.* **1991**, *58*, 1982.

[21] N. Dieter, *Macromol. Rapid Commun.* **2001**, *22*, 1365.

[22] P. W. M. Blom, *Adv. Mater. Technol.* **2020**, *5*, 1.

[23] S. Fratini, M. Nikolka, A. Salleo, G. Schweicher, H. Sirringhaus, *Nat. Mater.* **2020**, *19*,

491.

[24] H. Bronstein, C. B. Nielsen, B. C. Schroeder, I. McCulloch, *Nat. Rev. Chem.* **2020**.

[25] J. L. Brédas, D. Beljonne, V. Coropceanu, J. Cornil, *Chem. Rev.* **2004**, *104*, 4971.

[26] I. N. Hulea, H. B. Brom, A. J. Houtepen, D. Vanmaekelbergh, J. J. Kelly, E. A. Meulenkamp, **2004**, 16.

[27] H. Bässler, A. Köhler, in *Unimolecular Supramol. Electron. I Chem. Phys. Meet Met. Interfaces* (Ed.: R.M. Metzger), Springer Berlin Heidelberg, Berlin, Heidelberg, **2012**, pp. 1–65.

[28] C. Kittel, *Introduction to Solid State Physics*, John Wiley & Sons, Inc, **2005**.

[29] E. M. Conwell, *Phys. Rev.* **1956**, *103*.

[30] N. F. Mott, *Can. J. Phys.* **1956**, *34*.

[31] E. Collini, G. D. Scholes, *Science (80-.).* **2009**, *323*.

[32] S. M. Sze, K. N. Kwok, *Physics of Semiconductor Devices*, John Wiley & Sons, Inc, Hoboken, New Jersey, **2007**.

[33] S. Fratini, D. Mayou, S. Ciuchi, *Adv. Funct. Mater.* **2016**, *26*, 2292.

[34] S. Ciuchi, S. Fratini, D. Mayou, *Phys. Rev. B - Condens. Matter Mater. Phys.* **2011**, *83*, 1.

[35] P. W. M. Blom, M. C. J. M. Vissenberg, **2000**, *27*.

[36] P. W. M. Blom, M. J. M. De Jong, C. T. H. F. Liedenbaum, *Polym. Adv. Technol.* **1998**, *9*, 390.

[37] V. D. Mihailetchi, H. Xie, B. De Boer, L. J. A. Koster, P. W. M. Blom, *Adv. Funct. Mater.* **2006**, *16*, 699.

[38] V. Coropceanu, J. Cornil, D. A. da Silva Filho, Y. Olivier, R. Silbey, and Jean-Luc Brédas, *Chem. Rev.* **2007**, *107*.

[39] D. Emin, *Polarons*, Cambridge University Press, Cambridge, **2012**.

[40] H. Bässler, A. Köhler, *Charge Carrier Mobility in Amorphous Organic Semiconductors*, Woodhead Publishing Limited, **2013**.

[41] A. Miller, E. Abrahams, *Phys. Rev.* **1960**, *120*, 745.

[42] R. A. Marcus, N. Sutin, *Biochim. Biophys. Acta - Rev. Bioenerg.* **1985**, *811*, 265.

[43] X. De Vries, P. Friederich, W. Wenzel, R. Coehoorn, P. A. Bobbert, *Phys. Rev. B* **2018**, *97*, 1.

[44] H. Bässler, *Polym. Adv. Technol.* **1998**, *9*, 402.

[45] H. Bässler, *Phys. Status Solidi* **1993**, *175*, 15.

[46] V. I. Arkhipov, E. V. Emelianova, H. Bässler, *Philos. Mag. B Phys. Condens. Matter; Stat. Mech. Electron. Opt. Magn. Prop.* **2001**, *81*, 985.

[47] P. W. M. Blom, N. I. Craciun, D. M. De Leeuw, G. A. H. Wetzelaer, H. T. Nicolai, M. Kuik, *Adv. Mater.* **2014**, *26*, 512.

[48] C. Tanase, E. J. Meijer, P. W. M. Blom, D. M. de Leeuw, *Phys. Rev. Lett.* **2003**, *91*, 1.

[49] C. Tanase, P. W. M. Blom, D. M. De Leeuw, *Phys. Rev. B - Condens. Matter Mater. Phys.* **2004**, *70*, 1.

[50] N. I. Craciun, J. J. Brondijk, P. W. M. Blom, *Phys. Rev. B - Condens. Matter Mater. Phys.* **2008**, *77*, 1.

[51] W. F. Pasveer, J. Cottaar, C. Tanase, R. Coehoorn, P. A. Bobbert, P. W. M. Blom, M. De Leeuw, M. A. J. Michels, *Phys. Rev. Lett.* **2005**, *94*, 1.

[52] S. L. M. Van Mensfoort, S. I. E. Vulto, R. A. J. Janssen, R. Coehoorn, *Phys. Rev. B - Condens. Matter Mater. Phys.* **2008**, *78*, 1.

[53] R. Coehoorn, W. F. Pasveer, P. A. Bobbert, M. A. J. Michels, *Phys. Rev. B - Condens. Matter Mater. Phys.* **2005**, *72*.

[54] N. I. Craciun, J. Wildeman, P. W. M. Blom, *Phys. Rev. Lett.* **2008**, *100*

[55] and D. A. Pascal Kordt , Jeroen J. M. van der Holst , Mustapha Al Helwi , Wolfgang Kowalsky , Falk May , Alexander Badinski , Christian Lennartz, *Adv. Funct. Mater.* **2017**, 101.

[56] H. T. Nicolai, A. Hof, J. L. M. Oosthoek, P. W. M. Blom, *Adv. Funct. Mater.* **2011**, *21*, 1505.

[57] D. K. Mangalore, P. W. M. Blom, G. J. A. H. Wetzelaer, *APL Mater.* **2019**, *7*.

[58] M. Kuik, J. Vandenbergh, L. Goris, E. J. Begemann, L. Lutsen, D. J. M. Vanderzande, J. V Manca, P. W. M. Blom, *Appl. Phys. Lett.* **2011**, *99*, 0.

[59] C. Tanase, P. W. M. Blom, D. M. De Leeuw, E. J. Meijer, *Phys. Status Solidi Appl. Res.* **2004**, *201*, 1236.

[60] D. Abbaszadeh, P. W. M. Blom, *Adv. Electron. Mater.* **2016**, *2*, 1.

[61] D. Abbaszadeh, A. Kunz, G. A. H. Wetzelaer, J. J. Michels, N. I. Craciun, K. Koynov, I. Lieberwirth, P. W. M. Blom, *Nat. Mater.* **2016**, *15*, 628.

[62] J. C. Blakesley, H. S. Clubb, N. C. Greenham, *Phys. Rev. B - Condens. Matter Mater. Phys.* **2010**, *81*, 1.

[63] E. Knapp, R. Häusermann, H. U. Schwarzenbach, B. Ruhstaller, *J. Appl. Phys.* **2010**, *108*.

[64] J. Meyer, S. Hamwi, M. Kröger, W. Kowalsky, T. Riedl, A. Kahn, *Adv. Mater.* **2012**, *24*, 5408.

[65] J. C. Blakesley, N. C. Greenham, *J. Appl. Phys.* **2009**, *106*.

[66] J. G. Simmons, *J. Phys. Chem. Solids* **1971**, *30*, 2581.

[67] M. Fahlman, S. Fabiano, V. Gueskine, D. Simon, M. Berggren, X. Crispin, *Nat. Rev. Mater.* **2019**, *4*, 627.

[68] H. Ishii, K. Sugiyama, E. Ito, K. Seki, *Adv. Mater.* **1999**, *11*, 605.

[69] I. Lange, J. C. Blakesley, J. Frisch, A. Vollmer, N. Koch, D. Neher, *Phys. Rev. Lett.* **2011**, *106*, 1.

[70] M. Oehzelt, N. Koch, G. Heimel, *Nat. Commun.* **2014**, *5*, 1.

[71] P. De Bruyn, A. H. P. Van Rest, G. A. H. Wetzelaer, D. M. De Leeuw, P. W. M. Blom, *Phys. Rev. Lett.* **2013**, *111*, 1.

[72] K. C. Kao, W. Hwang, *Electrical Transport in Solids with Particular Reference to Organic Semiconductors*, Pergamon Press, Oxford, New York, Toronto, Sydney, Paris, Frankfurt, **1981**.

[73] L. Lindell, C. Vahlberg, K. Uvdal, M. Fahlman, S. Braun, *J. Electron Spectros. Relat. Phenomena* **2015**, *204*, 140.

[74] N. B. Kotadiya, H. Lu, A. Mondal, Y. Ie, D. Andrienko, P. W. M. Blom, G. J. A. H. Wetzelaer, *Nat. Mater.* **2018**, *17*, 329.

[75] K. Zhang, N. B. Kotadiya, X. Y. Wang, G. J. A. H. Wetzelaer, T. Marszalek, W. Pisula, P. W. M. Blom, *Adv. Electron. Mater.* **2020**, *6*.

[76] G. A. H. Wetzelaer, P. W. M. Blom, *Phys. Rev. B - Condens. Matter Mater. Phys.* **2014**, *89*, 1.

[77] N. F. Mott, R. W. Gurney, *Electronic Processes in Ionic Crystals*, Oxford University Press, London, **1948**.

[78] M. A. Lampert, P. Mark, *Current Injection in Solids*, (Academic Press, New York, **n.d.**

[79] R. Coehoorn, P. A. Bobbert, *Phys. Status Solidi Appl. Mater. Sci.* **2012**, *209*, 2354.

[80] N. I. Craciun, Y. Zhang, A. Palmaerts, H. T. Nicolai, M. Kuik, R. J. P. Kist, G. A. H. Wetzelaer, J. Wildeman, J. Vandenbergh, L. Lutsen, D. Vanderzande, P. W. M. Blom, *J. Appl. Phys.* **2010**, *107*.

[81] P. Mark, W. Helfrich, *J. Appl. Phys.* **1962**, *33*, 205.

[82] M. M. Mandoc, B. de Boer, G. Paasch, P. W. M. Blom, *Phys. Rev. B* **2007**, *75*, 12.

[83] H. T. Nicolai, M. M. Mandoc, P. W. M. Blom, *Phys. Rev. B - Condens. Matter Mater. Phys.* **2011**, *83*, 1.

[84] A. Sussman, *J. Appl. Phys.* **1967**, *38*, 2738.

[85] H. P. D. Lanyon, *Phys. Rev.* **1963**, *130*, 134.

[86] S. NeŠpůrek, P. Smejtek, *Czechoslov. J. Phys.* **1972**, *22*, 160.

[87] N. B. Kotadiya, A. Mondal, P. W. M. M. Blom, D. Andrienko, G. J. A. H. H. Wetzelaer, *Nat. Mater.* **2019**, *18*, 1182.

[88] M. Diethelm, M. Bauer, W. H. Hu, C. Vael, S. Jenatsch, P. W. M. Blom, F. Nüesch, R. Hany, *Adv. Funct. Mater.* **2022**, *32*.

[89] N. B. Kotadiya, P. W. M. Blom, G.-J. A. H. Wetzelaer, *Nat. Photonics* **2019**, 1.

[90] and M. S. M. Meier, S. Karg, K. Zuleeg, W. Brütting, M. Meier, S. Karg, K. Zuleeg, W. Brütting, M. Schwoerer, *J. Appl. Phys.* **1998**, *84*, 87.

[91] W. Brütting, *Physics of Organic Semiconductors*, Wiley-VCH Verlag GmbH & Co. KGaA, Weinheim, **2005**.

[92] W. Graupner, G. Leditzky, G. Leising, U. Scherf, *Phys. Rev. B - Condens. Matter Mater. Phys.* **1996**, *54*, 7610.

[93] A. Köhler, H. Bässler, *Mater. Sci. Eng. R Reports* **2009**, *66*, 71.

[94] A. Köhler, H. Bässler, *J. Mater. Chem.* **2011**, *21*, 4003.

[95] R. Pauncz, *Spin Eigenfunctions: Construction and Use*, Plenum Press, London, New York, **1979**.

[96] M. Pope, C. E. Swenberg, *Electronic Processes in Organic Crystals and Polymers*, Oxford University Press, Oxford, **1999**.

[97] I. Rörich, O. V Mikhnenko, D. Gehrig, P. W. M. Blom, N. I. Crăciun, *J. Phys. Chem. B* **2017**, *121*, 1405.

[98] R. Englman, J. Jortner, *Mol. Phys.* **1970**, *18*, 285.

[99] M. A. Baldo, S. Lamansky, P. E. Burrows, M. E. Thompson, S. R. Forrest, *Appl. Phys. Lett.* **1999**, *75*, 4.

[100] C. Adachi, M. A. Baldo, S. R. Forrest, S. Lamansky, M. E. Thompson, R. C. Kwong, *Appl. Phys. Lett.* **2001**, *78*, 1622.

[101] F. B. Dias, T. J. Penfold, A. P. Monkman, *Methods Appl. Fluoresc.* **2017**, *5*, 012001.

[102] T. J. Penfold, *J. Phys. Chem. C* **2015**, *119*, 13535.

[103] F. B. Dias, T. J. Penfold, A. P. Monkman, *Methods Appl. Fluoresc.* **2018**, 425.

[104] T. Hatakeyama, K. Shiren, K. Nakajima, S. Nomura, S. Nakatsuka, K. Kinoshita, J. Ni, Y. Ono, T. Ikuta, *Adv. Mater.* **2016**, *28*, 2777.

[105] S. Sem, S. Jenatsch, K. Stavrou, A. Danos, A. P. Monkman, B. Ruhstaller, *J. Mater. Chem. C* **2022**, *10*, 4878.

[106] K. Thakur, B. van der Zee, G. J. A. H. Wetzelaer, C. Ramanan, P. W. M. Blom, *Adv. Opt. Mater.* **2022**, *10*.

[107] T. Serevičius, R. Skaisgiris, G. Kreiza, J. Dodonova, K. Kazlauskas, E. Orentas, S. Tumkevičius, S. Juršenas, *J. Phys. Chem. A* **2021**, *125*, 1637.

[108] H. Noda, X. Chen, H. Nakanotani, T. Hosokai, M. Miyajima, N. Notsuka, Y. Kashima, J. Brédas, C. Adachi, *Nat. Mater.* **2019**.

[109] T. Kobayashi, D. Kawate, A. Niwa, T. Nagase, K. Goushi, C. Adachi, H. Naito, *Phys. Status Solidi Appl. Mater. Sci.* **2020**, *217*, 1.

[110] B. T. Lim, S. Okajima, A. K. Chandra, E. C. Lim, *Chem. Phys. Lett.* **1981**, *79*, 22.

[111] B. H. Drummond, N. Aizawa, Y. Zhang, W. K. Myers, Y. Xiong, M. W. Cooper, S. Barlow, Q. Gu, L. R. Weiss, A. J. Gillett, D. Credgington, Y. J. Pu, S. R. Marder, E. W. Evans, *Nat. Commun.* **2021**, *12*, 1.

[112] F. B. Dias, J. Santos, D. R. Graves, P. Data, R. S. Nobuyasu, M. A. Fox, A. S. Batsanov, T. Palmeira, M. N. Berberan-Santos, M. R. Bryce, A. P. Monkman, *Adv. Sci.* **2016**, *3*, 1.

[113] Y. Olivier, B. Yurash, L. Muccioli, G. D'Avino, O. Mikhnenko, J. C. Sancho-García, C. Adachi, T. Q. Nguyen, D. Beljonne, *Phys. Rev. Mater.* **2017**, *1*, 1.

[114] E. Zysman-Colman, *Nat. Photonics* **2020**, *14*, 593.

[115] M. K. Etherington, J. Gibson, H. F. Higginbotham, T. J. Penfold, A. P. Monkman, *Nat. Commun.* **2016**, *7*, 1.

[116] T. J. Penfold, E. Gindensperger, C. Daniel, C. M. Marian, *Chem. Rev.* **2018**, *118*, 6975.

[117] J. Gibson, A. P. Monkman, T. J. Penfold, *ChemPhysChem* **2016**, *17*, 2956.

[118] N. Haase, A. Danos, C. Pflumm, A. Morherr, P. Stachelek, A. Mekic, W. Brütting, A. P. Monkman, *J. Phys. Chem. C* **2018**, *122*, 29173.

[119] J. Eng, T. J. Penfold, *Commun. Chem.* **2021**, *4*, 21.

[120] J. U. Kim, I. S. Park, C. Y. Chan, M. Tanaka, Y. Tsuchiya, H. Nakanotani, C. Adachi, *Nat. Commun.* **2020**, *11*.

[121] C. Y. Chan, M. Tanaka, Y. T. Lee, Y. W. Wong, H. Nakanotani, T. Hatakeyama, C. Adachi, *Nat. Photonics* **2021**.

[122] T. Förster, *Ann. Phys.* **1948**, *437*, 55.

[123] T. Förster, *Zeitschrift fur Naturforsch. - Sect. A J. Phys. Sci.* **1949**, *4*, 321.

[124] D. L. Dexter, *J. Chem. Phys.* **1953**, *21*, 836.

[125] R. Saxena, T. Meier, S. Athanasopoulos, H. Bässler, A. Köhler, *Phys. Rev. Appl.* **2020**, *14*, 1.

[126] B. H. Wallikewitz, D. Kabra, S. Gélinas, R. H. Friend, *Phys. Rev. B - Condens. Matter Mater. Phys.* **2012**, *85*, 22.

[127] S. T. Hoffmann, J. M. Koenen, U. Scherf, I. Bauer, P. Strohriegl, H. Bässler, A. Köhler, *J. Phys. Chem. B* **2011**, *115*, 8417.

[128] D. Y. Kondakov, *Philos. Trans. R. Soc. A Math. Phys. Eng. Sci.* **2015**, *373*.

[129] M. A. Baldo, C. Adachi, S. R. Forrest, *Phys. Rev. B - Condens. Matter Mater. Phys.* **2000**, *62*, 10967.

[130] Y. Zhang, S. R. Forrest, *Chem. Phys. Lett.* **2013**, *590*, 106.

[131] A. Niwa, S. Haseyama, T. Kobayashi, T. Nagase, K. Goushi, C. Adachi, H. Naito, *Appl. Phys. Lett.* **2018**, *113*.

[132] L. Zhang, H. Van Eersel, P. A. Bobbert, R. Coehoorn, *Chem. Phys. Lett.* **2016**, *652*, 142.

[133] N. C. Giebink, Y. Sun, S. R. Forrest, *Org. Electron. physics, Mater. Appl.* **2006**, *7*, 375.

[134] W. Staroske, M. Pfeiffer, K. Leo, M. Hoffmann, *Phys. Rev. Lett.* **2007**, *98*, 8.

[135] M. Hasan, S. Saggar, A. Shukla, F. Bencheikh, J. Sobus, S. K. M. McGregor, C. Adachi, S. C. Lo, E. B. Namdas, *Nat. Commun.* **2022**, *13*, 1.

[136] D. Hertel, K. Meerholz, *J. Phys. Chem. B* **2007**, *111*, 12075.

[137] M. Hasan, A. Shukla, V. Ahmad, J. Sobus, F. Bencheikh, S. K. M. McGregor, M. Mamada, C. Adachi, S. C. Lo, E. B. Namdas, *Adv. Funct. Mater.* **2020**, *30*, 1.

[138] H. Van Eersel, P. A. Bobbert, R. A. J. Janssen, R. Coehoorn, *Appl. Phys. Lett.* **2014**, *105*.

[139] S. Reineke, K. Walzer, K. Leo, *Phys. Rev. B - Condens. Matter Mater. Phys.* **2007**, *75*, 1.

[140] S. Wehrmeister, L. Jäger, T. Wehlus, A. F. Rausch, T. C. G. Reusch, T. D. Schmidt, W. Brütting, *Phys. Rev. Appl.* **2015**, *3*, 1.

[141] Y. Zhang, S. R. Forrest, *Phys. Rev. Lett.* **2012**, *108*, 1.

[142] K. Masui, H. Nakanotani, C. Adachi, *Org. Electron. physics, Mater. Appl.* **2013**, *14*, 2721.

[143] C. Murawski, K. Leo, M. C. Gather, *Adv. Mater.* **2013**, *25*, 6801.

[144] B. Dick, B. Nickel, *Chem. Phys.* **1983**, *78*, 1.

[145] T. Yonehara, K. Goushi, T. Sawabe, I. Takasu, C. Adachi, *Jpn. J. Appl. Phys.* **2015**, *54*.

[146] H. Van Eersel, P. A. Bobbert, R. Coehoorn, *J. Appl. Phys.* **2015**, *117*.

[147] B. S. B. Karunathilaka, U. Balijapalli, C. A. M. Senevirathne, S. Yoshida, Y. Esaki, K. Goushi, T. Matsushima, A. S. D. Sandanayaka, C. Adachi, *Nat. Commun.* **2020**, *11*, 1.

[148] L. S. Cui, S. Bin Ruan, F. Bencheikh, R. Nagata, L. Zhang, K. Inada, H. Nakanotani, L. S. Liao, C. Adachi, *Nat. Commun.* **2017**, *8*, 1.

[149] Y. Zhang, M. Slootsky, S. R. Forrest, *Appl. Phys. Lett.* **2011**, *99*, 4.

[150] T. Furukawa, H. Nakanotani, M. Inoue, C. Adachi, *Sci. Rep.* **2015**, *5*, 8429.

[151] N. C. Erickson, R. J. Holmes, *Adv. Funct. Mater.* **2014**, *24*, 6074.

[152] C. J. Bardeen, C. Chen, J. Lee, M. Leung, N. T. Tierce, T. Chiu, C. Lin, *Adv. Mater.* **2018**, *30*, 1804850.

[153] P. W. M. Blom, M. J. M. De Jong, **1998**, *4*, 105.

[154] R. M. Lawrence, A. L. Murray, *J. Appl. Phys.* **1970**, *41*, 508.

[155] P. Langevin, *Ann. Chim. Phys* **1903**, *28*, 433.

[156] P. W. M. Blom, M. J. M. De Jong, S. Breedijk, *Appl. Phys. Lett.* **1997**, *71*, 930.

[157] J. J. M. Van Der Holst, F. W. A. Van Oost, R. Coehoorn, P. A. Bobbert, *Phys. Rev. B - Condens. Matter Mater. Phys.* **2009**, *80*, 1.

[158] U. Albrecht, H. Bässler, **1995**, *455*, 455.

[159] W. Shockley, W. T. Read, *Phys. Rev.* **1952**, *87*, 835.

[160] R. N. Hall, *Phys Rev* **1952**, *87*, 387.

[161] G. A. H. Wetzelaer, M. Kuik, H. T. Nicolai, P. W. M. Blom, *Phys. Rev. B - Condens. Matter Mater. Phys.* **2011**, *83*, 1.

[162] G. J. A. H. Wetzelaer, N. J. Van Der Kaap, J. A. Koster, P. W. M. Blom, *Adv. Energy Mater.* **2013**, *3*, 1130.

[163] W. Brütting, J. Frischeisen, T. D. Schmidt, B. J. Scholz, C. Mayr, *Phys. Status Solidi Appl. Mater. Sci.* **2013**, *210*, 44.

[164] J. S. Kim, P. K. H. Ho, N. C. Greenham, R. H. Friend, *J. Appl. Phys.* **2000**, *88*, 1073.

[165] W. L. Barnes, A. Dereux, T. W. Ebbesen, *Nature* **2003**, *424*, 824.

[166] D. Abbaszadeh, G. A. H. Wetzelaer, H. T. Nicolai, P. W. M. Blom, *J. Appl. Phys.* **2014**, *116*, 1.

[167] D. E. Markov, P. W. M. Blom, *Appl. Phys. Lett.* **2005**, *87*, 1.

[168] F. Tenopala-Carmona, O. S. Lee, E. Crovini, A. M. Neferu, C. Murawski, Y. Olivier, E. Zysman-Colman, M. C. Gather, *Adv. Mater.* **2021**, *33*.

[169] M. Furno, R. Meerheim, S. Hofmann, B. Lüssem, K. Leo, *Phys. Rev. B - Condens. Matter Mater. Phys.* **2012**, *85*, 1.

[170] Y. Li, N. B. Kotadiya, B. van der Zee, P. W. M. Blom, G. J. A. H. Wetzelaer, *Adv. Opt. Mater.* **2021**, *9*, 1.

[171] S. Hofmann, B. Lüssem, M. Furno, K. Leo, R. Meerheim, *Appl. Phys. Lett.* **2010**, *97*, 253305.

[172] B. Van der Zee, Y. Li, G. J. A. H. Wetzelaer, P. W. M. Blom, *Adv. Mater.* **2022**, *34*.

[173] N. Chitraningrum, T. Y. Chu, P. T. Huang, T. C. Wen, T. F. Guo, *Org. Electron. physics, Mater. Appl.* **2018**, *62*, 505.

[174] D. Y. Kondakov, T. D. Pawlik, T. K. Hatwar, J. P. Spindler, *J. Appl. Phys.* **2009**, *106*, DOI: 10.1063/1.3273407.

[175] S. Sinha, A. P. Monkman, *Appl. Phys. Lett.* **2003**, *82*, 4651.

[176] D. Di, L. Yang, J. M. Richter, L. Meraldi, R. M. Altamimi, A. Y. Alyamani, D. Credgington, K. P. Musselman, J. L. MacManus-Driscoll, R. H. Friend, *Adv. Mater.* **2017**, *29*.

[177] C. J. Chiang, A. Kimyonok, M. K. Etherington, G. C. Griffiths, V. Jankus, F. Turksoy, A. P. Monkman, *Adv. Funct. Mater.* **2013**, *23*, 739.

[178] I. Rörich, A. K. Schönbein, D. K. Mangalore, A. Halda Ribeiro, C. Kasparek, C. Bauer, N. I. Crăciun, P. W. M. Blom, C. Ramanan, *J. Mater. Chem. C* **2018**, *6*, 10569.

[179] Y. Li, O. Sachnik, B. van der Zee, K. Thakur, C. Ramanan, G. J. A. H. Wetzelaer, P. W. M. Blom, *Adv. Opt. Mater.* **2021**, *9*.

[180] L. J. A. Koster, E. C. P. Smits, V. D. Mihailetchi, P. W. M. Blom, *Phys. Rev. B - Condens. Matter Mater. Phys.* **2005**, *72*, 1.

[181] V. Rühle, A. Lukyanov, F. May, M. Schrader, T. Vehoff, J. Kirkpatrick, B. Baumeier, D. Andrienko, *J. Chem. Theory Comput.* **2011**, *7*, 3335.

[182] J. J. M. Van Der Holst, M. A. Uijttewaal, R. Balasubramanian, R. Coehoorn, P. A. Bobbert, G. A. De Wijs, R. A. De Groot, *Phys. Rev. B - Condens. Matter Mater. Phys.* **2009**, *79*, 1.

[183] G. Paasch, S. Scheinert, *J. Appl. Phys.* **2010**, *107*.

[184] S. Selberherr, *Analysis and Simulation of Semiconductor Devices*, **2013**.

[185] G. A. H. Wetzelaer, L. J. A. Koster, P. W. M. Blom, *Phys. Rev. Lett.* **2011**, *107*, 1.

[186] W. C. Germs, J. J. M. Van Der Holst, S. L. M. Van Mensfoort, P. A. Bobbert, R. Coehoorn, *Phys. Rev. B - Condens. Matter Mater. Phys.* **2011**, *84*, 1.

[187] M. Mesta, C. Schaefer, J. De Groot, J. Cottaar, R. Coehoorn, P. A. Bobbert, *Phys. Rev. B - Condens. Matter Mater. Phys.* **2013**, *88*, 1.

[188] R. Scholz, P. Kleine, R. Lygaitis, L. Popp, S. Lenk, M. K. Etherington, A. P. Monkman, S. Reineke, *J. Phys. Chem. A* **2020**, *124*, 1535.

[189] Y. Tsuchiya, S. Diesing, F. Bencheikh, Y. Wada, P. L. dos Santos, H. Kaji, E. Zysman-Colman, I. D. W. Samuel, C. Adachi, *J. Phys. Chem. A* **2021**, *125*, 8074.

[190] S. Sudheendran Swayamprabha, D. K. Dubey, Shahnawaz, R. A. K. Yadav, M. R. Nagar, A. Sharma, F. C. Tung, J. H. Jou, *Adv. Sci.* **2021**, *8*, 1.

[191] A. Turak, *RSC Adv.* **2013**, *3*, 6188.

[192] S. Schmidbauer, A. Hohenleutner, B. König, *Adv. Mater.* **2013**, *25*, 2114.

[193] F. So, D. Kondakov, *Adv. Mater.* **2010**, *22*, 3762.

[194] I. D. Parker, *J. Appl. Phys.* **1994**, *75*, 1656.

[195] G. C. M. Silvestre, M. T. Johnson, A. Giraldo, J. M. Shannon, *Appl. Phys. Lett.* **2001**, *78*, 1619.

[196] Q. Niu, G. J. A. H. Wetzelaer, P. W. M. Blom, N. I. Crăciun, *Adv. Electron. Mater.* **2016**, *2*, 1.

[197] C. Hauenstein, S. Gottardi, E. Torun, R. Coehoorn, H. van Eersel, *Front. Chem.* **2022**, *9*, 1.

[198] I. Rörich, Q. Niu, B. van der Zee, E. del Pino Rosendo, N. I. Crăciun, C. Ramanan, P. W. M. Blom, *Adv. Electron. Mater.* **2020**, *1700643*, 1.

[199] D. Y. Kondakov, *J. Appl. Phys.* **2008**, *104*.

[200] D. Y. Kondakov, T. D. Pawlik, W. F. Nichols, W. C. Lenhart, *J. Soc. Inf. Disp.* **2007**, *16*, 37.

[201] D. Y. Kondakov, W. C. Lenhart, W. F. Nichols, *J. Appl. Phys.* **2007**, *101*.

[202] C. Jeong, C. Coburn, M. Idris, Y. Li, P. I. Djurovich, M. E. Thompson, S. R. Forrest, *Org. Electron. physics, Mater. Appl.* **2019**, *64*, 15.

[203] D. Y. Kondakov, C. T. Brown, T. D. Pawlik, V. V. Jarikov, *J. Appl. Phys.* **2010**, *107*.

[204] I. Rabelo, D. Moraes, S. Scholz, B. Lüssem, K. Leo, *Org. Electron.* **2011**, *12*, 341.

[205] S. C. Dong, L. Xu, C. W. Tang, *Org. Electron. physics, Mater. Appl.* **2017**, *42*, 379.

[206] B. Sim, J. S. Kim, H. Bae, S. Nam, E. Kwon, J. W. Kim, H. Y. Cho, S. Kim, J. J. Kim, *Phys. Rev. Appl.* **2020**, *14*, 1.

[207] K. Yang, S. Nam, J. Kim, E. S. Kwon, Y. Jung, H. Choi, J. W. Kim, J. Lee, *Adv. Funct. Mater.* **2022**, *32*, 1.

[208] S. Scholz, D. Kondakov, B. Lüssem, K. Leo, *Chem. Rev.* **2015**, *115*, 8449.

[209] J. Lee, C. Jeong, T. Batagoda, C. Coburn, M. E. Thompson, S. R. Forrest, *Nat. Commun.* **2017**, *8*, 1.

[210] M. Tanaka, R. Nagata, H. Nakanotani, C. Adachi, *Commun. Mater.* **2020**, *1*, 1.

[211] C. Y. Chan, M. Tanaka, H. Nakanotani, C. Adachi, *Nat. Commun.* **2018**, *9*, 2.

[212] M. Tanaka, H. Noda, H. Nakanotani, C. Adachi, *Adv. Electron. Mater.* **2019**, *5*, 1.

[213] Q. Niu, R. Rohloff, G. A. H. Wetzelaer, P. W. M. Blom, N. I. Crăciun, *Nat. Mater.* **2018**, *17*, 557.

[214] N. C. Giebink, B. W. D'Andrade, M. S. Weaver, P. B. MacKenzie, J. J. Brown, M. E. Thompson, S. R. Forrest, *J. Appl. Phys.* **2008**, *103*.

[215] A. Gassmann, S. V Yampolskii, A. Klein, K. Albe, N. Vilbrandt, O. Pekkola, Y. A. Genenko, M. Rehahn, H. Von Seggern, *Mater. Sci. Eng. B Solid-State Mater. Adv. Technol.* **2015**, *192*, 26.

[216] T. H. Han, W. Song, T. W. Lee, *ACS Appl. Mater. Interfaces* **2015**, *7*, 3117.

[217] R. Meerheim, S. Scholz, S. Olthof, G. Schwartz, S. Reineke, K. Walzer, K. Leo, *J. Appl. Phys.* **2008**, *104*.

[218] H. Zamani Siboni, Y. Luo, H. Aziz, *J. Appl. Phys.* **2011**, *109*.

[219] H. Zamani Siboni, H. Aziz, *Org. Electron. physics, Mater. Appl.* **2011**, *12*, 2056.

[220] H. Fukagawa, T. Shimizu, H. Kawano, S. Yui, T. Shinnai, A. Iwai, K. Tsuchiya, T. Yamamoto, *J. Phys. Chem. C* **2016**, *120*, 18748.

[221] S. G. Ihn, N. Lee, S. O. Jeon, M. Sim, H. Kang, Y. Jung, D. H. Huh, Y. M. Son, S. Y. Lee, M. Numata, H. Miyazaki, R. Gómez-Bombarelli, J. Aguilera-Iparraguirre, T. Hirzel, A. Aspuru-Guzik, S. Kim, S. Lee, *Adv. Sci.* **2017**, *4*, 1.

[222] Y. Zhang, J. Lee, S. R. Forrest, *Nat. Commun.* **2014**, *5*, 1.

[223] H. Nakanotani, K. Masui, J. Nishide, T. Shibata, C. Adachi, *Sci. Rep.* **2013**, *3*, 1.

[224] J. M. Kim, K. H. Lee, J. Y. Lee, *Adv. Opt. Mater.* **2022**, *10*, 1.

Chapter 2: Experimental methods

In this chapter I will outline the fabrication procedure of hole-only (HO)/electron-only (EO)/OLED devices as well as several measurement techniques. We will run through these in the order in which you would do when making a device.

2.1 Device cleaning

In a cleanroom environment, the pre-patterned ITO or glass substrates are cleaned using a soap solution and with a rubbing motion from the fingers. This is to get rid of the large dust particles as well as to mechanically smooth the ITO surface. Working in a cleanroom environment is important to limit the number of shorts in the final device. The soap cleaning is followed by a short rinsing under demi-water and subsequently, sonication in both acetone and isopropanol (IPA) for 10 minutes each.

2.2 Solution making / preparing for evaporation

Conjugated polymers can be readily dissolved in most organic solvents. For SY-PPV generally toluene is preferred. Generally, solutions are prepared one day before spin coating and left stirring. Before spin coating the solutions are filtered using a PTFE filter.

Before an evaporation the tooling factor must be set correctly so the thickness you set, will be the actual thickness of the evaporated layer. To do this one would set the evaporator to deposit (e.g.) 80 nm, measure the actual thickness (with a profilometer) and adjust the tooling according to

$$new\ tooling\ factor = old\ tooling\ factor * \frac{measured\ thickness}{set\ thickness} \tag{2.1}$$

2.3 Device fabrication

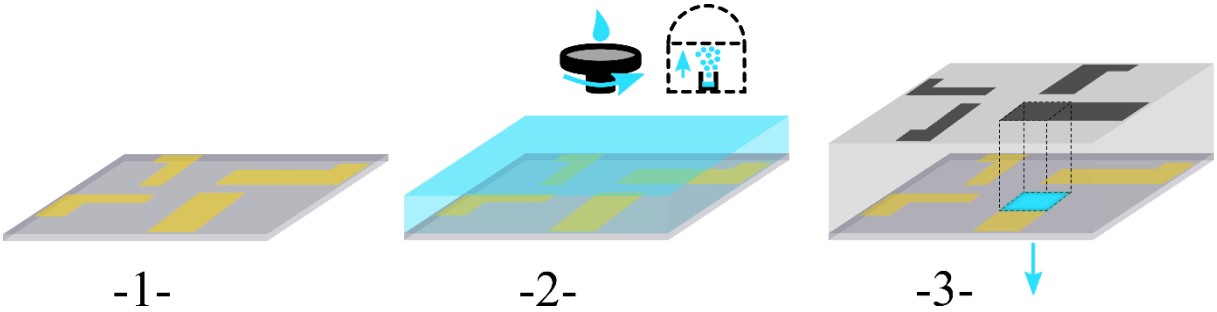

Figure 2.1: Schematic representation of the fabrication procedure of a standard bottom-emitting OLED. -1- represents the cleaned substrate with bottom electrodes; -2- the spin coating or evaporation of an organic layer and -3- the full device with counter-electrodes. In -3- the organic layer can be multiple layers, but for visibility it is depicted as one transparent grey layer. Furthermore in -3- the active area that lights up is depicted in blue and the direction where the light leaves the device is depicted with a blue arrow.

Hole only

HO devices use the patterned ITO substrates as bottom electrodes. These have a series resistance (Rs) which amounts to 30-40 Ohm. On top of the ITO a hole injection layer of poly(3,4ethylenedioxythiophene):polystyrene sulfonate (PEDOT:PSS) (±40 nm) (Heraeus

Clevios 4083) is spin-coated from an aqueous solution and annealed at 140 °C for 10 minutes. For symmetric TADF HO's (usually not for conjugated polymer HO's) MoO_3 (7 nm, rate of 0.12-0.15 Å s^{-1}) and C_{60} (4 nm, rate of 0.12 Å s^{-1}) are evaporated through a shadow mask. Next the active layer is spin coated or evaporated. For spin coating conjugated polymers it is generally advised to have the speed >1000 rpm in order to obtain a homogenous film. For evaporation one would like to keep the rate between 0.2 and 0.3 Å s^{-1} as a nice compromise between speed and uniformity. For TADF HO's (usually not for conjugated polymer HO's) again a layer of C_{60} (4 nm, rate of 0.12 Å s^{-1}) is evaporated. Next, a layer of MoO_3 (10 nm, rate of 0.12-0.15 Å s^{-1}) and a capping layer of 100 nm Aluminum (Al) (first slow then high rate) are evaporated. The organic layers do not require a shadow mask, however the Al does. Moreover, the mask for Al is set up in such a way that two contact points are formed and the device area is more to the center of the device. The substrate is always 3x3 cm^2 and the four active areas have a size of $8.1x10^{-6}$ m^2, $1.482x10^{-5}$ m^2, $3.481x10^{-5}$ m^2 or $9.7x10^{-5}$ m^2. All evaporations should be done in a glovebox environment, ideally with oxygen (O_2) and water (H_2O) values < 0.1 ppm, and under a pressure of around $1x10^{-6}$ mbar. The final device structures are:

Symmetric HO: ITO/PEDOT:PSS/MoO_3/C_{60}/active layer/C_{60}/MoO_3/Al

Asymmetric HO: ITO/PEDOT:PSS/active layer/C_{60}/MoO_3/Al

Where the red coloured compounds are generally only employed for TADF emitters. For conjugated polymers with deep HOMO levels (PFO for example), PEDOT:PSS can be swapped out for p-pTFF (±35 nm) if the C_{60} interlayer is not employed. Furthermore, ITO can be swapped for a 30 nm gold (Au) electrode in order to decrease the series resistance.

Electron only

EO devices are made on a glass substrate. First 30 nm Al is evaporated through a shadow mask and exposed to air for 5 minutes to form a small insulating layer of Al_2O_3 on top of the Al. Next the active layer is spin coated or evaporated. For TADF EO's (usually not for conjugated polymer EO's) what follows is the evaporation of a TPBi (4 nm, rate of 0.12 Å s^{-1}) layer. The EO is finished by evaporating barium (Ba) (5 nm, rate of 0.12 Å s^{-1}) and 100 nm Al. The active area is $1x10^{-6}$ m^2. The final device structure is:

Glass/Al/Al_2O_3/active layer/TPBi/Ba/Al

Where the red coloured compound is generally only employed for TADF emitters. The Ba can be left out if the WF of Al outlines well with the LUMO of the active layer *and* only if TPBi is employed as an interlayer.

OLED

The fabrication of OLEDs is outlined in figure 2.1. OLEDs are built on ITO substrates (fig. 2.1 -1-) and use the PEDOT:PSS HIL. What follows, as shown in figure 2.1 -2-, is the evaporation or spin coating of the active layer and potentially interlayers. For TADF OLEDs the standard layers are, in order, MoO_3, C_{60}, active layer and TPBi, all evaporated. The active layer, without any additional layers, is generally spin coated for conjugated polymers. Moving from -2- to -3- in figure 2.1 we evaporate the cathode, this includes evaporation of Ba and Al to finish the

device. Parameters for the various compounds such as rates and thicknesses are outlined under the EO and HO sections above. The final device structure is:

ITO/PEDOT:PSS/MoO_3/C_{60}/active layer/TPBi/Ba/Al

Where the red coloured compounds are usually only employed for TADF emitters.

2.4 *I-V* and EQE measurements

To expose the bottom ITO electrodes the organic layers are scratched off with a knife (harsh) or a cotton tip (softer, preferred). *I-V* measurements are carried out with a Keithley 2400 source meter, while simultaneously the photocurrent – voltage measurements are carried out with a Keithley 6514 system electrometer. A Labview software is used to set the parameters of the sweep, such as the maximum voltage and the voltage step size, as well as to read out the data. The EQE measurements are done using a calibrated silicon photodiode with an area larger than the emitting pixel. Current density and photocurrent density are calculated using an origin script. The EQE, luminance [cd m^{-2}], current efficiency [cd A^{-1}], luminous efficacy [lm W^{-1}] and Commission Internationale de l'éclairage (CIE) coordinates are calculated using a Python script. These measurements should be carried out in a glovebox environment with O_2 and H_2O values preferably below 0.1 ppm.

For the *J-V* measurement it is good not to scan to too high current densities as this may result in device failure. Furthermore, current densities too far beyond ~10^3 A m^{-2} are going to be limited by the series resistance of the ITO and are therefore not always reliable.

2.5 Degradation measurements

Degradation measurements are also carried out in a glovebox with O_2 and H_2O values below 0.1 ppm. The setup consists of 12 substrate holders coupled with a homebuilt voltage source. When the OLED is placed in the holder a photodiode is placed on top to collect the light. Labview software controls the voltage source as well as reads out the values of the voltage and photocurrent, generally every 30 seconds. There is a feedback loop between the computer and the voltage source, which updates also every 30 seconds, to ensure that the OLED is kept at a constant current.

2.6 Further characterization

EL measurements are taken with a USB4000 UV-Vis-ES spectrometer. Thickness measurements are done with a Bruker profilometer. PL and PLQY measurements are done with a HORIBA Jobin Yvon Fluorolog-3.

Chapter 3: Role of Singlet and Triplet Excitons on the Electrical Stability and Efficiency of Polymer Light-Emitting Diodes

Triplets are dark states in polymer light emitting diodes (PLEDs), thus despite their ubiquity their influence on the device operation is hard to probe. Therefore, to what extent triplets are involved in the efficiency or degradation of PLEDs is hard to quantify. Naturally singlets contribute to the efficiency, but here we also shed light on the positive role triplets play in the context of efficiency. We start in this chapter with undegraded PLEDs where we are able to quantitatively describe the external quantum efficiency (EQE) of a PLED, but only when we incorporate triplet-triplet annihilation (TTA) into our device model. Further down in this chapter the contribution of the two exciton types, singlets and triplets, on degradation is disentangled by systematically manipulating the exciton populations. To control singlet excitons, the emission of a blue-emitting PLED is modified to green by adding a small amount of a perylene-monoimide based green-emitting dye. The triplet population is manipulated by blending the light-emitting polymer with a dye that has either a longer or shorter triplet lifetime as compared to the polymer host. We prove the involvement of *triplet* excitons in PLED degradation. Our conclusion is twofold: we show the substantial enhancement that TTA can have on the efficiency, and our results reveal that the degradation in fluorescent PLEDs is governed by the interaction between polarons and triplet excitons.

3.1 Introduction

Studying PLEDs has clear advantages when it comes to mechanistic investigations, for example studying the mechanism of degradation. As pointed out in section 1.7 the standard PLED device structure is not multilayered, making degradation processes more straightforward to analyse. In earlier work on degradation of poly(phenylene vinylene) (PPV) based LEDs the effects of molecular weight, molecular structure and defects that arise during synthesis on lifetime have been discussed.[1] In particular halogen related defects in PPVs are pointed out to have a negative influence on the lifetime. With regard to physical degradation mechanisms, in 2001, Silvestre et al.[2] were the first to propose that 'voltage increase' and 'luminance decrease' during degradation shared a common origin, namely the formation of trap states. Furthermore, Pekkola et al.[3] studied the influence of triplet excitons on the electrical stability of conjugated polymers. A triplet sensitizer was introduced into a PPV-based LED, and a negative influence of triplet excitons on the lifetime was reported. As a possible mechanism the energy transfer from a PPV triplet to an oxygen triplet state, creating the reactive singlet oxygen molecule, was suggested.[4,5] Singlet oxygen has the ability to attack the vinyl bonds of PPV's, providing a chemical pathway for degrading the material.[6] Also in phosphorescent OLEDs (ph-OLEDs) the harmful influence of triplet excitons on lifetime has been extensively reported13-16.[7–10] The device lifetime of ph-OLEDs has been increased by the incorporation of a managing molecule that dissipates the energy of highly excited states, resulting from triplet-triplet or triplet-polaron interactions, before they can lead to bond dissociation.[11]

In recent years our understanding PLED degradation has advanced to a point that we can describe the dynamics of trap formation in SY PLEDs. Modelling of degraded PLEDs revealed that both the typical degradation characteristics of a voltage increase as well as a decrease of the light output during degradation could be linked to the formation of hole traps.[12] In the yellow emitting polymer super-yellow poly(*p*-phenylene vinylene (SY-PPV) the dynamics of the trap formation revealed that the interaction between excitons and polarons is responsible for the creation of these degradation traps.[13] In this picture an exciton will give its energy to a charge carrier and whereas the exciton goes to the ground state, the carrier gets promoted to a higher energetic state and has the ability to dissociate a chemical bond. The exciton-polaron annihilation correctly predicted the scaling of the trap density with J_{age} and aging time (t_{age}).[13] Just after starting the degradation experiment the number of trapped holes does not exceed the number of free holes, leading to a linear scaling of the trap density with $J_{age}^{3/2}$ and t_{age}. As the number of trapped holes becomes greater than the number of free holes, the scaling changes to a J_{age} scaling as well as a $t_{age}^{1/2}$ scaling. In contrast to the earlier oxygen- and halogen-related degradation, this mechanism is purely of an intrinsic nature.

Although for the first time PLED degradation has been quantitatively described, a major mechanistic question remains, namely whether singlet, triplet or both excitons are playing the major role in hole trap formation and the resulting PLED degradation. In this chapter we experimentally show, with the support of numerical modelling, that triplet excitons rather than singlet excitons are responsible for the intrinsic degradation of PLEDs. However, whereas there are negative sides to triplets, the situation is more nuanced than that, as triplets have been reported to boost the efficiency of undegraded PLEDs through the mechanism of triplet-triplet

annihilation (TTA). Due to the relatively low stability of phosphorescent blue OLEDs in present applications such as displays, blue-light is often generated by fluorescence. We have seen in section 1.6.5 that in fluorescent OLEDs the efficiency can be enhanced by up to 40% or even up to 62.5% by TTA. Although often studied, a comprehensive quantification of TTA using a validated device model is not present in literature. Here we resolve this issue by quantifying the positive effect triplets have on the efficiency of PLEDs.

Knowledge of the exact triplet dynamics and degradation mechanisms is indispensable for further improvement of the lifetime of organic LEDs. Due to their simplified device structure, PLEDs are an excellent model system to further study the fundamental processes involving triplet excitons, providing a basis for optimization of the lifetime and understanding of highly efficient TADF single-layer OLEDs and multi-layer ph-OLEDs.[14]

3.2 Experimental idea

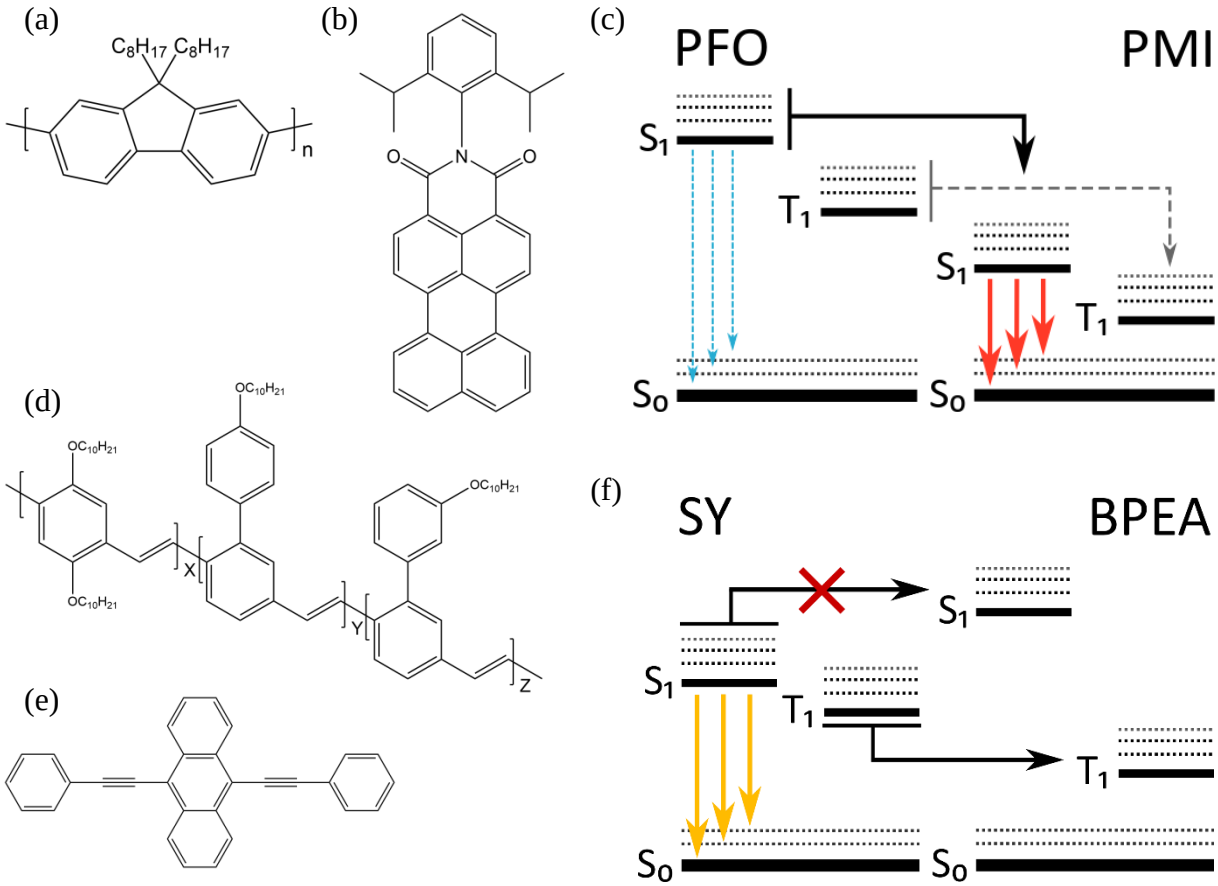

Figure 3.1: (a); (b); (d); (e) Structures of respectively PFO, DiPP-PMI, SY, BPEA. c) Schematic illustration of the PFO:PMI system. S_0, S_1 and T_1 are the singlet ground state, first singlet excited state and first triplet excited state respectively. The weakened fluorescence of

PFO and the weak triplet transfer are shown as dashed lines, whereas the prominent singlet transfer and stronger fluorescence of PMI are shown as bold lines. (f) Schematic illustration of the SY:BPEA system. Singlet transfer of SY to BPEA is energetically not favoured and therefore marked with a red cross.

In order to disentangle the effect of singlet and triplet excitons in PLEDs on degradation and efficiency, we have to manipulate their properties such as energy and lifetime. This can be achieved by blending the light-emitting polymer with suitable functional molecules.

Manipulation of the singlet energy is straightforward, as schematically shown in figure 3.1(c). The blue electroluminescence of PLEDs based on poly(dioctylfluorene) (PFO, figure 3.1(a)),[15–19] can be easily converted to green by blending PFO with a low concentration of green emitting dye, in our case the perylene-monoimide (PMI) derivative DiPP-PMI (figure 3.1(b)).[20] Perylene dyes have proven to be suitable candidates for tuning the emission colour of PFO over a wide spectral range.[21] Since the blue emission spectrum of PFO overlaps well with the absorption of DiPP-PMI the Förster resonance energy transfer (FRET) for singlet excitons is very efficient. As a result, a dye concentration of only 0.1% is sufficient to fully convert the blue PFO emission to green (figure 3.3). In case that singlet excitons play a role in PLED degradation lowering their energy would be beneficial for the device stability, since excited states resulting from exciton-polaron or exciton-exciton interactions would be lower in energy, reducing the probability of breaking chemical bonds. It should also be noted that the steady-state concentration of singlet excitons in a PLED under DC current stress is not significantly changed by the incorporation of the DiPP-PMI dyes, since the (singlet) exciton lifetime of both PFO and DiPP-PMI are in the nanosecond regime. One could argue that also triplet excitons generated on the PFO can be transferred towards the triple state of the DiPP-PMI. However, singlet transfer is known to take place over a larger distance than triplet transfer, since triplets are transferred via a Dexter mechanism. For β-phase PFO, a Förster radius of 8.2 nm has been reported,[22] while Dexter transfer only occurs over a distance of 1-2 nm. In one of the very first papers utilizing phosphorescence in OLEDs it was already shown that for 1% concentration of a phosphorescent dye in a host still electroluminescence (EL) of the host was visible,[23] showing that Dexter transfer from host to dye was not complete. Only at 6% dye concentration the host emission disappeared, and the emission solely originated from the phosphorescent dye. For this reason, almost all phosphorescent OLEDs utilize phosphorescent dye concentrations in the range of 6-10% in order to have complete Dexter energy transfer. At a dye concentration of only 0.1%, as used here, Dexter energy transfer is far from complete, as indicated by the dotted line in figure 3.1(c).The effect of the PMI dye incorporation is therefore mainly a reduction of the singlet exciton energy.

The effect of triplet excitons on degradation is harder to investigate in fluorescent OLEDs, because of their non-radiative nature. For this purpose, we blend super-yellow poly(p-phenylene vinylene) (SY-PPV,[24] figure 3.1(d)) with the anthracene derivative 9,10-Bis(phenylethynyl)anthracene (BPEA,[25] figure 3.1e). As schematically shown in figure 3.1(f), we make use of the fact that the anthracene derivative has a higher singlet-triplet splitting than the SY-PPV. On the one hand, as a result of the higher lying T_1 level of SY (1.3 eV)[26] with respect to that of BPEA (1.11 eV),[27] triplets can be efficiently transferred from the SY-PPV to

the BPEA . On the other hand, since the singlet level of SY-PPV (2.21 eV)[26] lies below that of the BPEA (2.4 eV)[27] there will not be any Förster transfer of singlet excitons from SY-PPV to BPEA. Another substantial advantage of this system is that due to the higher bandgap of BPEA as compared to SY-PPV, the BPEA molecules will not act as charge traps. Therefore, BPEA can be added in concentrations of 5-10%, sufficient to capture all triplet excitons from SY-PPV, without disrupting the charge transport.[28] Furthermore, since the HOMO and LUMO levels of the BPEA dye are coinciding with those of the SY-PPV host, the charge transport and recombination will be dominated by the host, even at 15% BPEA concentration. Dye concentration dependent processes as guest-guest transport, which is often used in conventional OLEDs to balance transport, do not play a role in these SY-PPV:BPEA blends. Collecting all triplet excitons on the anthracene derivative has large consequences for the steady-state amount of triplet excitons during current stress. Triplet lifetimes of SY-PPV are on the order of 100 µs,[29] whereas BPEA molecules have reported triplet lifetimes of 2.7-2.8 ms.[25] A more than ten times enhancement of the triplet lifetime will then lead to a corresponding increase of the steady-state triplet population under electrical stress. Since the singlet exciton properties are not affected, addition of BPEA allows us to independently manipulate the triplet concentration, which will affect triplet-polaron and triplet-triplet interactions.

In addition to studying degradation, manipulating the triplet population with BPEA opens a pathway for us to study the role triplets play in the efficiency of undegraded PLEDs. A high triplet concentration on BPEA might in theory lead to TTA upconversion from the triplet T_1 to the singlet S_1 state of BPEA, after which a transfer to the S_1 state of SY can take place. If this recombination mechanism would be important a significant enhancement of the PLED efficiency upon addition of BPEA would be expected. This recombination pathway is expected to be unimportant however, since the efficiency of the upconversion reaction via TTA was reported to be only 1.6% for BPEA.[30] Another pathway for triplets is back transfer of triplets from BPEA to the SY, but this is energetically unfavorable and will thus also be unimportant. Furthermore, the low wt% of BPEA means once triplets are on the BPEA, they are further away from other triplets, and their ability to diffuse to other BPEA molecules is restricted. Effectively, by capturing triplets on the BPEA molecules we are inhibiting the TTA pathway on the SY. This gives us the opportunity to study and quantify the TTA effect, if it plays a role in the first place.

3.3 The effect of TTA on the efficiency of PLEDs

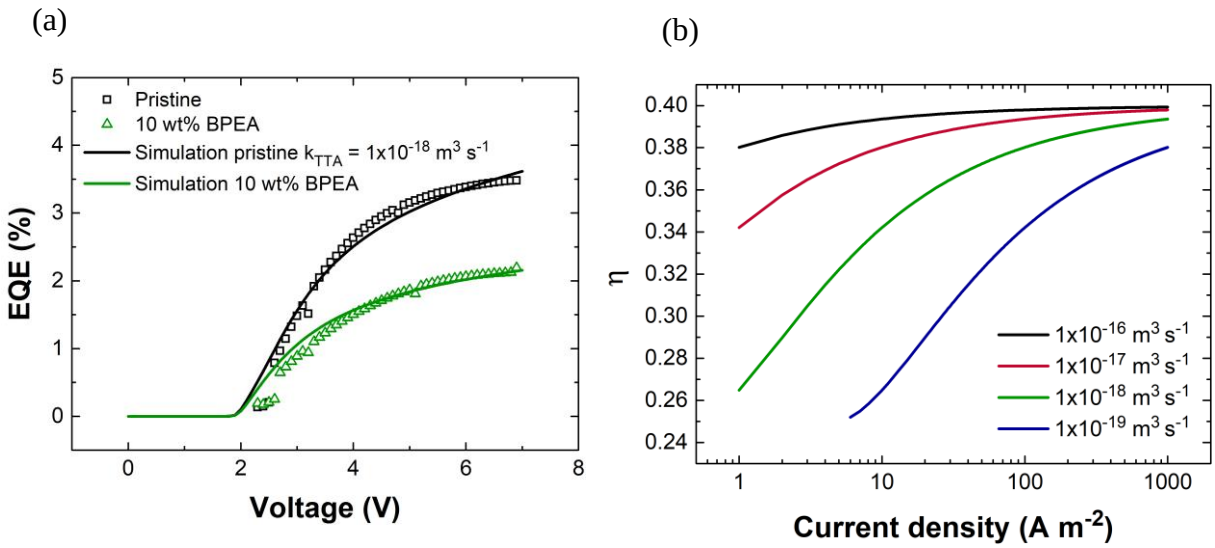

Figure 3.2: (a) EQE versus voltage for a SY and SY:BPEA OLED. (b) Efficiency of singlet generation as function applied current density for varying k_{TTA}.

We observe a decreasing EQE of 3.5% to 2.2% upon the addition of BPEA to our SY LEDs, as shown in figure 3.2(a). Looking at formula (1.26) for the EQE (section 1.6.5) we see there are four factors that could in principle be affected by the addition of BPEA. We know that BPEA does not act as an electrical trap for SY, thus the charge balance factor is not affected. Similarly, the low wt% of BPEA is not expected to influence the PLQY or the outcoupling either. What is left is the singlet/triplet fraction. Since TTA is known to influence the efficiency of PLEDs, let us find out what the exact magnitude of this effect is on the efficiency. For this we turn to rate equations, combining equations (1.33a-d) (section 1.6.7) in order to provide a description of the light output with TTA. The full derivation for the singlet and triplet population is given in appendix A (section A.1), but the final expressions are also given here:

$$\frac{[S(x,t)]}{\tau_s} = \frac{1}{4}\cdot G(x,t) + \frac{1}{4}\cdot k_{TTA}\cdot [T(x,t)]^2. \tag{3.1}$$

$$[T(x)] = \frac{-2\cdot\tau_t^{-1}}{5\cdot k_{TTA}} + \sqrt{4\cdot\left(\frac{\tau_t^{-1}}{5\cdot k_{TTA}}\right)^2 + 4\cdot\frac{0.75\cdot G(x)}{5\cdot k_{TTA}}}. \tag{3.2}$$

With τ_t the triplet lifetime. The maximum efficiency of the TTA process is given when no triplets decay via phosphorescence. Mathematically this is implemented in equation (3.2) as $\tau_t \to \infty$, which simplifies the triplet density to:

$$[T(x)] = \sqrt{4\cdot\frac{0.75\cdot G(x)}{5\cdot k_{TTA}}}. \tag{3.3}$$

Plugging eq. (3.3) into (3.1) and calculating the efficiency (Appendix A, A.1) we see that:

$$\eta_{max} = 0.25 + 0.15 = 0.4. \tag{3.4}$$

Where the first term is coming from the electrically generated singlet population and the second term originates from the singlets of TTA.

As predicted before in section 1.6.5, we see again an increase from 25% to 40% in internal efficiency in case TTA enhances the efficiency, and this factor of 1.6 is exactly what we see as difference in efficiency between the OLED with and without BPEA (figure 3.2(a)). The effect of adding BPEA is thus not to provide an up-conversion channel, instead we suggest it prevents triplets on the SY to generate singlets through TTA.

We can get an estimate of the k_{TTA} constant in SY through this experiment. Naturally the triplet population varies with the applied voltage, at higher voltages there is a higher triplet concentration which concomitantly increases the singlet generation from TTA as well. However two other factors are playing a role in how the efficiency is going to vary with voltage, these are the k_{TTA} constant and τ_t. For a fixed τ_t of 100 µs figure 3.2(b) shows how the generation of singlets varies with k_{TTA}. For values of $k_{TTA} > 1x10^{-18}$ m^{-3} s^{-1} we observe no major difference in efficiency increase at higher currents, whereas lower values of k_{TTA} give a clear drop in internal efficiency. We can now combine the optical rate equations and electrical model, outlined in section 1.6.6, to describe the efficiency. Modelling the efficiency of BPEA with standard SY mobility parameters,[12] trap parameters and incorporating TTA with a $k_{TTA} = 1x10^{-18}$ m^{-3} s^{-1} through rate equations leads to the black curve in figure 3.2(a). The value of k_{TTA} found here is about an order of magnitude lower than found for the blue emitting F8BT.[31] Turning TTA off correctly predicts the green EQE curve with 10 wt% BPEA, proving that TTA is indeed playing a substantial role in the efficiency of PLEDs.

Regarding stability of PLEDs TTA can also play an important role. First, a higher efficiency due to TTA means for a given light-output a lower current, so less polarons, which reduces triplet-polaron interactions. Furthermore, TTA also lowers the triplet lifetime, resulting in a lower steady-state triplet concentration in an OLED driven at constant current, which will enhance the stability as well.[7] Specifically for blue-emitting devices recent progress in both efficiency and stability has been achieved by employing TTA.[32,33]

3.4 PLED degradation with reduced singlet energy

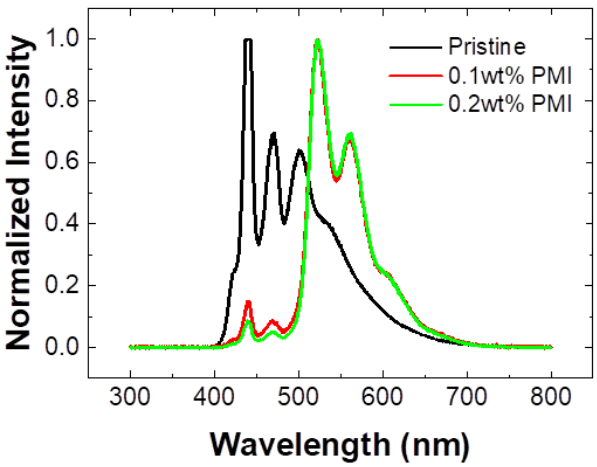

Figure 3.3: EL spectrum of PFO:PMI in various weight percentages.

Previous reports on the degradation of PLEDs using PFO and its derivatives as emitter apply poly(3,4-ethylenedioxythiophene) polystyrene sulfonate (PEDOT:PSS) as anode,[34,35] despite the misalignment in HOMO levels of PEDOT:PSS (-5.0 eV) and PFO (-5.8 eV). From earlier studies it is known that the initially limited hole injection from PEDOT:PSS into PFO is strongly enhanced once injected electrons from the cathode side reach the PEDOT:PSS and get trapped at the PFO/PEDOT:PSS interface.[36] This 'forming' of the hole injection contact shows up as strong hysteresis in the first current-voltage (*J-V*) scan. During subsequent *J-V* scans the enhanced hole injection remains. The presence of this forming process complicates the degradation analysis of PEDOT:PSS/PFO based PLEDs, since during prolonged electrical driving it is unclear what happens to the PEDOT:PSS/PFO interface and the resulting hole injection. For this purpose, for devices using PFO and PFO:PMI blend as emitting layers, we replace PEDOT:PSS by p-doped poly(9,9-bis(3-(pentafluoroethanesulfonyl-imidosulfonyl)propyl)fluorene-2,7-diyl-*alt*-1,4-phenylene-(*p*-trifluoromethylphenylimino)-1,4-phenylene) (p-pTFF).[37] Since p-pTFF with a work function of ~5.85 eV does not require a forming process to obtain efficient hole injection into PFO,[37]vv this allows us to more reliably analyse our degradation results.

As first step, to show that the energy transfer from PFO to DiPP-PMI takes place, the EL spectra of pristine PFO and PFO doped with 0.1-0.2% weight-percentages of DiPP-PMI are presented in figure 3.3. While the PFO emission peaks are still present in a minimal way, the by far dominant contribution to the EL spectrum stems from the PMI.

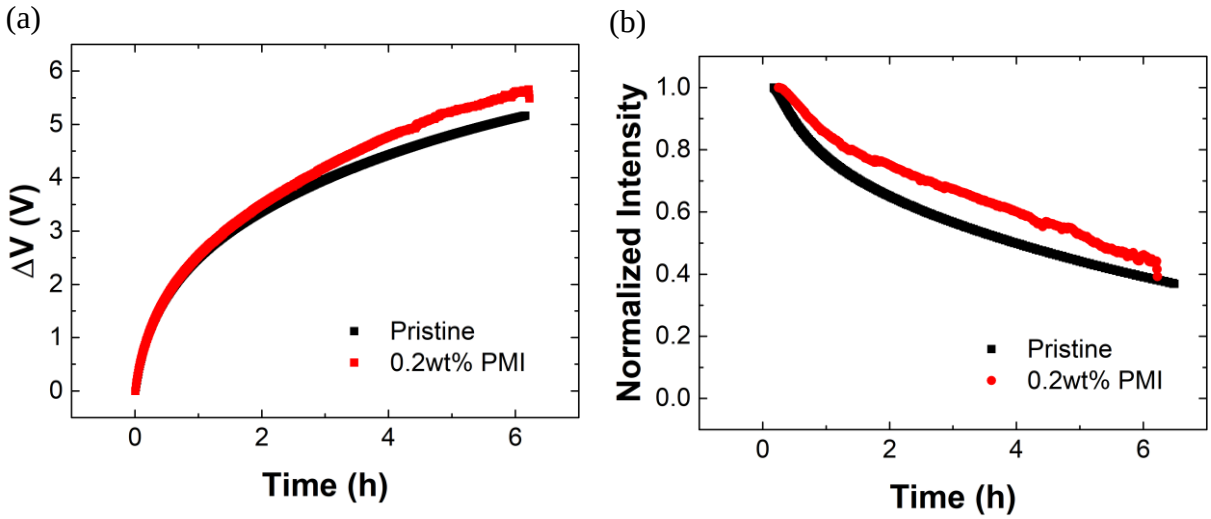

Figure 3.4: Degradation characteristics of pristine PFO and PFO with 0.2 wt% DiPP-PMI under constant current stress with (a) Increase of the driving voltage and (b) normalized light output as a function of stress time. The PLEDs were aged at a current density of 10 mA cm^{-2}.

Furthermore, the *J-V* and normalized light-output vs voltage (*L-V*) characteristics of PFO and PFO:DiPP-PMI (0.2 wt%) PLEDs show that incorporation of such a small amount of dye does not strongly affect the charge transport and light generation in the respective PLEDs.[28] This is expected since due to severe electron trapping the current in a pristine PFO based PLED is carried by holes.[38] The DiPP-PMI dye thus mostly affects the electron transport of the PFO.[28]

Figure 3.4 shows the degradation characteristics of the PFO:DiPP-PMI devices aged at a constant current density of 10 mA cm^{-2}. Over the electrical driving period of around 6 hours,

the samples with and without DiPP-PMI show nearly the same voltage increase (figure 3.4(a)) of around 5V as well as an identical decrease of the light-output (figure 3(b)). By changing the emission colour from blue to green we have altered the energy of the singlet excitons by 0.44 eV. The absence of any stability difference suggests that the energy of singlet excitons has no significant influence on the degradation characteristics of PLEDs.

To verify that we do not influence the analysis of the degradation characteristics of the PFO PLED by addition of a molecule with an electron trapping character, we have performed numerical simulations. The numerical PLED device model[13] is based on drift-diffusion equations that take the voltage, *V(t)*, from the degradation experiment as input, and calculate the hole trap density (P_t) needed to keep the current constant at the aging current at each point in time. The light output as a function of stress time can then numerically be calculated by considering the radiative Langevin recombination together with the non-radiative trap-assisted recombination, that arises from the already existing electron traps and the newly formed hole traps. First, we calculate the amount of hole traps as function of time formed during current stress for a PLED with the typical parameters for PFO.[38] To incorporate the effect of the additional DiPP-PMI molecules, we then increase the amount of electron traps by a factor of two and perform the same analysis. The effect on the derived hole trap density as function of stress time is only marginal,[28] showing that the electron trapping feature of the PMI does not affect the degradation analysis.

3.5 PLED degradation with enhanced triplet lifetime

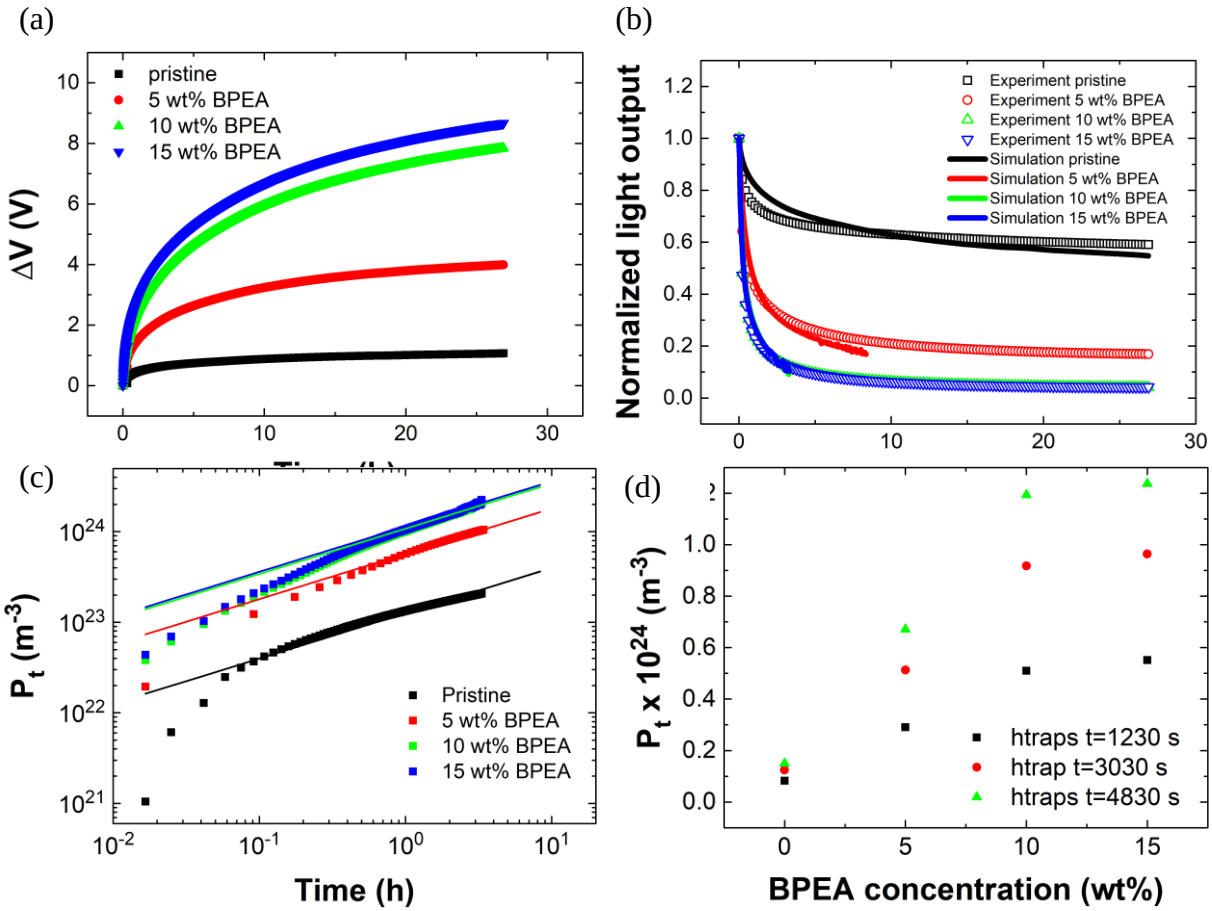

Figure 3.5: Degradation characteristics of SY PLEDs with different weight-percentages of BPEA. (a) Increase of driving voltage and (b) normalized light output as a function of stress time for 0-15 wt% BPEA mixed into the SY-PPV active layer. (c) Hole trap density as a function of time obtained from numerical simulation. The solid and lines have slope 0.5 and are a guide to the eye. (d) Hole trap density at various stress times plotted as a function of BPEA concentration.

Next, we perform degradation experiments with SY:BPEA PLEDs to study the effect of an enhanced triplet lifetime, resulting in an enhanced triplet steady-state concentration. To capture most of the triplet excitons generated in SY-PPV during PLED operation we vary the BPEA concentration from 5 to 15 weight-percent. The EL spectra of SY blended in different weight-percentages with BPEA show no variation of the singlet peak of SY (λ = 550 nm), confirming the absence of singlet transfer from SY to BPEA molecules.[28] The reported HOMO level of BPEA (-5.49 eV) is slightly deeper than the HOMO of SY (~-5.4 eV) and the LUMO of BPEA (-2.92 eV) is marginally shallower to the LUMO of SY (~-2.8 eV).[39] Significant charge trapping is therefore not expected, also not for high BPEA concentrations. This is confirmed by the *J-V* and *L-V* of the SY:BPEA LEDs.[28] From the *J-V* curves we see that increasing the BPEA concertation from 5 to 15 weight-percent indeed has no effect on the charge transport and light-output of the PLED.

The degradation characteristics of the SY:BPEA PLEDs are presented in figure 3.5 and were studied under a constant current density of 10 mA cm^{-2}. Figures 3.5(a) & (b) show that the voltage increase and luminance decrease over time become significantly stronger with an increasing weight-percentage of BPEA, until 10wt%, at which point they saturate. The time when the light intensity reaches 80% of its initial intensity, LT80, decreases roughly by a factor of 8, 15 and 18 when adding 5, 10 and 15 wt% BPEA respectively. Using numerical simulations we extract the hole trap density (P_t) as a function of time, which is plotted in figure 3.5(c). The simulations were based on the description as outlined above. The resulting light-output from the simulation can be compared with the luminance decrease over time from the degradation experiment, which are plotted together in figure 3.5(b) and show good agreement.

After adding more than 10 wt% of BPEA, we can see from figures 3.5(a) & (b) that the degradation characteristics do not change anymore. This is also reflected in the P_t vs t plot as well as in the plot of *P_t vs BPEA concentration* at a specific point in time (figures 3.5(c) & (d)). Phosphorescent OLEDs typically employ an emitter concentration of around 6-10 wt% in order to harvest all triplets that are created on the host. It is therefore unsurprising that 10 wt% of BPEA is sufficient to collect all triplets in the SY-PPV PLED, which accounts for the saturation of the degradation characteristics for BPEA concentrations higher than 10 wt%. We note that by addition of BPEA we also slightly lower the energy of the triplet excitons. It is well known that the triplet energy plays an important role in the stability of phosphoresecent OLEDs, red emissive OLEDs are more stable than blue due to a ~ 1 eV lower triplet energy. However, in our SY-PPV:BPEA blends the lowering of the triplet energy is relatively small (<0.2 eV). Furthermore, we inhibit TTA to take place on the SY, increasing the triplet density. Our experiments show that the effect of this slightly lowered triplet energy, which would be

beneficial for stability, is overruled by the longer triplet lifetime and inhibition of TTA, which strongly decreases stability, as experimentally observed.

3.6 Increase of PLED stability

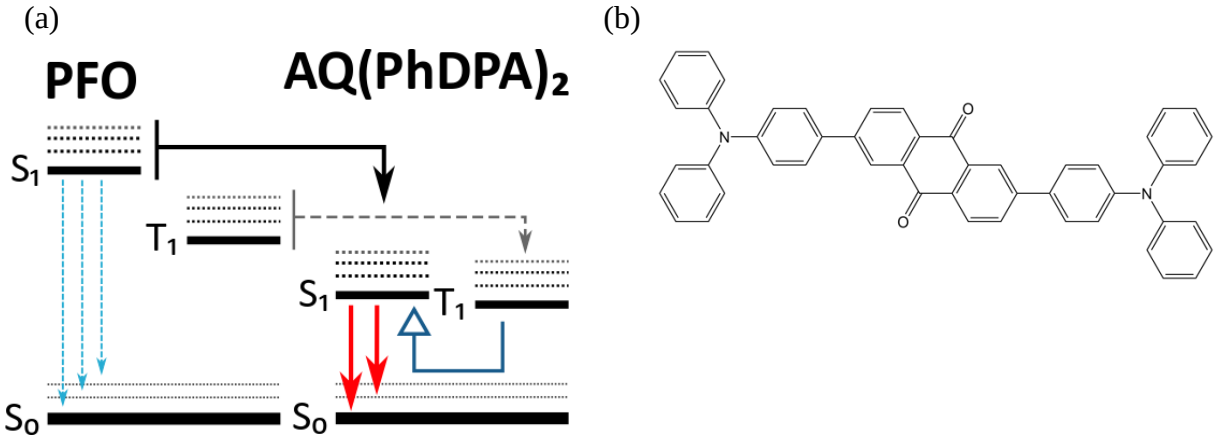

Figure 3.6: (a) Schematic energy level diagram for the PFO:AQ(PhDPA)$_2$ blend. The weak emission of PFO and the reduced triplet transfer from PFO to the TADF molecule are shown as dashed lines, whereas the stronger fluorescence of the TADF dye and the singlet transfer of PFO to the TADF molecule are shown as bold lines. The reverse intersystem crossing is shown as a blue arrow with an open arrowhead. (b) Chemical structure of AQ(PhDPA)$_2$.

Summarizing, we observe that lowering of the energy of singlet excitons does not influence PLED degradation, whereas enhancement of the triplet lifetime strongly accelerates the degradation process. This indicates that triplet excitons play an important role in the PLED degradation. A next question is then if the PLED stability can also be enhanced by a reduction of the triplet lifetime.

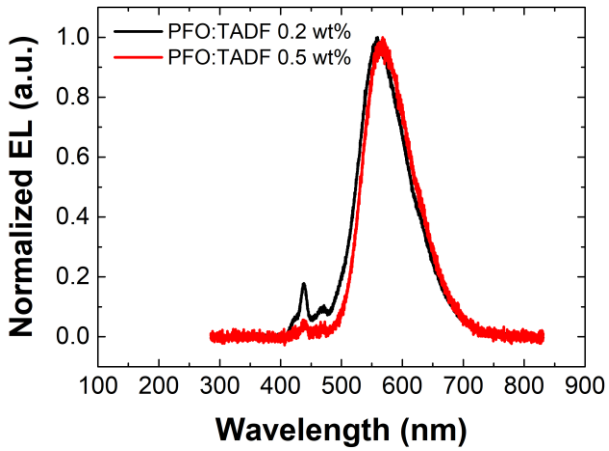

Figure 3.7: EL spectrum of PFO:AQ(PhDPA)$_2$.

In order to reduce the triplet lifetime in a blue-emitting PFO based PLED we blend PFO with the red emitting molecule 2,6-bis[4-(diphenylamino)phenyl]-9,10-Anthracenedione AQ(PhDPA)$_2$ (chemical structure in figure 3.6(b)).[40,41] AQ(PhDPA)$_2$ shows next to prompt

fluorescence also TADF as a result of reverse intersystem crossing due to the reduced energy splitting between the singlet and triplet levels. In this way the population of its triplets is depleted via the singlet state and their lifetime is shortened, leading to a reduction of the steady-state triplet population in the PLED under stress. The PFO:AQ(PhDPA)$_2$ blend, shown in figure 3.5(a), is from an energy level perspective similar to the PFO:PMI blend (figure 3.1(c)). Equal to the PFO:PMI blend transfer of singlet excitons from PFO to AQ(PhDPA)$_2$ will be efficient due to the long range Förster process.

As a result, shown in figure 3.7, only a low concentration of a few tenths of weight-percent of dyes is required to shift the emission colour from blue to red. To harvest all triplets on the dye a higher concentration would be required. We note that here increasing the concentration of the TADF dye to harvest more triplets is not straightforward. From the position of the HOMO and LUMO levels we expect the TADF dye to function as a deep electron trap, since the LUMO of AQ(PhDPA)$_2$ (-3.6 eV) is much deeper than the LUMO of PFO (-2.6 eV). In contrast, their HOMO levels (-5.8 eV for PFO and -5.9 eV for AQ(PhDPA)$_2$) are well aligned,[41] so addition of the TADF dye will not impede hole transport. The *J-V* curves show that, as expected, the increased electron trapping due to the red TADF has only a minor effect on the hole dominated current in the PFO LED.[28] However, addition of a large amount (5-10 wt%) of deep electron traps will confine the electroluminescence in a very narrow region close to the cathode, where most of the excitons will be quenched by the metallic electrode. This will obscure the degradation processes. For this reason, we have focused on PLEDs with 0.5 wt% of AQ(PhDPA)$_2$, where next to the *J-V* also the *L-V* characteristics are not strongly affected yet by incorporation of the dyes. A disadvantage is then that we will collect only a fraction of the in PFO generated triplets on the dye (figure 3.6(a), grey dashed line), but on the other hand still partially reduce the triplet population in the PLED.

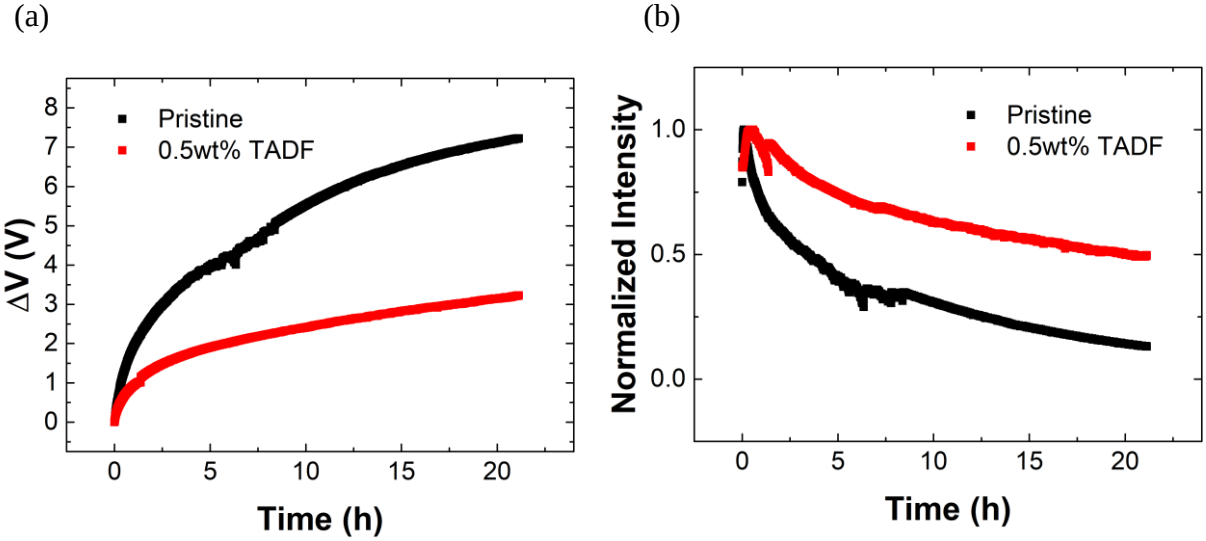

Figure 3.8: (a) Voltage increase and (b) normalized light output versus time of the PFO:AQ(PhDPA)$_2$ LEDs for different wt% of TADF aged at a constant current density of 10 mA cm^{-2}.

To investigate the influence of the TADF dye on the PLED driving voltage and light output during degradation, we again perform the degradation tests at a constant current density of 10 mA cm^{-2}. The degradation characteristics of the PFO:AQ(PhDPA)$_2$ LEDs are presented in

figure 3.8. We observe that the voltage increase is reduced with increasing amount of TADF dye in the active layer, and the light is more stable, demonstrating that a reduced triplet lifetime enhances stability.

3.7 Qualitative reasoning why triplets decrease stability

Typically, in a fluorescent PLED 25% of the excitons formed by Langevin recombination exhibit the singlet spin state, whereas 75% are formed with the triplet spin state. Recombination of singlet excitons is fast: time-resolved photoluminescence measurement revealed a singlet exciton lifetime τ_S of 1.9 ns for SY-PPV at room temperature.[42] In contrast, the transition of the triplet state to the ground state is spin-forbidden and therefore a slow process compared to the singlet fluorescence. As mentioned before, the triplet exciton lifetime τ_T in PPV derivatives was previously reported to be around 100 µs.[29] This substantial difference in exciton lifetime strongly affects the steady-state concentration of singlet *[S]* and triplet *[T]* excitons in a PLED under operation. As a consequence, the steady-state amount of triplet excitons in an operating PLED can be 4-5 orders of magnitude larger than the amount of singlet excitons. Furthermore, in an unaged operating PLED, the density of free electrons is much smaller than the density of free holes due to the present of electron traps[48]. Therefore, the interactions between triplet excitons (triplet-triplet annihilation) and between triplet excitons and free holes (triplet-polaron interaction) are expected to be dominant processes in an operating PLED.

3.8 Verifying triplet-polaron quenching as the degradation mechanism

Having now the experimental confirmation that indeed triplet excitons are involved in the degradation of fluorescent PLEDs, but also having pinpointed the role of triplets in the efficiency, a point we should address is if the mechanism of hole trap formation during degradation really proceeds via the triplet-polaron interaction[13] or if TTA plays a role in degradation as well. Another mechanism involving triplets that possibly plays a role is monomolecular triplet recombination. Recently it was found that degraded OLED products are also formed under UV radiation only, from which the authors conclude that TTA is likely to contribute to degradation.[43] The question remains how the contributions of the various triplet-related degradation mechanisms can be disentangled in the first place.

Experimentally, it was found that the hole trap formation scales linearly with the current density (J) and scales with stress time (t) as $t^{1/2}$ presented in equation 3.5:

$$P_t = \alpha \times J \times t^{1/2}. \tag{3.5}$$

with α a proportionality constant. This trap formation rate could be rationalized by Niu et al. as being the result of (triplet) exciton-polaron interactions.[13]

Following the same approach the dynamics of hole trap formation for the case of a monomolecular process (presented in Appendix B) can also be derived, given by:

$$P_t = \gamma \times J^{3/4} \times t^{1/2}. \tag{3.6}$$

with γ another proportionality constant. Furthermore, for the case of triplet-triplet interaction, we obtain an expression for the hole trap density formation (Appendix B) following:

$$P_t = \beta \times J \times t^{1/3}. \tag{3.7}$$

with β again a proportionality constant. This demonstrates that we can distinguish between these three mechanisms by analysing the aging current and time dependence of the hole trap density. For SY-PPV it has already been reported that the hole trap density shows a linear dependence on aging current, combined with a square-root dependence on stress time[13]. Combination of these observations then exclude triplet-triplet interactions and monomolecular decay processes as cause of the hole trap formation during stress. Another argument can be made based on the scaling of the hole trap density with BPEA concentration. Figure 3.5(d) shows that the amount of generated hole traps scales linearly with the concentration of BPEA for the time points considered. Intuitively, a quadratic dependence is expected if TTA would be the most pronounced mechanism behind degradation. A linear concentration dependence instead argues in favour of the triplet-polaron interaction. Furthermore, the observed linear dependence of hole trap formation on BPEA concentration also indicates that the BPEA triplet lifetime remains unaffected. A strong decrease of the triplet lifetime with increasing BPEA concentration would result in a sublinear behavior.

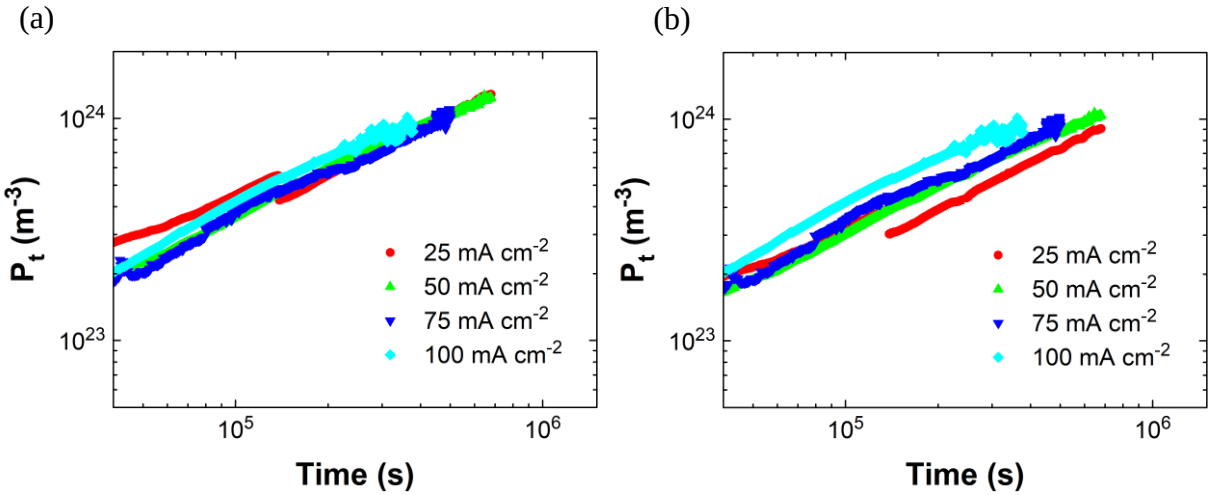

Figure 3.9: Hole trap density as a function of time for different aging currents, a) scaled linearly with the aging current (~J), b) scaled with a ¾-power of the aging current (~$J^{3/4}$).

Another question is whether the observed dependence of hole trap formation on stress time and stress current also holds for other PPV derivatives. For this purpose, we used the polymer poly[2-methoxy-5-(2′ -ethyl-hexyloxy)-1,4-phenylenevinylene] (MEH-PPV) as the emitting material. MEH-PPV has a higher mobility of $5x10^{-11}$ m^2 V^{-1} s^{-1} as compared to SY-PPV,[44] which amounts to $5x10^{-12}$ m^2 V^{-1} s^{-1}.[12] Figure 3.9 shows the hole trap density over time for a range of aging currents scaled with either a linear J (figure 3.9(a)) or a $J^{3/4}$ (figure 3.9(b)) current dependence. We vary the aging currents from 25 mA cm^{-2} to 100 mA cm^{-2} and show the

modelled hole trap densities after the initial 'burn-in'[13]. The scaling is done as follows: P_t at an aging current of 100 mA cm^{-2} is taken as a reference, and the hole trap densities in the range of 25 to 75 mA cm^{-2} are multiplied by a factor $100/J_{age}^{x}$, where J_{age} is the aging current in mA cm^{-2}, and 'x' is either 1 or ¾ for a J- or a $J^{3/4}$-scaling respectively. In other words, the hole trap densities in the range of 25 to 75 mA cm^{-2} are corrected as if they had an aging current of 100 mA cm^{-2}. It appears that the hole trap concentration curves scaled linearly with the aging current lie almost on top of each other, while the $J^{3/4}$-scaled curves are further apart. Based on these results we can already exclude the monomolecular process. To differentiate between the triplet-polaron or triplet-triplet interaction, we look at the time dependence of the hole trap density. The slope of the *Pt vs stress time* in figure 3.9 (as in figure 3.5(c)) is close to 0.5, in agreement with the earlier results on SY-PPV. As a result, also in MEH-PPV the current and stress time dependence of the hole trap formation point to triplet exciton – polaron interactions as dominant degradation mechanism.

3.9 Conclusions

In conclusion, we have quantified the involvement of TTA in the efficiency of PLEDs. Furthermore, we have experimentally disentangled the effect of singlet and triplet excitons on PLED degradation. Our results show that triplet excitons are responsible for the degradation of PLEDs, via their interactions with polarons. Lowering the singlet energy by incorporating a low concentration of fluorescent dyes does not affect PLED degradation. In contrast, addition of anthracene derivatives with long triplet lifetimes, without affecting the singlet excitons in the host, strongly enhances degradation. Incorporation of a dye with TADF functionality with reduced triplet lifetime successfully enhances the PLED lifetime. The current and time dependence of hole trap formation under current stress provide a fingerprint for the mechanism of the degradation. The observations point to triplet exciton -polaron interactions as being the main mechanism behind the trap formation. The relatively simple PLED device structure allows for a quantitative basic understanding of the degradation and efficiency, which will form a base for unravelling the degradation and device physics in more complex device architectures and more efficient Ph- and TADF-based OLEDs.

3.10 Experimental section

p-pTFF HIL fabrication

All devices were made as outlined in section **2.3**. P-pTFF was spin-coated from acetonitrile (ACN) solution after dissolving by help of an oil bath at 80°C and mechanical shaker treatment. On top of the hole-injection layer, the active layer was spin-coated in a N_2-rich environment from a chlorobenzene solution. The spin-coating parameters were set such that the thickness of the active layer ranged between 100 and 200 nm.

References

[1] A. Gassmann, S. V Yampolskii, A. Klein, K. Albe, N. Vilbrandt, O. Pekkola, Y. A. Genenko, M. Rehahn, H. Von Seggern, *Mater. Sci. Eng. B Solid-State Mater. Adv. Technol.* **2015**, *192*, 26.

[2] G. C. M. Silvestre, M. T. Johnson, A. Giraldo, J. M. Shannon, *Appl. Phys. Lett.* **2001**, *78*, 1619.

[3] O. Pekkola, A. Gassmann, F. Etzold, F. Laquai, H. Von Seggern, *Phys. Status Solidi Appl. Mater. Sci.* **2014**, *211*, 2035.

[4] J. R. Durrant, Y. W. Soon, H. Bronstein, H. Cho, I. McCulloch, J. Low, H. Bronstein, I. McCulloch, J. R. Durrant, *Chem. Commun.* **2013**, *49*, 1291.

[5] B. H. Cumpston, K. F. Jensen, *Synth. Met.* **1995**, *73*, 195.

[6] R. D. Scurlock, B. Wang, P. R. Ogilby, J. R. Sheats, R. L. Clough, *J. Am. Chem. Soc.* **1995**, *117*, 10194.

[7] Y. Zhang, J. Lee, S. R. Forrest, *Nat. Commun.* **2014**, *5*, 1.

[8] D. G. Ha, J. Tiepelt, M. A. Fusella, M. S. Weaver, J. J. Brown, M. Einzinger, M. C. Sherrott, T. Voorhis, N. J. Thompson, M. A. Baldo, T. Van Voorhis, N. J. Thompson, M. A. Baldo, T. Voorhis, N. J. Thompson, M. A. Baldo, *Adv. Opt. Mater.* **2019**, *1901048*, 1901048.

[9] N. C. Giebink, B. W. D'Andrade, M. S. Weaver, P. B. MacKenzie, J. J. Brown, M. E. Thompson, S. R. Forrest, *J. Appl. Phys.* **2008**, *103*.

[10] S. R. Forrest, *Philos. Trans. A* **2015**, *373*.

[11] J. Lee, C. Jeong, T. Batagoda, C. Coburn, M. E. Thompson, S. R. Forrest, *Nat. Commun.* **2017**, *8*, 1.

[12] Q. Niu, G. J. A. H. Wetzelaer, P. W. M. Blom, N. I. Crăciun, *Adv. Electron. Mater.* **2016**, *2*, 1.

[13] Q. Niu, R. Rohloff, G. A. H. Wetzelaer, P. W. M. Blom, N. I. Crăciun, *Nat. Mater.* **2018**, *17*, 557.

[14] N. B. Kotadiya, P. W. M. Blom, G.-J. A. H. Wetzelaer, *Nat. Photonics* **2019**, 1.

[15] M. Ariu, M. Sims, M. D. Rahn, J. Hill, A. M. Fox, D. G. Lidzey, M. Oda, J. Cabanillas-Gonzalez, D. D. C. Bradley, *Phys. Rev. B - Condens. Matter Mater. Phys.* **2003**, *67*, 1.

[16] X. Zhang, Q. Hu, J. Lin, Z. Lei, X. Guo, L. Xie, W. Lai, W. Huang, *Appl. Phys. Lett.* **2013**, *103*.

[17] A. Perevedentsev, S. Aksel, K. Feldman, P. Smith, P. N. Stavrinou, D. D. C. Bradley, *J. Polym. Sci. Part B Polym. Phys.* **2015**, *53*, 22.

[18] N. Dieter, *Macromol. Rapid Commun.* **2001**, *22*, 1365.

[19] T. Virgili, G. Cerullo, L. Lüer, G. Lanzani, C. Gadermaier, D. D. C. Bradley, *Phys. Rev. Lett.* **2003**, *90*, 4.

[20] T. Weil, T. Vosch, J. Hofkens, K. Peneva, K. Müllen, *Angew. Chemie - Int. Ed.* **2010**, *49*, 9068.

[21] C. Ego, D. Marsitzky, S. Becker, J. Zhang, A. C. Grimsdale, K. Müllen, J. D. MacKenzie, C. Silva, R. H. Friend, *J. Am. Chem. Soc.* **2003**, *125*, 437.

[22] A. L. T. Khan, P. Sreearunothai, L. M. Herz, M. J. Banach, A. Köhler, *Phys. Rev. B - Condens. Matter Mater. Phys.* **2004**, *69*, 1.

[23] M. A. Baldo, D. F. O'Brien, Y. You, A. Shoustikov, S. Sibley, M. E. Thompson, S. R. Forrest, *Nature* **1998**, *395*, 151.

[24] H. Spreitzer, H. Becker, E. Kluge, W. Kreuder, H. Schenk, R. Demandt, H. Schoo, *Adv. Mater.* **1998**, *10*, 1340.

[25] M. Mitsui, Y. Kawano, R. Takahashi, H. Fukui, *RSC Adv.* **2012**, *2*, 9921.

[26] V. Jankus, E. W. Snedden, D. W. Bright, V. L. Whittle, J. A. G. Williams, A. Monkman, *Adv. Funct. Mater.* **2013**, *23*, 384.

[27] Y. J. Bae, G. Kang, C. D. Malliakas, J. N. Nelson, J. Zhou, R. M. Young, Y. L. Wu, R. P. Van Duyne, G. C. Schatz, M. R. Wasielewski, *J. Am. Chem. Soc.* **2018**, *140*, 15140.

[28] B. vander Zee, S. Paulus, R. Q. Png, P. K. H. Ho, L. L. Chua, G. J. A. H. Wetzelaer, P. W. M. Blom, *Adv. Electron. Mater.* **2020**, *6*.

[29] A. S. Dhoot, D. S. Ginger, D. Beljonne, Z. Shuai, N. C. Greenham, *Chem. Phys. Lett.* **2002**, *360*, 195.

[30] V. Gray, A. Dreos, P. Erhart, B. Albinsson, K. Moth-Poulsen, M. Abrahamsson, *Phys. Chem. Chem. Phys.* **2017**, *19*, 10931.

[31] B. H. Wallikewitz, D. Kabra, S. Gélinas, R. H. Friend, *Phys. Rev. B - Condens. Matter Mater. Phys.* **2012**, *85*, 22.

[32] T. Shan, Z. Gao, X. Tang, X. He, Y. Gao, J. Li, X. Sun, Y. Liu, H. Liu, B. Yang, P. Lu, Y. Ma, *Dye. Pigment.* **2017**, *142*, 189.

[33] H. Lim, H. J. Cheon, G. S. Lee, M. Kim, Y. H. Kim, J. J. Kim, *ACS Appl. Mater. Interfaces* **2019**, *11*, 48121.

[34] B. Arredondo, B. Romero, A. Gutiérrez-Llorente, A. I. Martínez, A. L. Álvarez, X. Quintana, J. M. Otón, *Solid. State. Electron.* **2011**, *61*, 46.

[35] B. Romero, B. Arredondo, A. L. Alvarez, R. Mallavia, A. Salinas, X. Quintana, J. M. Otón, *Solid. State. Electron.* **2009**, *53*, 211.

[36] T. Van Woudenbergh, J. Wildeman, P. W. M. Blom, J. J. A. M. Bastiaansen, B. M. W. Langeveld-Voss, *Adv. Funct. Mater.* **2004**, *14*, 677.

[37] R. Q. Png, M. C. Y. Ang, M. H. Teo, K. K. Choo, C. G. Tang, D. Belaineh, L. L. Chua, P. K. H. Ho, *Nat. Commun.* **2016**, *7*, 1.

[38] M. Kuik, G. J. A. H. Wetzelaer, J. G. Laddé, H. T. Nicolai, J. Wildeman, J. Sweelssen, P. W. M. Blom, *Adv. Funct. Mater.* **2011**, *21*, 4502.

[39] C. Wang, Y. Liu, Z. Ji, E. Wang, R. Li, H. Jiang, Q. Tang, H. Li, W. Hu, *Chem. Mater.* **2009**, *21*, 2840.

[40] L. S. Cui, S. Bin Ruan, F. Bencheikh, R. Nagata, L. Zhang, K. Inada, H. Nakanotani, L. S. Liao, C. Adachi, *Nat. Commun.* **2017**, *8*, 1.

[41] Q. Zhang, H. Kuwabara, W. J. Potscavage, S. Huang, Y. Hatae, T. Shibata, C. Adachi, *J. Am. Chem. Soc.* **2014**, *136*, 18070.

[42] I. Rörich, A. K. Schönbein, D. K. Mangalore, A. Halda Ribeiro, C. Kasparek, C. Bauer, N. I. Crăciun, P. W. M. Blom, C. Ramanan, *J. Mater. Chem. C* **2018**, *6*, 10569.

[43] C. Jeong, C. Coburn, M. Idris, Y. Li, P. I. Djurovich, M. E. Thompson, S. R. Forrest, *Org. Electron. physics, Mater. Appl.* **2019**, *64*, 15.

[44] P. W. M. Blom, N. I. Craciun, D. M. De Leeuw, G. A. H. Wetzelaer, H. T. Nicolai, M. Kuik, *Adv. Mater.* **2014**, *26*, 512.

Chapter details

Publications

This chapter is based on the publications:

B. van der Zee, S. Paulus, R.-Q. Png, P. K. H. Ho, L.-L. Chua, G.-J. A. H. Wetzelaer, and P. W. M. Blom, Role of singlet and triplet excitons on the electrical stability of polymer light-emitting diodes, Adv. Electron. Mater. **6,** 2000367 (2020)

and

Van der, B., Li, Y., Wetzelaer, G.-J. A. H., Blom, P. W. M., Efficiency of Polymer Light-Emitting Diodes: A Perspective. *Adv. Mater.* 2022, 34, 2108887.

(Note that the second publication is a review article)

Author contributions

For the first publication:

Bas van der Zee and Sarina Paulus performed the experiments. Q.M. Koh and Q.J. Seah synthesized the *p*-pTFF-C_2F_5SIS. R.-Q. Png, P. K. H. Ho and L.-L. Chua supplied the *p*-pTFF-C_2F_5SIS. Bas van der Zee performed the simulations and wrote the manuscript with help from the co-authors. G. A. H. Wetzelaer and P. W. M. Blom proposed and supervised the project.

For the second publication:

Bas van der Zee expanded the PLED device model with the inclusion of exciton populations and interactions. Bas van der Zee carried out the experiments shown in paragraph 4 of the corresponding paper. Y. Li did the simulations and experiments regarding outcoupling in paragraph 3 of the corresponding paper. P. W. M Blom wrote the manuscript with input from co-authors.

Chapter 4: Origin of the efficiency roll-off in single-layer organic light-emitting diodes based on thermally activated delayed fluorescence

The efficiency roll-off in organic light-emitting diodes (OLEDs) based on thermally activated delayed fluorescence (TADF) is attributed to either singlet-triplet or triplet-triplet annihilation (TTA) as well as triplet-polaron annihilation (TPA). We study the origin of the efficiency roll-off on a TADF OLED consisting of a host-less single-layer emitter. Varying the charge carrier concentration at constant exciton density or the exciton density at constant charge carrier density with temperature unambiguously shows that the dominant contribution to the roll-off originates from TTA. Using an analytical model, a TTA rate constant of 1.5×10^{-18} m^{-3} s^{-1} is obtained. Our results show that single-layer TADF OLEDs are suited not only to determine the roll-off mechanism, but also provide its rate constant directly from OLED efficiency measurements.

4.1 Introduction

Thermally activated delayed fluorescence (TADF) has led to highly efficient OLEDs and are being considered as promising candidates in future display applications.[1] In practice, the maximum efficiency of a TADF OLED is commonly attained in the low voltage regime at low brightness, while with increasing voltage the efficiency decreases.[2] This phenomenon is commonly known as 'efficiency roll-off' and it is a negative effect as it reduces the efficiency at high light output. For both types of OLEDs the origin of the roll-off is a much debated topic, although triplet-triplet annihilation (TTA), triplet-polaron annihilation (TPA) and singlet-triplet annihilation (STA) are the most commonly cited responsible mechanisms (section 1.5.5).[3–6]

A straightforward approach to investigate the roll-off would be to use the steady-state solutions of the rate equations, enabling the identification of annihilation processes directly from the measured OLED light output. This steady-state approach was applied to TADF OLEDs before, where both TTA and STA were incorporated in the rate equations for the singlet/triplet density to describe the efficiency roll-off.[4,7] In these studies, the roll-off analysis was performed on a multi-layer architecture and with the TADF emitter doped in a host. A multilayer architecture is generally needed to attain high external quantum efficiency (EQE), where the several layers aid in injection, transport, light generation and blocking of charges and/or excitons. However, a multilayer structure strongly complicates a quantitative analysis of all the annihilation processes during device operation. For example, estimation of the carrier density in the emissive layer, required to analyze the role of TPA, is not straightforward. Furthermore, the photophysical properties of the TADF emitters can vary widely depending on the choice of host,[8,9] such that the obtained TTA-constant depends on the choice of host.[10] Ideally, a reliable steady-state analysis of the roll-off is performed in a model device using a single-layer architecture with an undoped emitter and nearly 100% internal quantum efficiency (IQE).

4.2 A model TADF OLED

Such a highly efficient TADF OLED based on an undoped single-layer architecture was recently demonstrated with the emitter material 9,10-bis(4-(9H- carbazol-9-yl)−2,6-dimethylphenyl)−9,10-diboraanthracene (CzDBA),[11] its chemical structure is shown in figure 4.1(b).[12] A photoluminescence quantum yield (PLQY) of >90% in the neat film, low electron- and hole-trap densities combined with balanced bipolar transport,[13] as well as efficient charge injection via Ohmic electron and hole contacts,[14] make these single-layer CzDBA OLEDs an ideal model system to uncover the device physics of OLEDs based on TADF emitters. The low trap densities stem from the fact that the lowest unoccupied molecular orbital (LUMO) and highest occupied molecular orbital (HOMO) levels of CzDBA, −3.45 eV and −5.93 eV respectively,[11] are situated close to the so called 'trap-free window',[15] which ranges from -3.6 eV to -6.0 eV with respect to the vacuum level, resulting in near trap-free electron and hole transport.[11] The absence of internal losses and balanced transport gives rise to high external quantum efficiency (EQE) values of 19% at 500 cd A^{-1},[16] meaning that for ~20% light-outcoupling efficiency an internal quantum efficiency (IQE) of ~95% is attained in the single-layer CzDBA OLED. In the present study, we examine the voltage and temperature dependence

of the EQE of CZDBA OLEDs. Using steady-state solutions to the rate equations for STA, TTA and TPA, we demonstrate that TTA is the dominant mechanism in the efficiency roll-off in our TADF OLEDs. Our analytical formulas provide a facile way to identify the roll-off mechanism and the corresponding annihilation rate directly from the OLED efficiency.

4.3 Efficiency analysis at constant voltage

(a) (b)

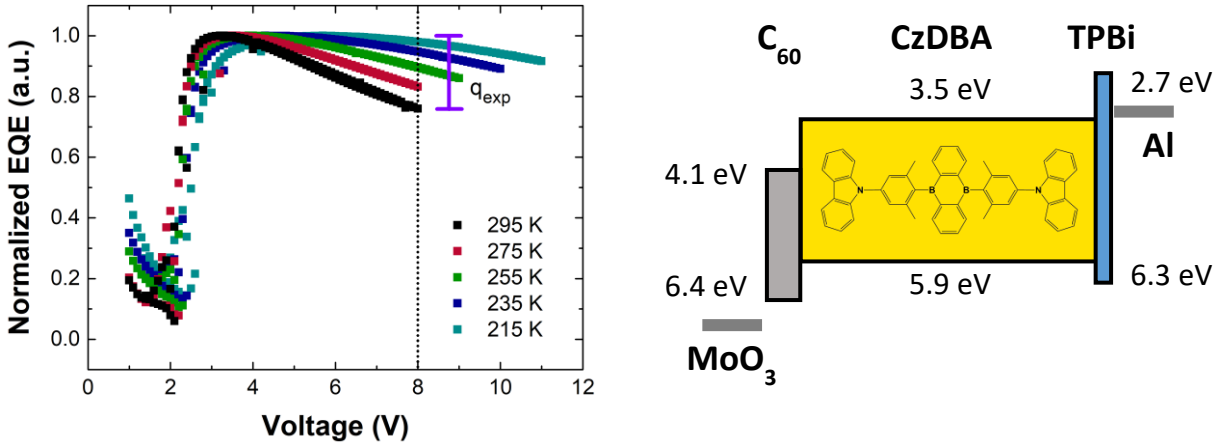

Figure 4.1: (a) Normalized temperature-dependent external quantum efficiency vs voltage for a 300 nm CzDBA OLED. The experimental quenching parameter q_{exp} is indicated graphically. **(**b) Schematic band diagram showing the device layout of a CzDBA OLED, the chemical structure of CzDBA is shown in the emissive layer. The HOMO/LUMO levels are given (f.l.t.r.) for C_{60}, CzDBA and TPBi, adopted from.[11]

Figure 4.1(a) shows the normalized external quantum efficiency (EQE) vs voltage for a 300 nm CzDBA OLED (figure 4.1(b)) at various temperatures. Going from 295 to 215 K we observe a flatter efficiency curve in combination with a shift of the maximum efficiency from 3.2 to 5.7 V. Considering one specific voltage, namely 8 V as indicated by the dotted line in figure 4.1(a), it can be seen that the efficiency increases with decreasing temperature. From single carrier devices it has been demonstrated that CzDBA exhibits low trap concentrations for both electrons and holes.[11] As a result, it was shown that already for an applied voltage of only 1.0-1.5 V the traps are nearly all filled. For the CzDBA OLED this automatically means that for a voltage 1.0-1.5 V above the build-in voltage (~2.0 V), so typically a voltage larger than 3.5 V, the OLED operates in the trap-filled limit where the current is space-charge limited. Furthermore, recombination is mainly governed by the bimolecular Langevin recombination, since due to the low amount of traps trap-assisted recombination does not play a role at higher voltages. This is further evidenced by comparing the experimental OLED current with the analytical model for double-carrier injection into a trap-free material with bimolecular recombination as dominant recombination mechanism.[17] As shown,[18] the excellent agreement between the experiment and model confirms that this OLED mainly operates in the trap-free space-charge limited regime, which implies that the carrier densities are governed by the applied voltage only, nearly independent of temperature. By cooling down the OLED, both the current and luminance at 8 V therefore drop due to the decrease of the carrier mobility with

temperature, whereas the carrier density remains nearly constant. As a result, the quenching parameter q_{exp} (figure 4.1(a)), defined as $q_{exp} = 1 - \eta_{exp}$ with η_{exp} being the normalized experimental efficiency, is only affected by a change in exciton density. The decrease of q_{exp} with decreasing temperature therefore indicates that excitons are involved in the quenching.

4.4 Efficiency analysis at constant current

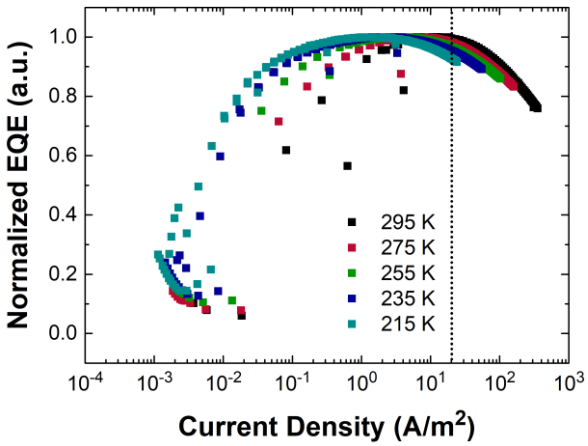

Figure 4.2: Normalized efficiency vs current density for temperatures ranging from 295 – 215 K in steps of 20 K. The dotted line indicates the efficiency at a current density of 20 A m^{-2}.

Complementing the efficiency analysis at constant voltage, the efficiency can also be examined as a function of current density, as shown in figure 4.2. At constant current density the light-output remains nearly constant, while the operating voltage and thus carrier density increases with decreasing temperature due to the temperature-dependent mobility. Consequently, a change in exciton quenching would be mainly governed by a change in carrier density in this case. Figure 4.2 shows that at one specific current density (20 A m^{-2}), as indicated by the dotted line, the efficiency and thus quenching is almost temperature invariant. This indicates that charge carriers or polarons do not play an important role in the quenching process.

4.5 Analytical theory

As a next step, we derive the efficiency from the steady-state solutions of the singlet and triplet concentrations for the various quenching mechanisms, starting with triplet-triplet annihilation. We assume uniform generation over the emission layer due to the balanced transport, such that we can write $G = \frac{J}{q \cdot d}$, with J the current density, q the elementary charge and d the emitter layer thickness. In these equations we make use of the fact that our TADF OLED is mainly loss-free with an IQE close to unity. In this case, almost all triplets eventually undergo a spin flip to the singlet state to give fluorescence. As a first step we assume that intersystem crossing does not affect the final steady-state singlet and triplet concentrations and thus is for now it is omitted in the rate equations. Furthermore, we assume that TTA only affects the triplet population eq. (1.33d). The singlet generation from TTA eq. (1.33c) has a prefactor of only 0.25, whereas the total prefactor of triplet disappearance is 1.25. Moreover, the dominant contribution to the

singlet population is not expected to be from TTA, but from rISC instead.[2] The last assumption we make is that the intrinsic triplet lifetime is long enough such that the monomolecular decay of triplets can be neglected, which agrees with an IQE near unity. This is implemented by $\tau_t \rightarrow \infty$. Typical triplet lifetimes are on the order of at least 100 µs,[19] much longer than the effective triplet lifetime that is dominated by rISC. The effective triplet lifetime for CzDBA was determined to be 3.2 µs at room temperature.[12] Following the derivation presented in Appendix A, section A.2 under the respective header, the normalized efficiency (η_{TTA}) in case of TTA is given by:

$$\eta_{TTA} = 0.25 + \frac{k_{rISC}^2}{2k_{TTA} \cdot G}\left(-1 + \sqrt{1 + \frac{4k_{TTA} \cdot 0.75G}{k_{rISC}^2}}\right). \tag{4.1}$$

The first term in eq. (4.1) represents the direct generation of singlets, which under electrical operation are produced in a singlet-to-triplet ratio of 1:3. The second term describes the singlets generated by rISC. We note that if $4k_{TTA} \cdot 0.75G/k^2_{rISC} << 1$ the η_{TTA} approaches unity using the binomial approximation ($\sqrt{1+x} \approx 1 + \frac{1}{2}x$).

Following the same approach, expressions for the normalized OLED efficiency can also be derived in case of STA and TPA, given by (Appendix A, A.2)

$$\eta_{STA} = \frac{\frac{[S]}{\tau_S}}{G} = \frac{1}{1 + \frac{k_{STA}\,\tau_S \cdot 0.75G}{k_{rISC}}}. \tag{4.2}$$

and

$$\eta_{TPA} = \frac{\frac{[S]}{\tau_S}}{G} = 0.25 + \frac{k_{rISC}}{k_{rISC} + k_{TPA} \cdot (n+p)}. \tag{4.3}$$

4.6 Establishing the dominant quenching mechanism

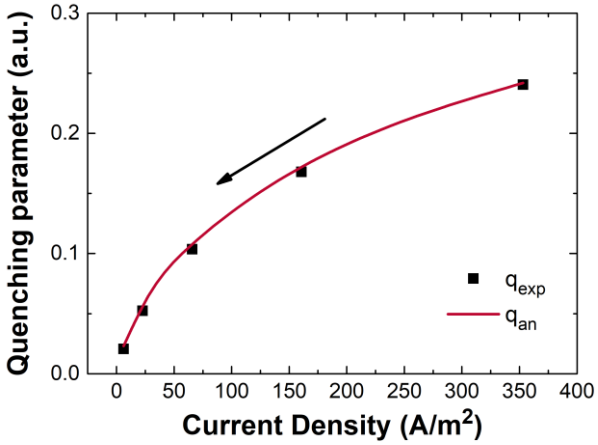

Figure 4.3: Experimental quenching parameter q_{exp} as function of current density at 8 V (symbols). The arrow indicates the direction of decreasing temperature from 295 to 215 K in steps of 20 K. Also shown is the calculated roll-off (analytical quenching parameter, q_{an}) for TTA as quenching mechanism using eq. 4.1 with k_{TTA} = 1.2x10^{-17} m^{-3} s^{-1} (solid line). This solid

line serves as a guide to the eye and was obtained by interpolating the values of q_{an} with a cubic spline.

As a next step, these steady-state solutions of the rate equations are compared with the experimentally observed efficiency roll-off. In figure 4.3 the quenching parameter q_{exp} is plotted as a function of the current density at a constant voltage of 8 V (symbols). We observe that at room temperature that the roll-off losses due to exciton quenching amount to 24% at 8 V, whereas as 215 K the losses have been reduced to 2% only.

For the case of TTA the normalized efficiency η_{TTA} depends on G, k_{rISC} and k_{TTA} eq. (4.1). The generation rate is directly obtained from the OLED current density J which is known as a function of voltage and temperature. Furthermore, for CzDBA, k_{rISC} was determined to be 3.13×10^5 s^{-1} at room temperature with a thermal activation energy of 33 meV,[21] such that k_{rISC} is known at any temperature. As a result, k_{TTA} is the only free parameter for describing the efficiency roll-off due to TTA. By setting k_{TTA} to a fixed value of 1.2×10^{-17} m^3 s^{-1}, independent of temperature, we obtain excellent agreement between the experiment and the model for TTA. The obtained magnitude for k_{TTA} is in the range of earlier reported values obtained via transient methods, typically $\sim 10^{-17}$ to $\sim 10^{-20}$ m^3 s^{-1}.[2,7,20]

In contrast, in the model for TPA eq. (4.3) at constant voltage p and n are fixed and the only contribution from temperature comes in via k_{rISC} and/or k_{TPA}. The known variation of k_{rISC} is not strong enough to explain the decrease of q_{exp} with current density and/or temperature, meaning that a strong temperature dependence of k_{TPA} would be required to explain the reduced quenching at low temperatures. However, as already indicated by the temperature independent quenching at a fixed current (figure 4.2) charge-carrier density and therefore TPA does not seem to play an important role in the efficiency roll-off of the TADF OLED. From the three quenching mechanisms considered only TTA reproduces the square-root like dependence of q_{exp} on current density/generation rate.

Having investigated the roll-off at a fixed voltage we now further establish the dominant quenching mechanism by considering the full voltage range. Figure 4.4 shows the experimental and calculated normalized efficiency vs voltage for a 300 nm CzDBA OLED, considering TTA as the dominant quenching mechanism. The efficiency decrease with voltage at room temperature is well described using a rate constant k_{TTA} of 1.2×10^{-17} m^3 s^{-1}. Since the temperature

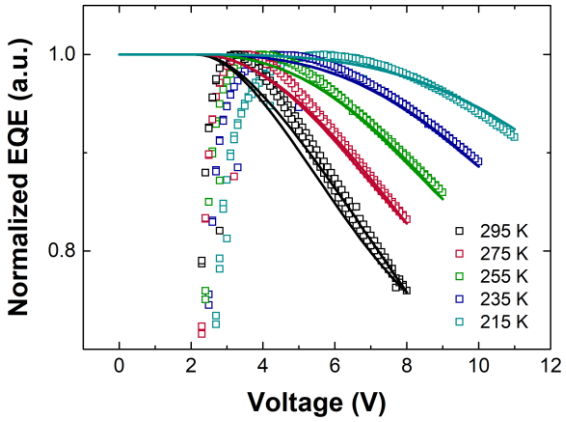

Figure 4.4: Normalized efficiency vs voltage for a 300 nm CzDBA OLED (symbols)

complemented by fits to equation 4.1 (lines) considering TTA as exciton quenching mechanism. For all fits a rate constant k_{TTA} of 1.2×10^{-17} m^3 s^{-1} has been used.

dependence of G and k_{rISC} are known the roll-off for all other temperatures can be predicted using eq. (4.1) combined with this value for k_{TTA}.

We observe that with this fixed k_{TTA} value the voltage dependence of the efficiency roll-off at all temperatures is consistently described, confirming the dominance of TTA as cause of the efficiency roll-off. The slight deviation at voltages just above the build-in voltage (~2 V at 295 K) stems from the trap filling of the small amount of electron and hole traps that are present in this material.[11] Our model is intended to study the roll-off in the trap-filled limit (>3.5 V), and does not consider the details of trapping at low voltages. Since at low voltages the roll-off shifts to higher voltages (>4 V) the agreement gets better since at higher voltages trapping does not play a role, as discussed before.

The observation that the roll-off at any temperature can be described by a fixed temperature independent k_{TTA} is surprising. In order to rationalize this experimental finding, we note that in recent kinetic Monte Carlo simulations of the TTA process,[21] it was found that in the relatively small temperature range of our study (215-295 K) the temperature dependence of TTA is weak, providing that the energetic disorder is small. Since in CzDBA the electron and hole transport are trap free and exhibit a high mobility, indicative of low energetic disorder, we suggest that the reduced disorder in combination with the limited experimental temperature regime might be the cause of our observation of a nearly temperature independent k_{TTA}.

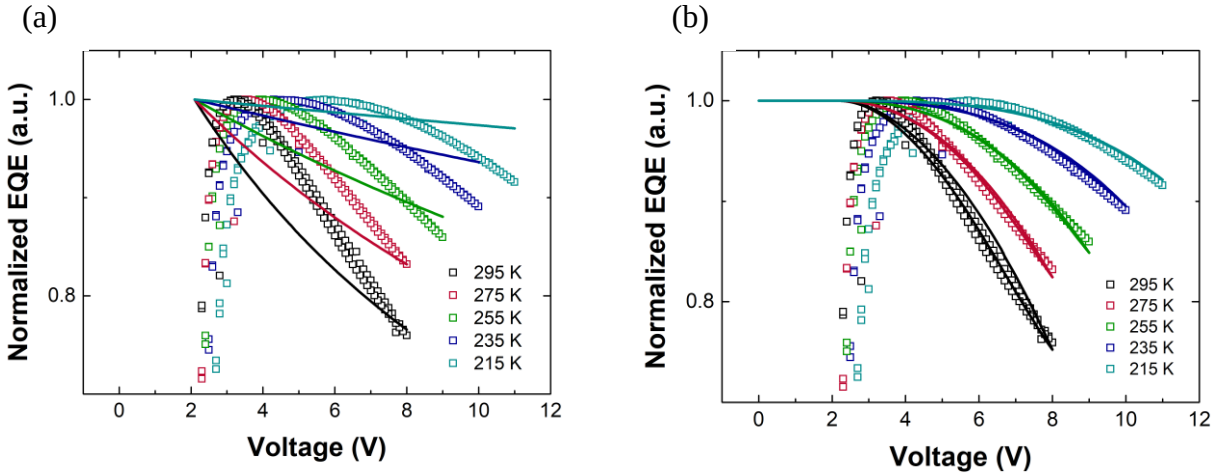

Figure 4.5: (a) Normalized efficiency vs voltage with fits to the analytical formula with TPA (eq. (4.3)). k_{TPA} is taken temperature dependent, with values presented in table 4.1. (b) Normalized efficiency vs voltage with fits to the analytical formula with STA (eq. (4.2)). k_{STA} is taken as a temperature dependent value with k_{STA} presented in table 4.1 below. For both figures the symbols represent the experimental data while the lines are fits to this data. The analytical formulas are found in section 1 above.

Table 4.1: Values of k_{TPA} and k_{STA} corresponding to the fits in figure 4.2, above.

Temperature (K)	**k_{TPA} x10^{-18} (m^3 s^{-1})**	**k_{STA} x10^{-15} (m^3 s^{-1})**

295	2.8	0.85
275	1.6	1.1
255	0.8	1.3
235	0.3	1.4
215	0.1	2

One could argue that the temperature dependence of q_{exp} at a fixed voltage can also arise from a strong temperature dependence of k_{TPA}. However, even with k_{TPA} as a fit parameter at every temperature the functional form of the voltage dependence of the roll-off cannot be described (figure 4.5(a)). For STA, the voltage dependence of the quenching process can be reasonably reproduced using a temperature dependent k_{STA} (figure 4.5(b)) However, to explain the quenching at room temperature and anomalously high rate constant k_{STA} of $1x10^{-15}$ m^3 s^{-1} has to be used, three orders of magnitude higher than previously reported.[2] Furthermore, to describe the quenching at lower temperatures k_{STA} would have to be further increased, ruling out the occurrence of this process. Consequently, by simply measuring the current density and light-output of the OLED as function of voltage, which together give the efficiency, the mechanism and magnitude of the quenching process can be directly obtained from a comparison with the analytical models.

4.7 Expanding the analytical theory

So far, we have demonstrated that the experimentally observed roll-off of the single layer TADF OLED is well described by the TTA process with a rate constant k_{TTA} of $1.2x10^{-17}$ m^3 s^{-1}. However, it should be noted that this was obtained ignoring the effect of the ISC process. It is expected that the omission of ISC has a major impact on the determination of value for k_{TTA}. Due to ISC, more triplets will be formed than we consider until now. This increased triplet population than results in a decreasing k_{TTA} in order to model the same roll-off. As next step we incorporate ISC in the rate equations in order to derive a modified expression for the OLED efficiency. Including ISC the OLED efficiency is given by:

$$\eta_{TTA,ISC} = \frac{1}{G}\frac{0.25 \cdot G + k_{rISC} \cdot [T]}{\tau_S^{-1} + k_{ISC}}. \quad (4.4)$$

With *[T]* being:

$$[T] = -\frac{k_{rISC}}{2(k_{TTA}+k_{TTA}\cdot k_{ISC}\cdot\tau_s)} + \sqrt{\frac{1}{4}\cdot\left(\frac{k_{rISC}}{k_{TTA}+k_{TTA}\cdot k_{ISC}\cdot\tau_s}\right)^2 + \frac{0.75\cdot G+k_{ISC}\cdot\tau_s\cdot G}{k_{TTA}+k_{TTA}\cdot k_{ISC}\cdot\tau_s}}. \quad (4.5)$$

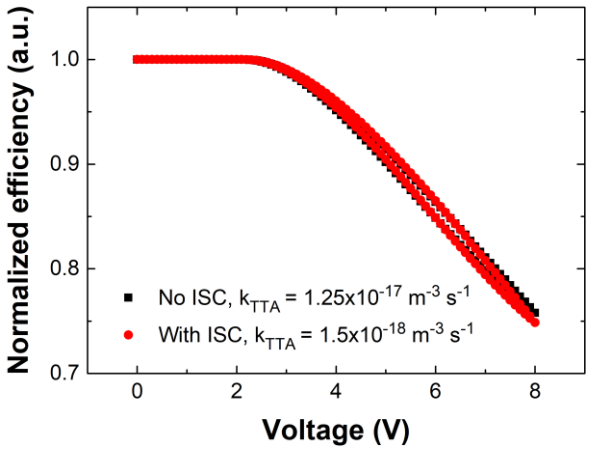

Figure 4.6: Normalized efficiency versus voltage comparing equation (5.1) (model without ISC) and equation (4.4) (model with ISC) for 295 K.

The derivation for this expression can be found in supplementary section 1. Assuming an ISC rate of $3.8\text{x}10^7$ s^{-1},[12] we remodel the efficiency decrease of the CzDBA OLED at T = 295 K using Eq 10. As shown in figure 4.6, where we plot the normalized efficiency versus voltage, comparing the analytical models with and without ISC, we find that including ISC lowers the TTA rate constant by an order of magnitude to $1.5\text{x}10^{-18}$ m^3 s^{-1}, whereas the functional dependence of the roll-off on voltage remains invariant. A rate constant k_{TTA} in the low 10^{-18} m^3 s^{-1} regime is therefore more realistic.

A big advantage of studying the effect of TTA on the roll-off in a single-layer OLED is that due to the simple device architecture the amount of injected carriers and excitons formed can be easily obtained, facilitating a quantitative analysis. Since the charge transport of CzDBA is almost balanced,[11] the recombination zone is spread over the thickness of the emissive layer. In contrast, in multilayer OLEDs the excitons are confined in a small volume. Confinement leads to more interaction between the excitons, and one could thus expect a stronger effect of TTA on the roll-off. However, another difference between the two architectures is that in a multilayer device the emitters are incorporated in a host, which will hinder the interaction between triplet excitons. These two competing processes make the study of the roll-off more complex in a multilayer OLED. Furthermore, due to the presence of many layers with various energy offsets the carrier density and exciton formation in the emissive part of the multilayer OLED are not easily determined. Therefore, our analysis of the roll-off, although more straightforward, cannot directly be extended to multilayer OLEDs with a host-guest emissive layer.

4.8 Conclusions

Summarizing, we have investigated the efficiency roll-off using a single-layer model TADF OLED based on the emitter CzDBA, in which the influence of a host and/or a multi-layer architecture do not obstruct a reliable analysis. By assessing the temperature dependent efficiency at a fixed voltage we find that the roll-off changes drastically. Opposite to this, the temperature dependent efficiency shows little change for a fixed current density. Combination of these observations shows that the efficiency roll-off of the TADF OLED is not caused by charge carriers, but originates from excitonic processes. Analytical formulas for the efficiency are derived in the case the roll-off is ascribed to either STA, TTA or TPA. By comparison with experiment we are able to discern between these different possible causes of the roll-off, pointing to TTA as the dominant mechanism. TTA is not only able to describe the efficiency loss at only one voltage, but the entire voltage range is very well described by the analytical formula presented here. As a last point of discussion, a more realistic case is presented, where ISC is included in the rate equations. It shows that an accurate determination of the triplet population will only alter the magnitude of the triplet-triplet annihilation constant, not the shape of the efficiency curve. As a result, the use of these analytical formulas provides a quick estimate of the quenching mechanism and corresponding rate constant from standard OLED characterization techniques.

4.9 Experimental section

Materials

CzDBA was obtained from Luminescence Technology Corporation and used without further purification.

References

[1] Y. Liu, C. Li, Z. Ren, S. Yan, M. R. Bryce, M. Y. W. and E. Zysman-Colman, *Nat. Rev. Mater.* **2018**, *3*, 18020.

[2] M. Hasan, A. Shukla, V. Ahmad, J. Sobus, F. Bencheikh, S. K. M. McGregor, M. Mamada, C. Adachi, S. C. Lo, E. B. Namdas, *Adv. Funct. Mater.* **2020**, *30*, 1.

[3] C. Murawski, K. Leo, M. C. Gather, *Adv. Mater.* **2013**, *25*, 6801.

[4] K. Masui, H. Nakanotani, C. Adachi, *Org. Electron. physics, Mater. Appl.* **2013**, *14*, 2721.

[5] A. Niwa, S. Haseyama, T. Kobayashi, T. Nagase, K. Goushi, C. Adachi, H. Naito, *Appl. Phys. Lett.* **2018**, *113*.

[6] S. Reineke, K. Walzer, K. Leo, *Phys. Rev. B - Condens. Matter Mater. Phys.* **2007**, *75*, 1.

[7] M. Inoue, T. Serevičius, H. Nakanotani, K. Yoshida, T. Matsushima, S. Juršenas, C. Adachi, *Chem. Phys. Lett.* **2016**, *644*, 62.

[8] K. Stavrou, L. G. Franca, A. P. Monkman, *ACS Appl. Electron. Mater.* **2020**, *2*, 2868.

[9] G. Méhes, K. Goushi, W. J. Potscavage, C. Adachi, *Org. Electron.* **2014**, *15*, 2027.

[10] D. Kasemann, R. Brückner, H. Fröb, K. Leo, *Phys. Rev. B - Condens. Matter Mater. Phys.* **2011**, *84*, 1.

[11] N. B. Kotadiya, P. W. M. Blom, G.-J. A. H. Wetzelaer, *Nat. Photonics* **2019**, 1.

[12] T.-L. Wu, M.-J. Huang, C.-C. Lin, P.-Y. Huang, T.-Y. Chou, R.-W. Chen-Cheng, H.-W. Lin, R.-S. Liu, C.-H. Cheng, *Nat. Photon.* **2018**, *12*, 235.

[13] W. Liu, N. B. Kotadiya, P. W. M. Blom, G. J. A. H. Wetzelaer, D. Andrienko, *Adv. Mater. Technol.* **2020**, *2000120*, 1.

[14] N. B. Kotadiya, H. Lu, A. Mondal, Y. Ie, D. Andrienko, P. W. M. Blom, G. J. A. H. Wetzelaer, *Nat. Mater.* **2018**, *17*, 329.

[15] N. B. Kotadiya, A. Mondal, P. W. M. M. Blom, D. Andrienko, G. J. A. H. H. Wetzelaer, *Nat. Mater.* **2019**, *18*, 1182.

[16] K. Zhang, N. B. Kotadiya, X. Y. Wang, G. J. A. H. Wetzelaer, T. Marszalek, W. Pisula, P. W. M. Blom, *Adv. Electron. Mater.* **2020**, *6*.

[17] L. M. Rosenberg, M. A. Lampert, *J. Appl. Phys.* **1970**, *41*, 508.

[18] B. van der Zee, Y. Li, G. J. A. H. Wetzelaer, P. W. M. Blom, *Adv. Opt. Mater.* **2021**, *n/a*, 2100249.

[19] O. V. Mikhnenko, P. W. M. Blom, M. A. Loi, *Phys. Chem. Chem. Phys.* **2011**, *13*, 14453.

[20] L. Zhang, H. van Eersel, P. A. Bobbert, R. Coehoorn, *Chem. Phys. Lett.* **2016**, *662*, 221.

[21] R. Saxena, T. Meier, S. Athanasopoulos, H. Bässler, A. Köhler, *Phys. Rev. Appl.* **2020**, *14*, 1.

Chapter details

Publication

This chapter is based on the publication:

van der, B., Li, Y., Wetzelaer, G.-J. A. H., Blom, P. W. M., Origin of the Efficiency Roll-Off in Single-Layer Organic Light-Emitting Diodes Based on Thermally Activated Delayed Fluorescence. *Adv. Optical Mater.* 2021, 9, 2100249

Author contributions

B. van der Zee made the analytical theory and performed the fitting. Y. Li made the devices and performed the experiments. G.-J. A. H. Wetzelaer supervised the project. P. W. M. Blom gave input on the theory and supervised the project.

Chapter 5: Numerical Device Model for Organic Light-Emitting Diodes Based on Thermally Activated Delayed Fluorescence

We present a numerical drift-diffusion model for TADF OLEDs that next to singlet and triplet generation also includes the positional dependence of intersystem crossing (ISC), reverse ISC and triplet-triplet annihilation (TTA). As experimental model system, we use a single-layer OLED based on the yellow TADF emitter 9,10-bis(4-(9H-carbazol-9-yl)−2,6-dimethylphenyl)−9,10-diboraanthracene (CzDBA), which possesses nearly trap-free transport and a high photoluminescence quantum yield. Our model accurately describes the voltage dependence of the current density and external quantum efficiency (EQE), both as a function of temperature and active layer thickness. Our model reveals that the steep increase in EQE at low voltage originates from emissive trap states, whereas the efficiency decrease at high voltage (roll-off) is dominated by TTA, with a temperature independent rate constant of $7\pm3 \times 10^{-18}$ m^3 s^{-1}. The rate constant for TTA is verified by ultrafast optical measurements. The model allows us to quantitatively disentangle the various contributions of direct and trap-assisted recombination as well as recombination following rISC to the EQE, providing a useful tool for further optimization of TADF OLEDs.

5.1 Introduction

Commercial organic light-emitting diodes (OLEDs) typically make use of phosphorescent molecules to generate electroluminescence (EL). In 2012, a new class of fully organic OLED materials emerged, using thermally activated delayed fluorescence (TADF).[1] TADF materials retained the theoretically achievable 100% IQE of phosphorescent OLEDs, but the necessity of an added toxic heavy-metal element was eliminated. Therefore, TADF materials are being treated as promising candidates for highly efficient OLEDs and they have gained considerable scientific attention in recent years.[2–5] High efficiencies have indeed been demonstrated for TADF OLEDs, often employing host-guest systems and in multilayer architectures. Due to the many variables introduced by such device design, e.g. the individual transport properties of the layers and ill-defined barriers at the heterojunctions, a quantitative understanding of the device operation of TADF OLEDs is hampered. For this reason, a comprehensive device model for TADF OLEDs is presently lacking. In contrast, single-layer polymer LEDs (PLEDs) have been successfully modelled with a well-established numerical drift-diffusion simulation program.[6–9] Also for TADF OLEDs, a simplified device structure would strongly benefit the development of a quantitative device model for TADF OLEDs.

An efficient single layer TADF OLED has recently been demonstrated with the emitter CzDBA.[10] In chapter 4, it was explained that CzDBA is an ideal model system for TADF OLEDs and in that chapter the efficiency decrease at high voltage (roll-off) of a single-layer CzDBA OLED was studied using analytical formulas.[11] Triplet-triplet annihilation (TTA) was identified to be the origin of the roll-off in EQE at high voltages. However, in this analytical approach a number of assumptions were made by neglecting the following features: the effect of intersystem crossing (ISC), the effect that TTA generates singlets, the monomolecular decay of triplets and the positional dependence of numerous quantities, such as bimolecular and trap-assisted charge recombination, in the device. Most importantly, although an analytical approach can provide insight into a specific aspect, such as the origin of the efficiency roll-off, it does not provide a full quantitative description of the efficiency and device operation of TADF OLEDs. In this study, we integrate all the previously neglected processes and features in a numerical device model in order to elucidate the TADF OLED device physics, and quantitatively describe the various contributions to the quantum efficiency. First, we discuss how the existing single-layer PLED device model with a position dependent exciton generation rate is expanded with the rate equations for singlet and triplet excitons to include forward and reverse intersystem crossing rates, as well as annihilation processes as TTA, triplet-polaron quenching (TPQ) and singlet-triplet annihilation (STA). As a next step, the model is applied to single-layer CzDBA OLEDs to describe the temperature-dependent current density and external quantum efficiency for a range of active layer thicknesses. We demonstrate that the high EQE at low voltages originates from the fact that recombination via traps in CzDBA is emissive, in contrast to the nonradiative trap-assisted recombination typically observed in PLEDs. The roll-off of the efficiency at higher voltages is well described by the TTA process at all temperatures with a rate constant of $7\pm3 \times 10^{-18}$ m^3 s^{-1}. It is furthermore demonstrated that the efficiency roll-off can be attributed to TTA, and that the incorporation of other annihilation processes like TPQ and STA cannot reproduce the experiment. Finally, the model enables us to break down the several contributions to the OLED efficiency in a quantitative way. The

availability of the presented comprehensive device model will greatly aid the further development of TADF OLEDs.

5.2 Fluorescent drift-diffusion model

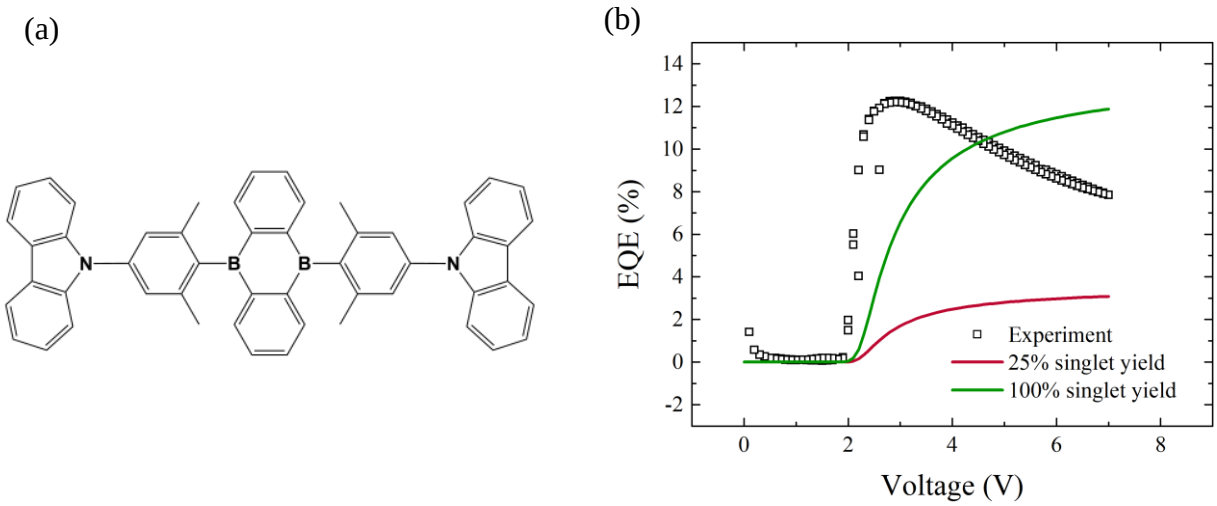

Figure 5.1: (a) Chemical structure of CzDBA. (b) Experimental external quantum efficiency versus voltage for a CzDBA OLED with an active-layer thickness of 200 nm (black symbols) and the simulated efficiencies (solid lines) for a 25% singlet yield (conventional fluorescent emitter) and a 100% singlet yield (TADF emitter), excluding excitonic interactions.

In this work, the *J-V* characteristics are modelled using numerical drift-diffusion simulations, with the field-, density-, and temperature- dependence of the mobility being described by the extended Gaussian disorder model (EGDM).[12] Such simulations were successfully employed to model the *J-V* characteristics of fluorescent PLEDs (see section 1.6.6 for an extensive description of the model).[6–9] As a first step towards modelling of the TADF OLED, the charge transport properties of the electrons and holes need to be investigated separately. The density-, field-, and temperature-dependent mobility can be obtained by fitting the current-density voltage characteristics of single-carrier devices, i.e. hole-only (HO) and electron-only (EO) devices.[12] In an earlier study, the HO and EO devices of CzDBA (figure 5.1(a)) were successfully modelled,[13] from which the obtained charge transport parameters are presented in table 5.1.

Table 5.1. Simulation parameters for the electron- and hole-only devices, the *e/h* superscripts refer to the parameter being for electrons/holes respectively. N_t/P_t are the electron/hole trap density, which are located at a trap depth E_{Nt}/E_{Pt} below the middle of the density-of-states of states of the material, with a width of $\sigma_{Nt/Pt}$.

Charge-transport parameters	**Value**
μ_0^e	5,000 $m^2 V^{-1} s^{-1}$

μ_0^h	20,000 $m^2 V^{-1} s^{-1}$
a^e	1.5×10^{-9} m
a^h	1.3×10^{-9} m
σ^e	0.115 eV
σ^h	0.135 eV
N_t	1.4×10^{22} m^{-3}
P_t	1.7×10^{22} m^{-3}
$E_{N_t} = E_{P_t}$	0.65 eV
$\sigma_{N_t} = \sigma_{P_t}$	0.1 eV

The measured room temperature mobilities of the electrons and holes are well balanced, being $\mu_e = 5 \times 10^{-5}$ $cm^2V^{-1}s^{-1}$ and $\mu_h = 3 \times 10^{-5}$ $cm^2V^{-1}s^{-1}$, respectively. Furthermore, with an ionization energy of 5.9 eV and electron affinity of 3.5 eV, the energy levels of CzDBA are located inside the energy window for trap-free charge transport in organic semiconductors.[14] However, as shown in table 5.1, the electron and hole transport is not completely trap free, but the obtained trap density of ~10^{22} m^{-3} is typically an order of magnitude lower than for the universal traps that are attributed to oxygen and/or water complexes, for which the density is in the 10^{23} m^{-3} regime. With the electron and hole transport parameters known, the CzDBA OLED can be modelled. As an intermediate step, we calculate the efficiency of a conventional fluorescent OLED, using the charge-transport parameters obtained for CzDBA. For the light output we base our model on rate equations as outlined in section 1.6.7.

For fluorescent LEDs we take the local Langevin recombination rate $R_L(x)$ as the generation rate $G(x,t)$ for excitons and without the addition of further processes this is related to the local emissive singlet density $[S(x,t)]$ as $[S(x,t)] = 0.25G(x,t) \cdot \tau_s$, with τ_s the singlet exciton lifetime. This result can be obtained by solving equation (1.33a) in steady state. The total light output is then given by integrating the local emissive recombination rate $0.25G(x,t)$ over the device thickness. This leads to the conventional 'fluorescent' efficiency in figure 5.1(b) as the red line, while the experimental efficiency of a 200 nm CzDBA OLED at room temperature is shown as black symbols. The CzDBA OLED is essentially a single-layer device, with a neat film of CzDBA sandwiched between Ohmic electron and hole contacts. The fabrication and full device structure of these single-layer CzDBA OLEDs was outlined previously.[10] We observe that the predictions of the model strongly deviate from the experimental efficiency, most notably the simulation underestimates the efficiency and the voltage dependence does not match the experiment. The reason for the too low efficiency values is straightforward: fluorescent models assume that only 25% of the generated excitons contributes to the light output, explaining the approximate factor 3 between the maximum of the experiment and the maximum

calculated efficiency (red line). Therefore, as a next step, the exciton dynamics appropriate to TADF should be taken into account.

5.3 TADF model

For this purpose, rate equations are a well-known approach and have been applied previously to study photoluminescence (PL) and EL transients as well as investigate the efficiency of TADF devices.[11,15,16] Rate equations for the singlet [$S(x,t)$] and triplet [$T(x,t)$] density take the form of linear differential equations:

$$\frac{d[S(x,t)]}{dt} = 0.25 \cdot G(x,t) - \frac{[S(x,t)]}{\tau_s} + k_{rISC} \cdot [T(x,t)] - k_{ISC} \cdot [S(x,t)], \quad (5.1)$$

$$\frac{d[T(x,t)]}{dt} = 0.75 \cdot G(x,t) - \frac{[T(x,t)]}{\tau_t} - k_{rISC} \cdot [T(x,t)] + k_{ISC} \cdot [S(x,t)], \quad (5.2)$$

where $G(x,t)$ [m^{-3} s^{-1}] is the local generation rate incorporating R_L, $k_{(r)ISC}$ [s^{-1}] the (reverse) intersystem crossing rate and $\tau_{s/t}$ [s] the singlet/triplet lifetime. Quantities denoted as a function of x are taken as position-dependent quantities in the simulations, whereas t denotes a time dependence.

We note that both rate equations assume that there is only one relevant excited singlet and triplet level. Together with the singlet ground state, one arrives at a model with three relevant energy levels. As reports from different groups have pointed out,[17,18] a small singlet-triplet gap only partly explains an efficient spin flip between two charge transfer (CT) states. The spin-orbit and vibronic coupling must be considered as well, and therefore the importance of a triplet locally excited states (^{3}LE) in rISC was recognized. For example, a four-level model, where a higher lying triplet state was included, has been used to explain the photo physics of TADF emitters previously.[19] Omitting LE singlet levels on the one hand is justified by the fact that they generally vanish after ~5 ns,[20] a consequence of the fact that their locally excited nature does not allow them to be repopulated via rISC. The light output that originates from LE singlets in steady state will thus be negligible compared to the contribution from the fluorescence of CT singlets. LE triplet states on the other hand have been shown to mix efficiently with CT triplet states, making it possible to consider one effective triplet level coupled to the singlet state through an effective k_{rISC}.[20] Furthermore, it has been shown that efficient TADF is obtained between mixed singlet and triplet states with different CT/LE contributions.[21] The exact electronic character (CT, LE or mixed) of the triplet is therefore not of relevance in our device model and whereas in reality a spin flip proceeds via a local intermediate energy state, a three-level model embeds the salient features of TADF photophysics and can therefore be reliably employed.

Table 5.2. Photophysical parameters obtained from the photoluminescence decay of CzDBA,[22] as used in the simulation. *Note that the exact value of the triplet lifetime is unknown, but we take it to be sufficiently long such that phosphorescence becomes a negligible process, as it should be in the temperature range we are considering (295 – 215 K).

Photophysical parameters	Value
k_{ISC}	1×10^6 s^{-1}
k_{rISC}	2.2×10^5 s^{-1}
ΔE_{ST}	33 meV
τ_s	98 ns
τ_t	100 μs*

The rate equations ((5.1) & (5.2)) can be solved in steady state to obtain [$S(x)$] and [$T(x)$] at every voltage, using values for $k_{(r)ISC}$ and other photophysical parameters published previously,[22] but for completeness we present them here again in table 5.2. The steady-state local singlet concentration [$S(x)$], as derived in section 1 of the Supplemental Material, is given by:

$$[S(x)] = \frac{0.25 \cdot G(x) + [T(x)] \cdot k_{rISC}}{\tau_s^{-1} + k_{ISC}}. \quad (5.3)$$

Whereas the derivation of the local triplet density [$T(x)$] can be found in Appendix A, section A.3.

5.4 Light emitting traps

Incorporation of the exciton dynamics in the TADF OLED device model is done by using the local triplet concentration to obtain the singlet concentration (equation (5.3)). The exciton density is divided by τ_s to obtain the recombination rate, which after integration over the device thickness and dividing by the number of electrical charges per unit time J/q gives the internal quantum efficiency. Experimentally, the EQE of 19% for an 80 nm device is reduced to around 12% for a 200 nm device, as a result of the non-ideal optical cavity, reducing the outcoupling efficiency.[23] Taking into account the forward and reverse intersystem crossing, as well as the optical outcoupling efficiency, we arrive at the simulated green line in figure 5.1(b), which now reaches the maximum observed experimental EQE, but we still observe a discrepancy between experiment and theory over the whole voltage range. For voltages just above the build-in voltage (V_{bi}) the experimental EQE increases much faster than the predicted green line. Studies on PLEDs have shown that trap-limited transport causes a competition between nonradiative trap-assisted SRH and radiative Langevin-type bimolecular recombination, where the stronger scaling with charge density of the latter leads to a rise and ultimately a plateau in the efficiency as function of voltage.[24] Using the trapping parameters obtained from single-carrier devices, the green line indeed displays this behavior, whereas the experimental efficiency increases in an almost vertical fashion just after V_{bi}, a situation that typically occurs when (almost) no traps are present in the material. These apparently conflicting findings can be reconciled by assuming that the majority of the trap states in CzDBA are emissive. As a first indication that CzDBA

contains light-emitting traps we show that these traps can be differentiated from the main fluorescence peak in a PL spectrum. In the following reference[25] we de-convoluted the PL spectrum into several Gaussian peaks.[26,27] The PL spectrum is asymmetric, exhibiting a broad Gaussian profile with a maximum located 0.65 eV below the middle of the main fluorescence peak. This corresponds exactly to the energy difference between the middle of the material DOS and the middle of the trap DOS found from single-carrier devices (table 5.1), and therefore we assign this lower-energy part of the spectrum to emissive recombination via trap states.

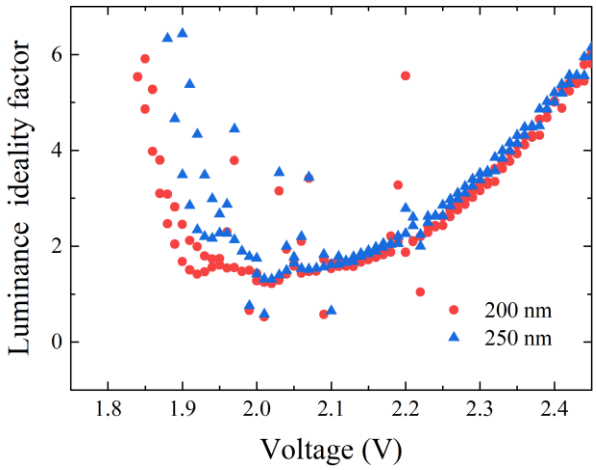

Figure 5.2: Luminance ideality factor versus voltage for two different CzDBA layer thicknesses

As a second indication that emissive trap-assisted recombination takes place, we calculated the ideality factor η_L of the luminance using the equation $\eta_L = \left(\frac{k_B T}{q}\frac{\partial \ln L}{\partial \ln V}\right)^{-1}$. The ideality factor can indicate the type of recombination, as it amounts to 1 for bimolecular and up to 2 for Shockley-Read-Hall (SRH) recombination.[24] A plot of the ideality factor can be found in figure 5.2 where we extract the ideality factor from the plateau value. We observe that η_L exceeds 1 (~1.5), meaning that a substantial part of the light-output in this voltage regime stems from trap-assisted recombination. In the simulation, we therefore included that SRH-recombination contributes to the light output, by incorporating R_L as well as R_{SRH} into $G(x,t)$, leading to a steep increase of the efficiency with voltage. Although the precise origin of these light-emitting traps (LETs) is still under investigation, we speculate that they might originate from aggregated CzDBA molecules.[28,29] This is in line with publications reporting that carbazole moieties have the tendency to dimerize.[29,30] An aggregated state would still be radiative, since the molecule is intact, but it could possess slightly lower energy levels that would show up as an electrical trap in single-carrier and OLED devices. This would also explain that in spite of the CzDBA energy levels being in the trap-free energy window with regard to oxygen/water trapping, there is still a low trap concentration present with traps of a more structural origin.

5.5 Efficiency roll-off

As a next step, we now address the mismatch between the calculated green line (figure 5.1(b)) and the experiment at higher voltage. A longstanding problem for the efficiency of both phosphorescent and TADF OLEDs is their efficiency decrease (roll-off) with increasing voltage and (thus) brightness. Several mechanisms for explaining the origin of the roll-off have been suggested, including triplet-triplet annihilation (TTA),[31–34] triplet-polaron quenching (TPQ)[33] and singlet-triplet annihilation (STA).[15,35] Here, we will first focus on TTA, as it was reported to be the dominant roll-off mechanism in CzDBA OLEDs following an analytical approach.[11] A discussion of the other two quenching processes will follow later.

TTA reduces the triplet population and enhances the singlet population at the same time. In the rate equation one can incorporate TTA by adding a term $+0.25 \cdot k_{TTA} \cdot [T(x,t)]^2$ to the differential equation for the singlet density (equation (5.1)) and additionally $-1.25 \cdot k_{TTA} \cdot [T(x,t)]^2$ to the differential equation for the triplet density (equation (5.2)). After solving these equations in steady state (Appendix A, A.3, TTA header) including TADF dynamics, it leads to the full expression for the two exciton densities, given by

$$[S(x)] = \frac{0.25 \cdot \tau_S \cdot G(x) + k_{rISC} \cdot \tau_S \cdot [T(x)] + 0.25 \cdot k_{TTA} \cdot \tau_S \cdot [T(x)]^2}{1 + k_{ISC} \cdot \tau_S}. \tag{5.4}$$

And

$$[T(x)] = -2\frac{\tau_t^{-1} + k_{ISC} \cdot \tau_S \cdot \tau_t^{-1} + k_{rISC}}{5 \cdot k_{TTA} + 4 \cdot k_{TTA} \cdot k_{ISC} \cdot \tau_S} + \sqrt{4 \cdot \left(\frac{\tau_t^{-1} + k_{ISC} \cdot \tau_S \cdot \tau_t^{-1} + k_{rISC}}{5 \cdot k_{TTA} + 4 \cdot k_{TTA} \cdot k_{ISC} \cdot \tau_S}\right)^2 + 4 \cdot \frac{0.75 \cdot G(x) + k_{ISC} \cdot \tau_S \cdot G(x)}{5 \cdot k_{TTA} + 4 \cdot k_{TTA} \cdot k_{ISC} \cdot \tau_S}}. \tag{5.5}$$

5.6 Validation of the TADF model: analysis of CzDBA OLEDs

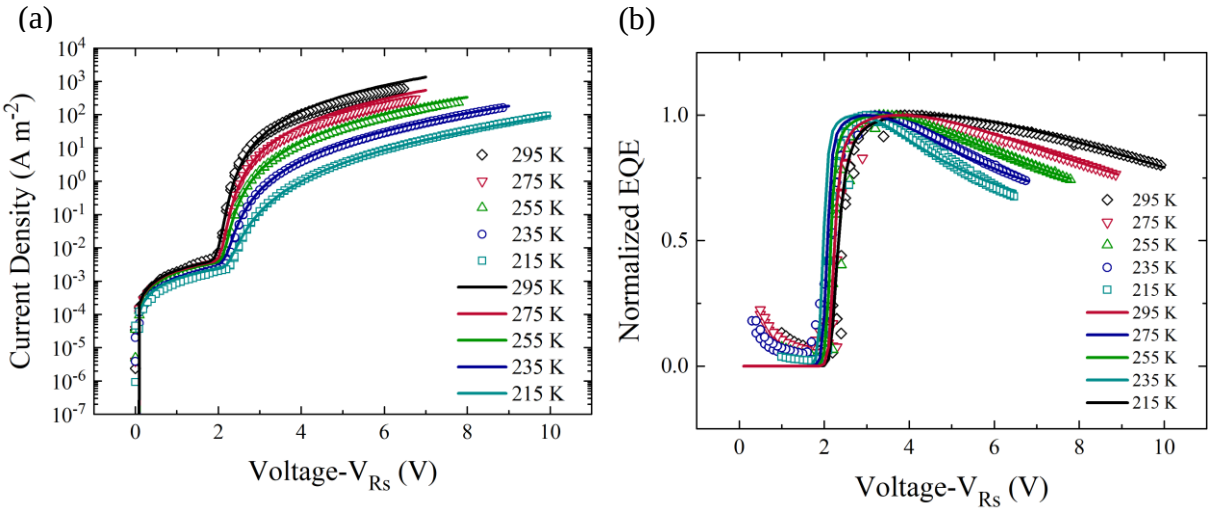

Figure 5.3: Temperature dependent characterization of a 200 nm CzDBA OLED; (a) Current density versus voltage corrected for the series resistance R_s of the electrodes and (b) normalized EQE against voltage. The open symbols correspond to experimental data whereas the solid lines represent the simulations for various temperatures.

Inserting $[T(x)]$ into $[S(x)]/\tau_s$ (via equations (5.5) and (5.4)), dividing it by J and normalizing to the maximum then leads to the normalized OLED efficiency. The experimentally validated HO/EO parameters serve as input for calculation of the double-carrier current density. For calculation of the light-output, next to the conventional Langevin recombination we also include emissive SRH-recombination from traps, as well as TTA, in order to describe the voltage dependence of the efficiency. In figure 5.3, the experimental and simulated temperature-dependent current density (figure 5.3(a)) and efficiency (figure 5.3(b)) as a function of voltage are presented for a 200 nm CzDBA OLED. We observe that with these processes included, the model is able to provide an excellent description of both the current-density and efficiency as a function of voltage. Since the electrical parameters were verified from single-carrier devices and the photophysical parameters were determined from a transient photoluminescence (TrPL) study, in this procedure the only fit parameter used to simulate the roll-off is k_{TTA}.

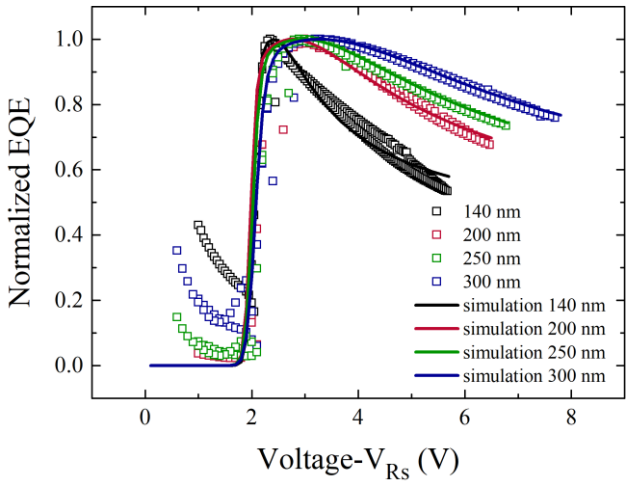

Figure 5.4: Normalized quantum efficiency vs voltage for different CzDBA layer thicknesses complemented by numerical simulations.

In figure 5.4, we present the fits to various emitter layer thicknesses. We find that the efficiency roll-off for all thicknesses is well described with our position dependent model by $k_{TTA} = 7\pm3 \times 10^{-18}$ m^3 s^{-1}. The obtained value of k_{TTA} is comparable to values obtained for a phosphorescent emitter lightly doped in a host[36] and to values obtained from transient methods,[31,37] which vary typically between ~10^{-18} to ~10^{-19} m^3 s^{-1}. Surprisingly, we find that a single k_{TTA} value fits the entire investigated temperature range (295-215 K). Recently, a kinetic Monte Carlo study of TTA in conjugated organic semiconductors found that temperature dependence of TTA is weak in our investigated temperature range,[34] given that the energetic disorder is small. The high mobilities of CzDBA in addition to the almost trap free transport are indicators of a low disorder and might explain the temperature independent k_{TTA} in our limited temperature range.

5.7 Optical verification of k_{TTA}

In order to verify the TTA rate constant found in OLEDs we turn to ultrafast optical measurements, in which *neat* films of CzDBA are studied in order to retain a morphology as close as possible to the thin film used in an OLED. Time resolved photoluminescence (TrPL)

data can be analyzed by rate equations in order to reliably extract the photophysical properties of TADF materials as well as extracting rate constants for various annihilation processes.[22] Optically, a 3-state model for a TADF OLED is given by the following equations:

$$\frac{d[S]}{dt} = \frac{[S_0]}{dt} - \frac{[S]}{\tau_s} - k_{ISC}[S] + k_{rISC}[T] - k_{SSA}[S][S] - k_{STA}[S][T] + 0.25k_{TTA}[T][T]. \quad (5.6)$$

$$\frac{d[T]}{dt} = -\frac{[T]}{\tau_T} + k_{ISC}[S] - k_{rISC}[T] - 1.25k_{TTA}[T][T]. \quad (5.7)$$

Where $[S_0]$ is the initial singlet density determined from the optical excitation density,[22] k_{SSA} *is* the singlet-singlet annihilation constant, k_{STA} is the singlet-triplet annihilation constant and k_{TTA} the triplet-triplet annihilation constant. The value of a particular annihilation coefficient can simply be set to zero in order to exclude the contribution of that specific quenching processes. In CzDBA the PLQY is >90% in neat film (chapter 4), indicative of low amounts of non-radiative decay. In case that non-radiative decay needs to be taken into account another factor of $-k_{nr}[S]/[T]$ needs to be taken into account.[38]

Equations (5.6) and (5.7) are solved in a numerical fashion using the finite difference method with a sufficiently small time step of 5 ns. The rate constants k_{ISC}, k_{rISC} and τ_s can be reliably extracted from fitting the normalized PL data to $[S]$ for lower power densities, where quenching does not play an important role.[22] The power dependence then gives information about the various quenching constants. Detailed insights into how the various photophysical rate constants influence the TrPL decay of TADF materials are given in Appendix C, figure C.1.

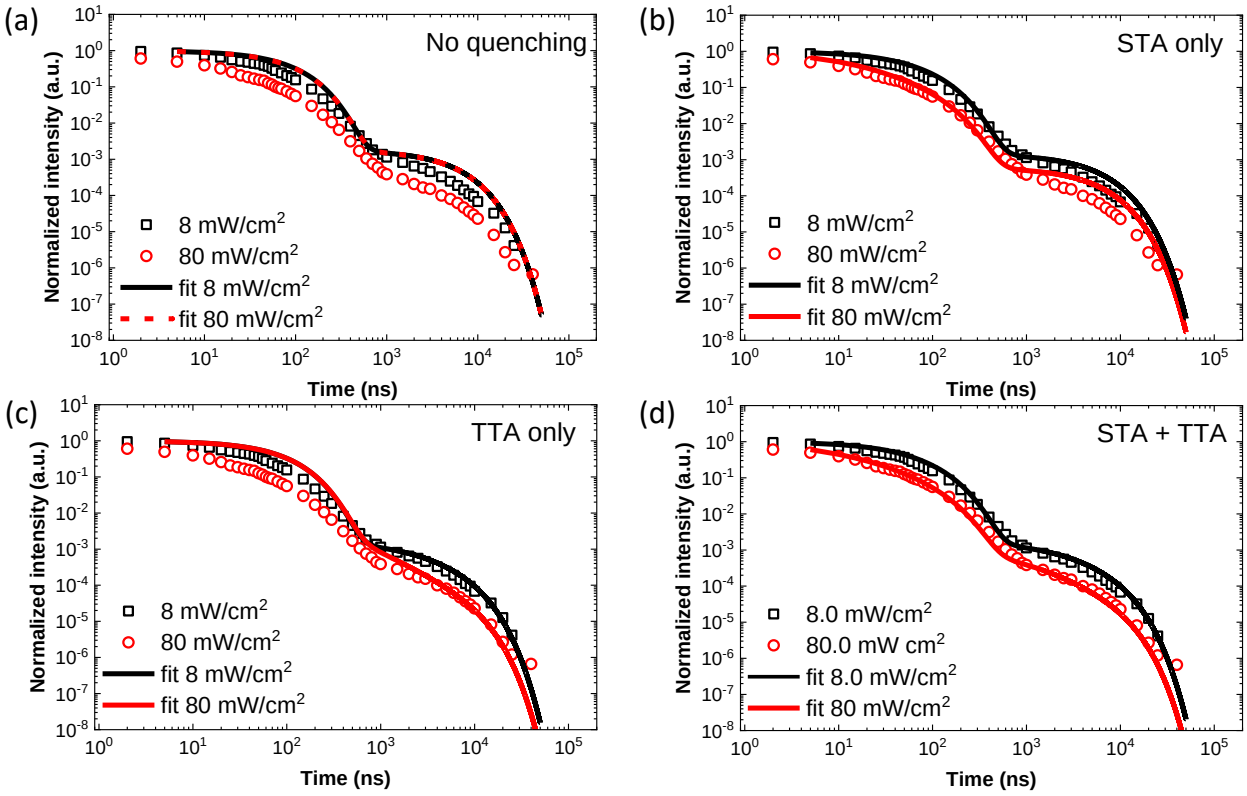

Figure 5.5: Normalized PL intensity versus time for (a) no quenching processes, (b) only STA, (c) only TTA and (d) complete. Open symbols represent the measured data whereas the lines correspond to a fit with our kinetic model.

The result of the rate equation modelling is given in figure 5.5, where several combinations of quenching constants are explored. No quenching, as in figure 5.5(a), obviously leads to no power dependence. We find that incorporating STA *or* TTA fits the prompt- or delayed-fluorescence respectively, as seen in figure 5.5(b) & (c). Only TTA in combination with STA (figure 5.5(d)) provides a good fit for the entire time range of every power density. We find values for the rate constants as follows: $k_{TTA} = 8 \times 10^{-18}$ m^3 s^{-1} and $k_{STA} = 2.5 \times 10^{-17}$ m^3 s^{-1}. Another possible decay process, namely SSA, was found not to be a major contribution,[22] in agreement with previous findings.[15] The need to include STA in the optical model, yet not in the electrical one is likely connected to the difference in exciton generation. Whereas optically only singlets are generated, electrically singlet:triplet excitons are formed in a 1:3 ratio, according to spin statistics. The difference in exciton population explains the prevalence of TTA in OLEDs, whereas this does not necessarily have to hold in TrPL experiments. The takeaway message is that the optically determined k_{TTA} of 8×10^{-18} m^3 s^{-1} corresponds well to the electrically determined one, which amounts to 7×10^{-18} m^3 s^{-1}.

5.8 Comparison TADF model to analytical formulas

Next to our TrPL study, we showed in chapter 4 that a straightforward analytical formula neglecting ISC can already provide a reasonable description of the CzDBA OLED efficiency roll-off, where the analysis of a 300 nm thick device led to a k_{TTA} of 1.5×10^{-17} m^3 s^{-1},[11] a factor two higher than obtained from our more comprehensive model here. The analytical formula was based on several assumptions, most notably it overlooked ISC and the position-dependent generation of the excitons and it is therefore instructive to see how these two assumptions change the fitted k_{TTA} value.

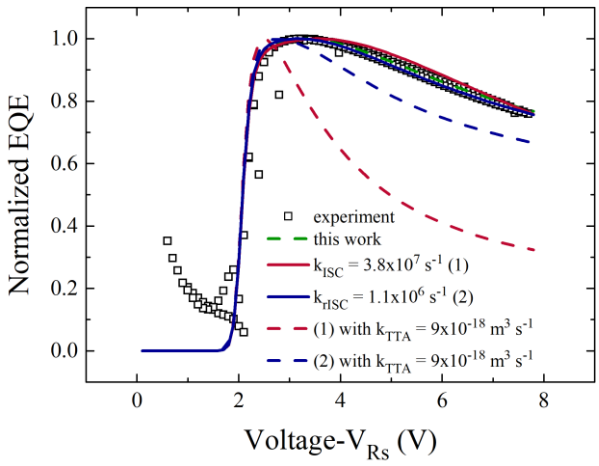

Figure 5.6: Normalized efficiency versus voltage for a 300 nm CzDBA OLED at 295 K. The solid lines correspond to fits with a different (reverse) intersystem crossing rate and a different k_{TTA}. The dashed lines are fits with a different (reverse) intersystem crossing rate (corresponding to (1) or (2)), but with the k_{TTA} determined from this work.

The impact of the intersystem crossing rate on k_{TTA} has been discussed in earlier work.[11] To reiterate, enhancing k_{ISC} increases the triplet population and therefore lowers the fitted k_{TTA} value, without a drastic change in the shape of the efficiency. In the initial report on a host:guest system with CzDBA as emitter, a k_{ISC} of 3.8×10^7 s^{-1} was reported.[39] Using this k_{ISC} rate would lower k_{TTA} to a value of 1.5×10^{-18} m^3 s^{-1} in the analytical analysis.[11] However, our recent TrPL study done on CzDBA neat films showed that the reported k_{ISC} was overestimated since in the analysis of the PL decay annihilation processes like TTA were not incorporated.[22] Taking these processes into account a k_{ISC} of to 1×10^6 s^{-1} was obtained, which is also used in this work. To further illustrate the sensitivity of k_{TTA} to ISC and rISC we plot in figure 5.6 the normalized efficiency versus voltage of a 300 nm OLED at 295 K for the earlier reported values of k_{ISC} as well as the currently used values obtained from PL decay.[25] The dashed green line represents the values of k_{ISC} and k_{rISC} used in this work together with a k_{TTA} of 9×10^{-18} m^3 s^{-1}, which is also in very good agreement with the k_{TTA} of 8×10^{-18} m^3 s^{-1} obtained from PL decay measurements. Increasing k_{ISC} to 3.8×10^7 s^{-1} and simultaneously reducing k_{TTA} to 2.5×10^{-18} m^3 s^{-1} still provides still a good fit (red solid line). The same holds for k_{rISC}, where changing it from 2.2×10^5 to 1.1×10^5 s^{-1} can still provide a good fit if k_{TTA} is reduced to 2×10^{-18} s^{-1} (blue solid line). For comparison, the red and blue dashed lines with the correct k_{TTA}, but a different $k_{(r)ISC}$, are severely off.

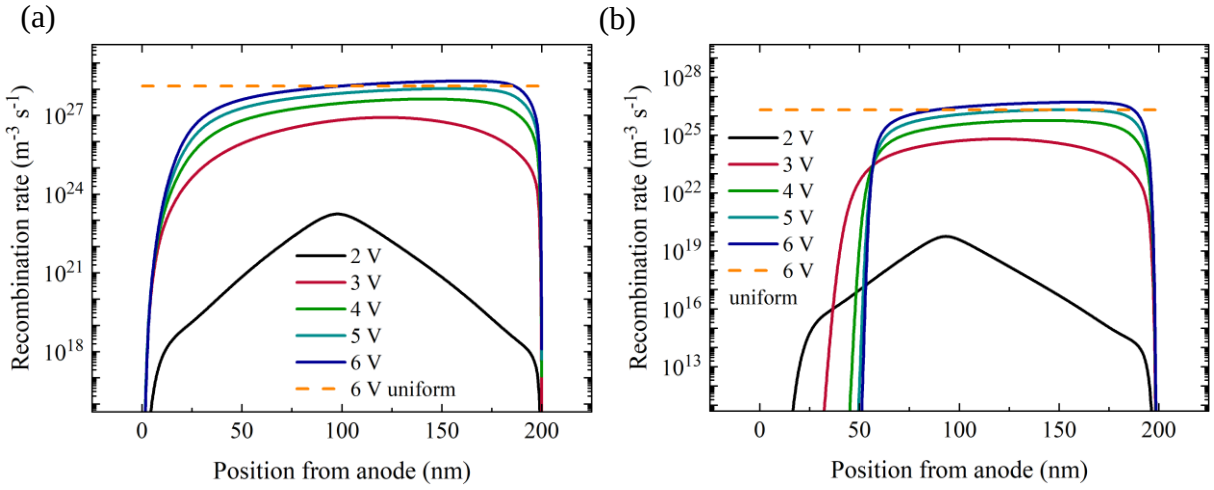

Figure 5.7: Recombination rate versus distance from the anode for a 200 nm CzDBA OLED at various voltages for (a) 295 K and (b) 215 K. The dashed orange line corresponds to a uniform exciton profile.

Another feature that was not considered in the analytical approach is the non-uniformity of the exciton profile in the device.[11] Here, we can investigate to what extent this impacts the fitted k_{TTA} value. In phosphorescent multi-layer OLEDs, a uniform exciton profile is justified by the narrow width of the emissive layer.[31] The simulated recombination profile for a single-layer 200 nm OLED at room temperature is presented in figure 5.7(a), and it shows that the balanced transport leads to a broadened recombination zone. Moreover, for voltages around the maximum EQE (2-3 V), it is clearly seen that the peak of the recombination profile is situated almost in the middle of the device. This is a favorable situation,[40] since it minimizes quenching of excitons at metallic contacts, and a broadening of the recombination zone naturally decreases the impact of TTA. Apart from the recombination profile being slightly voltage dependent, the recombination profile of CzDBA also shifts and narrows at lower temperatures. From table 5.1

we see that the disorder for holes (0.135 eV) is larger than that for electrons (0.115 eV), leading to increasingly imbalanced transport with lower temperature due to the decreased probability of thermally activated hopping at lower temperatures for holes. This is reflected in the recombination profile at 215 K which is presented in figure 5.7(b). Because of the temperature scaling of the mobility, the current and therefore the recombination rate are naturally lower at decreased temperatures, but besides this we also observe a shift of the recombination profile away from the anode, due to imbalanced transport. As TTA is influenced by the local density of excitons in the device, the positional dependence should play a role in the fitted k_{TTA}. This is illustrated in the following reference,[25] where for a 200 nm device we use a uniform exciton profile for the calculation of TTA and again take k_{TTA} as a free parameter to fit the efficiency. At 295 K there is a slight change in k_{TTA} from 4×10^{-18} to 5×10^{-18} m^3 s^{-1}, whereas at 215 K we need an increased k_{TTA} of 7×10^{-18} m^3 s^{-1} to fit the efficiency. The overall higher k_{TTA} values when a uniform exciton profile is considered result from the fact that the uniform exciton profile lies below the peak of the position dependent profile (figure 5.7(a) & (b)) Since the TTA-term in the triplet rate equation scales with the square of the triplet concentration, it results in a stronger effect of TTA when the positional dependence is considered, and as such the k_{TTA} needed to fit the same roll-off is lower. When the position dependence is not included one might conclude that k_{TTA} increases with decreasing temperature, but since k_{TTA} is a diffusion dominated process this situation is not physically meaningful. This highlights the importance of using a position dependent exciton profile, as in that case these effects are automatically taken into account.

5.9 Effect of other quenching processes on the efficiency

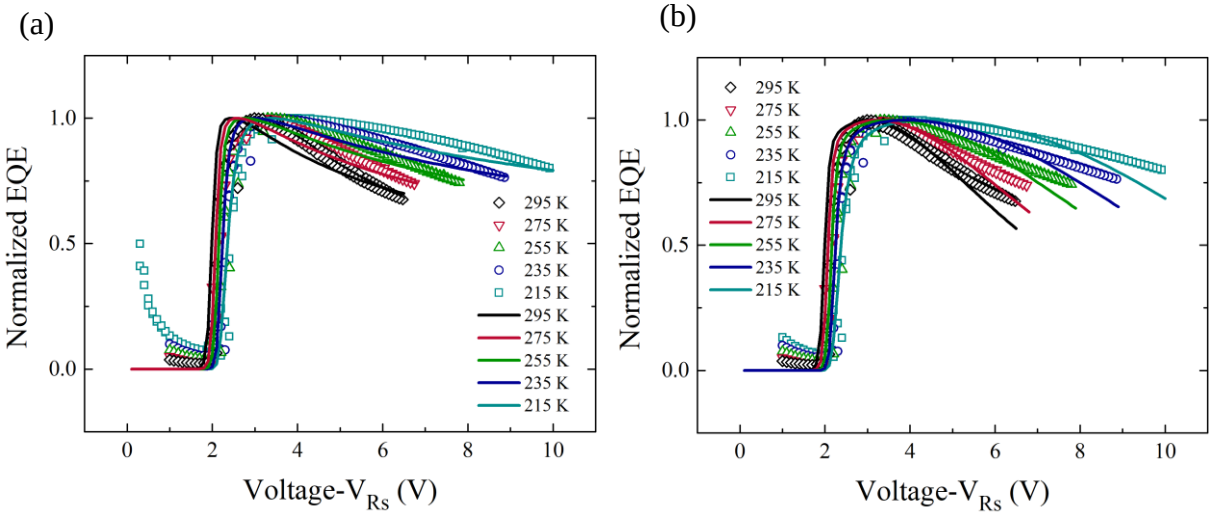

Figure 5.8: Temperature dependent normalized EQE versus voltage plots for a 200 nm OLED. The open symbols correspond to the experiment, whereas the lines correspond to the simulations taking (a) TPQ or (b) STA as quenching process. The values of k_{TPQ}/k_{STA} for every temperature can be found in table 5.3.

Table 5.3. Values of the rate constants for TPQ and STA for the investigated temperature range. The extracted rate constants correspond to the fits in figure 5.8(a) & (b).

Temperature [K]	k_{TPQ} [$m^3 s^{-1}$]	k_{STA} [$m^3 s^{-1}$]
295	3.0×10^{-18}	6.0×10^{-17}
275	2.0×10^{-18}	8.0×10^{-17}
255	1.3×10^{-18}	9.5×10^{-17}
235	9.0×10^{-19}	1.4×10^{-16}
215	6.0×10^{-19}	1.9×10^{-16}

As a next step, we study the effect of TPQ and STA on the efficiency roll-off of the TADF OLED by analyzing the shape of the simulated efficiency curves. The derivation of the rate equations including these two other processes are presented in appendix A, section A.3 under their respective header. Two other processes that could impact the roll-off are singlet-polaron quenching (SPQ) and/or singlet-singlet annihilation (SSA). We note that the role of SSA is controversial, either being considered a significant contribution to the roll-off,[41–43] whereas other works deem SSA unimportant,[22,35] making it necessary to consider its significance in this study. In our recent TrPL study on CzDBA neat films we found that SSA was not a major decay process (**5.7**) which justifies neglecting it in our OLED analysis. Turning our attention to SPQ, the triplet density exceeds the singlet density often by more than an order of magnitude under steady state conditions, making TPQ a far more relevant process than SPQ. Furthermore, reported rate-constants for SPQ are in the order of 10^{-20} m^3 s^{-1}.[43] Both these factors combined mean we can also neglect it in our OLED analysis.

It is observed in figure 5.8(a) that the shape of the simulated efficiency with TPQ exhibits a fast drop and a subsequent flattening at higher voltage. This is contrasting with the experiment, which decreases more rapidly with increasing voltage than TPQ predicts. We lowered k_{TPQ} with decreasing temperature since it slightly improves the fitting (table 5.3), nevertheless at all temperatures TPQ fails to reproduce the shape of the experimental efficiency. Just after V_{bi}, the number of injected carriers is high relative to the number of excitons, and consequently the product of excitons and carriers can lead to a stronger roll-off than the product of two excitons, which is why TPQ shows a fast drop just after V_{bi}. At higher current densities the number of excitons surpasses the number of carriers due to the stronger scaling of excitons with the current density, $[S]/[T] \sim J$ while $n/p \sim J^{1/2}$. With this straightforward argument we can already explain why TPQ will flatten the current efficiency more than TTA. Since it does not match the voltage dependence of the experimental efficiency, it corroborates once again that TPQ is not the dominant roll-off mechanism.

5.10 Quantitative breakdown of the TADF OLED efficiency

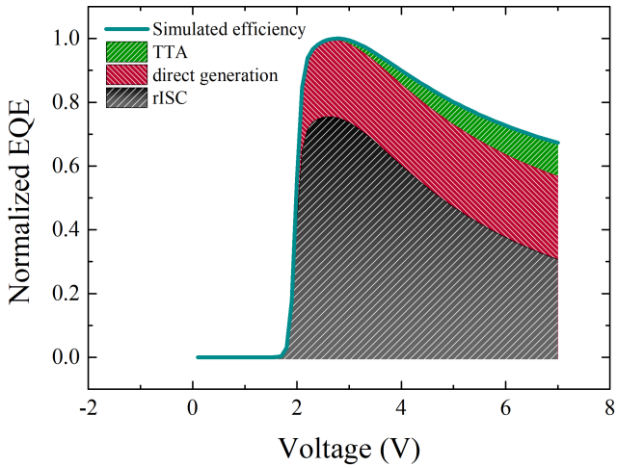

Figure 5.9: Normalized EQE versus voltage for a layer thickness of 200 nm showing the various contributions to the efficiency. This figure corresponds to the fit in figure 5.2(b) at 295 K.

In contrast to TPQ, at high current density, we see that the simulations with STA have a too strong dependence of the efficiency on voltage compared to the experiment (figure 5.8(b)). Note that we increase the STA rate constant with temperature (table 5.3) in order to improve the fit, especially in the voltages just after V_{bi}. Both TTA and STA are processes in which two excitons annihilate and to understand why they give dissimilar efficiency curves, we need to look at the fractional contributions to the efficiency in more detail. For this purpose we chose the fit from figure 5.3(b) at 295 K. Figure 5.9 shows the various contributions to the efficiency, where we take TTA to account for the roll-off. We see that just after V_{bi} the efficiency originates to a large extent from singlets that underwent rISC, whereas at higher voltages there are growing contributions from the direct generation of singlets as well as singlets coming from TTA. Disentangling the contributions to the efficiency thus explains the flattening of the efficiency curve that we observe. The loss of triplet excitons due to TTA has its effect on the efficiency in figure 5.9 implicitly via singlets coming from rISC, whose fractional contribution shrinks with increasing voltage. This highlights the importance of a fast rISC-rate once again,[44] since the mutual annihilation of triplets will be reduced if they are converted to singlets before TTA occurs. In contrast to this, STA negatively impacts the entire singlet population, meaning the direct generation of singlets as well and therefore it overestimates the roll-off at higher voltage.

5.11 Conclusions

In summary, a device model for TADF OLEDs is presented that accurately describes the dependence of the efficiency as function of voltage, temperature and layer thickness. From the efficiency roll-off at higher voltages, a triplet-triplet annihilation constant of $k_{TTA} = 7\pm3 \times 10^{-18}$ $m^3\ s^{-1}$ is determined, which agrees well with the k_{TTA} from optical measurements. However, for reliable extraction of the TTA constant it is of importance that values of $k_{(r)ISC}$ are accurately determined before as well as that the positional dependence of the exciton profile is taken into account. With our device model we are able to discriminate between different causes for the

roll-off, verifying that TTA is the dominant cause. By disentangling the various contributions to the efficiency, we elucidate why the observed voltage dependence of the roll-off cannot be due to TPQ and STA.

5.12 Experimental section

Simulation

For the theoretical *J-V* curves, our drift-diffusion simulations employ an iterative scheme to calculate the charge carrier density with a tolerance of 1×10^{-6}, i.e. both current and charge carrier density values have converged if their values between loops vary less than the said tolerance. For stability, the iterative loop is usually repeated five times and the calculated mobility values are averaged over all iterative loops. The active layer itself is simulated using 1000 points on an exponential symmetric grid, normalized to unity. The electrical bandgap of CzDBA was determined from OLED data to be 2.8 eV and the relative permittivity was set to 3.

Thin film fabrication for TrPL measurements

CzDBA was obtained from Luminescence Technology Corporation and used without further purification. Samples were prepared by evaporating 100 nm onto a quartz substrate under a base pressure of around 2×10^{-6} mbar. The sample was loaded into a home-built air-tight sample holder inside a glovebox before it was transferred out for the spectroscopic measurements.

Spectroscopic characterization

Time-resolved photoluminescence measurements were carried out using a 4Picos gated-iCCD camera (Standford Computer Optics). Samples were photoexcited at 350 nm using the output from a Ti: sapphire laser (Coherent, Astrella, 1 kHz, 5 mJ, 35 fs) paired with a commercial optical parametric amplifier (Coherent, OperA). The spectra are collected using the 4Spec software (Stanford Computer Optics) using gating times ranging exponentially from 0.5-5000 ns and spectra were recorded out to 50 µs. The photoexcitation light was focused onto the sample in order to ensure a uniform excitation density throughout the film. The spot size of 0.8 mm at the sample position was characterized using a beam profiler (Coherent, LaserCamHR-II).

For the power study, the lowest incident power was chosen to minimize annihilation processes while maintaining a good signal-to-noise ratio. We varied the power at least an order of magnitude but kept the highest power low enough that bleaching or other degradation effects of our films during the measurement would play a minor role and would not impede our analysis.

Analysis

The raw data from the 4Picos was further processed with a home-build code in order to obtain the intensity versus time plots. The initial singlet density was calculated from the absorption spectrum and the incident laser power using a reported method.[41]

References

[1] H. Uoyama, K. Goushi, K. Shizu, H. Nomura, C. Adachi, *Nature* **2012**, *492*, 234.

[2] T. Hosokai, H. Matsuzaki, H. Nakanotani, K. Tokumaru, T. Tsutsui, A. Furube, K. Nasu, H. Nomura, M. Yahiro, C. Adachi, **2017**, 1.

[3] Z. Yang, Z. Mao, Z. Xie, Y. Zhang, S. Liu, J. Zhao, J. Xu, Z. Chi, M. P. Aldred, *Chem. Soc. Rev.* **2017**, *46*, 915.

[4] Q. Zhang, B. Li, S. Huang, H. Nomura, H. Tanaka, C. Adachi, *Nat. Photonics* **2014**, *8*, 326.

[5] M. Y. Wong, E. Zysman-Colman, *Adv. Mater.* **2017**, *29*.

[6] P. W. M. Blom, N. I. Craciun, D. M. De Leeuw, G. A. H. Wetzelaer, H. T. Nicolai, M. Kuik, *Adv. Mater.* **2014**, *26*, 512.

[7] D. Abbaszadeh, A. Kunz, G. A. H. Wetzelaer, J. J. Michels, N. I. Craciun, K. Koynov, I. Lieberwirth, P. W. M. Blom, *Nat. Mater.* **2016**, *15*, 628.

[8] M. Kuik, L. J. A. Koster, A. G. Dijkstra, G. A. H. Wetzelaer, P. W. M. Blom, *Org. Electron. physics, Mater. Appl.* **2012**, *13*, 969.

[9] Q. Niu, G. J. A. H. Wetzelaer, P. W. M. Blom, N. I. Crăciun, *Adv. Electron. Mater.* **2016**, *2*, 1.

[10] N. B. Kotadiya, P. W. M. Blom, G.-J. A. H. Wetzelaer, *Nat. Photonics* **2019**, 1.

[11] B. van der Zee, Y. Li, G. J. A. H. Wetzelaer, P. W. M. Blom, *Adv. Opt. Mater.* **2021**, *n/a*, 2100249.

[12] W. F. Pasveer, J. Cottaar, C. Tanase, R. Coehoorn, P. A. Bobbert, P. W. M. Blom, M. De Leeuw, M. A. J. Michels, *Phys. Rev. Lett.* **2005**, *94*, 1.

[13] W. Liu, N. B. Kotadiya, P. W. M. Blom, G. J. A. H. Wetzelaer, D. Andrienko, *Adv. Mater. Technol.* **2020**, *2000120*, 1.

[14] N. B. Kotadiya, A. Mondal, P. W. M. M. Blom, D. Andrienko, G. J. A. H. H. Wetzelaer, *Nat. Mater.* **2019**, *18*, 1182.

[15] K. Masui, H. Nakanotani, C. Adachi, *Org. Electron. physics, Mater. Appl.* **2013**, *14*, 2721.

[16] G. Schwartz, S. Reineke, T. C. Rosenow, K. Walzer, K. Leo, *Adv. Funct. Mater.* **2009**, *19*, 1319.

[17] F. B. Dias, T. J. Penfold, A. P. Monkman, *Methods Appl. Fluoresc.* **2017**, *5*, 012001.

[18] H. Noda, X. Chen, H. Nakanotani, T. Hosokai, M. Miyajima, N. Notsuka, Y. Kashima, J. Brédas, C. Adachi, *Nat. Mater.* **2019**.

[19] T. Kobayashi, A. Niwa, K. Takaki, S. Haseyama, T. Nagase, K. Goushi, C. Adachi, H. Naito, *Phys. Rev. Appl.* **2017**, *7*, 1.

[20] N. Haase, A. Danos, C. Pflumm, A. Morherr, P. Stachelek, A. Mekic, W. Brütting, A. P. Monkman, *J. Phys. Chem. C* **2018**, *122*, 29173.

[21] P. De Silva, C. A. Kim, T. Zhu, T. Van Voorhis, *Chem. Mater.* **2019**, *31*, 6995.

[22] K. Thakur, B. van der Zee, G. J. A. H. Wetzelaer, C. Ramanan, P. W. M. Blom, *Adv. Opt. Mater.* **2022**, *10*.

[23] Y. Li, N. B. Kotadiya, B. van der Zee, P. W. M. Blom, G. J. A. H. Wetzelaer, *Adv. Opt. Mater.* **2021**, *9*, 1.

[24] G. A. H. Wetzelaer, M. Kuik, H. T. Nicolai, P. W. M. Blom, *Phys. Rev. B - Condens. Matter Mater. Phys.* **2011**, *83*, 1.

[25] B. van der Zee, Y. Li, G. J. A. H. Wetzelaer, P. W. M. Blom, *Adv. Electron. Mater.* **2022**, *8*.

[26] R. Scholz, P. Kleine, R. Lygaitis, L. Popp, S. Lenk, M. K. Etherington, A. P. Monkman, S. Reineke, *J. Phys. Chem. A* **2020**, *124*, 1535.

[27] Y. Li, L. Jiang, W. Liu, S. Xu, T. Y. Li, F. Fries, O. Zeika, Y. Zou, C. Ramanan, S. Lenk, R. Scholz, D. Andrienko, X. Feng, K. Leo, S. Reineke, *Adv. Mater.* **2021**, *33*.

[28] M. K. Etherington, N. A. Kukhta, H. F. Higginbotham, A. Danos, A. N. Bismillah, D. R. Graves, P. R. McGonigal, N. Haase, A. Morherr, A. S. Batsanov, C. Pflumm, V. Bhalla, M. R. Bryce, A. P. Monkman, *J. Phys. Chem. C* **2019**, *123*, 11109.

[29] E. Cho, M. Hong, V. Coropceanu, J. L. Brédas, *Adv. Opt. Mater.* **2021**, *9*, 1.

[30] E. W. Evans, Y. Olivier, Y. Puttisong, W. K. Myers, T. J. H. Hele, S. M. Menke, T. H. Thomas, D. Credgington, D. Beljonne, R. H. Friend, N. C. Greenham, *J. Phys. Chem. Lett.* **2018**, *9*, 4053.

[31] M. A. Baldo, C. Adachi, S. R. Forrest, *Phys. Rev. B - Condens. Matter Mater. Phys.* **2000**, *62*, 10967.

[32] C. Murawski, K. Leo, M. C. Gather, *Adv. Mater.* **2013**, *25*, 6801.

[33] S. Reineke, K. Walzer, K. Leo, *Phys. Rev. B - Condens. Matter Mater. Phys.* **2007**, *75*, 1.

[34] R. Saxena, T. Meier, S. Athanasopoulos, H. Bässler, A. Köhler, *Phys. Rev. Appl.* **2020**, *14*, 1.

[35] A. Niwa, S. Haseyama, T. Kobayashi, T. Nagase, K. Goushi, C. Adachi, H. Naito, *Appl. Phys. Lett.* **2018**, *113*.

[36] S. Reineke, G. Schwartz, K. Walzer, M. Falke, K. Leo, *Appl. Phys. Lett.* **2009**, *94*, 2007.

[37] D. Kasemann, R. Brückner, H. Fröb, K. Leo, *Phys. Rev. B - Condens. Matter Mater. Phys.* **2011**, *84*, 1.

[38] S. Sem, S. Jenatsch, K. Stavrou, A. Danos, A. P. Monkman, B. Ruhstaller, *J. Mater. Chem. C* **2022**, *10*, 4878.

[39] T.-L. Wu, M.-J. Huang, C.-C. Lin, P.-Y. Huang, T.-Y. Chou, R.-W. Chen-Cheng, H.-W. Lin, R.-S. Liu, C.-H. Cheng, *Nat. Photon.* **2018**, *12*, 235.

[40] D. E. Markov, P. W. M. Blom, *Appl. Phys. Lett.* **2005**, *87*, 1.

[41] M. Hasan, A. Shukla, V. Ahmad, J. Sobus, F. Bencheikh, S. K. M. McGregor, M. Mamada, C. Adachi, S.-C. C. Lo, E. B. Namdas, *Adv. Funct. Mater.* **2020**, *30*, 2000580.

[42] H. Nakanotani, H. Sasabe, C. Adachi, *Appl. Phys. Lett.* **2005**, *86*, 1.

[43] V. Ahmad, J. Sobus, M. Greenberg, A. Shukla, B. Philippa, A. Pivrikas, G. Vamvounis, R. White, S. C. Lo, E. B. Namdas, *Nat. Commun.* **2020**, *11*.

[44] M. Inoue, T. Serevičius, H. Nakanotani, K. Yoshida, T. Matsushima, S. Juršenas, C. Adachi, *Chem. Phys. Lett.* **2016**, *644*, 62.

Chapter details

Publications

This chapter is based on the publications:

B. van der Zee, Y. Li, G.-J. A. H. Wetzelaer, and P. W. M. Blom, Numerical device model for organic light-emitting diodes based on thermally activated delayed fluorescence, Adv. Electron. Mater. **8,** 2101261 (2021)

and

Thakur, K., van der, B., Wetzelaer, G.-J. A. H., Ramanan, C., Blom, P. W. M., Quantifying Exciton Annihilation Effects in Thermally Activated Delayed Fluorescence Materials. *Adv. Optical Mater*. 2022, 10, 2101784.

Author contributions

For the first publication:

B. v. d. Zee and Y. Li made the devices and performed the experiments. B. v. d. Zee wrote the code for the TADF device model, did the simulations and wrote the manuscript with input from the co-authors. G. A. H. Wetzelaer and P. W. M. Blom supervised the project.

For the second publication:

K. Thakur performed the photophysical experiments. B. v. d. Zee wrote software to analyse the raw data from the 4Picos setup. B. v. d. Zee wrote the simulation program to fit the TrPL data and performed the fitting together with K. Thakur. K. Thakur together with B. v. d. Zee wrote the manuscript with input from the other authors. G. A. H. Wetzelaer, C. Ramanan and P. W. M. Blom supervised the project.

Chapter 6: Degradation of Organic Light-Emitting Diodes Based on Thermally Activated Delayed Fluorescence

In this chapter we study the degradation of single-layer OLEDs based on the TADF emitter 9,10-bis(4-(9H-carbazol-9-yl)−2,6-dimethylphenyl)−9,10-diboraanthracene (CzDBA). After quantitatively describing the current-voltage (*J-V*) and efficiency curves after electrical driving, we use a numerical model to reproduce the voltage increase and light decrease during degradation. We demonstrate that the fundamental mechanism behind OLED degradation is electron and hole trap formation due to triplet-polaron annihilation (TPA), the same as reported for polymer light-emitting diodes (PLEDs). Other mechanisms such as triplet-triplet annihilation (TTA) and singlet-triplet annihilation (STA) do not match the experimental data. Understanding of the degradation mechanism allows us to predict how a broader emission zone in a thicker single-layer TADF OLED affects its lifetime, resulting in an improved stability with an LT_{80} lifetime of 1050 hours at an initial luminance of 1000 cd m^{-2}.

6.1 Introduction

As we've seen in chapter 1, TADF materials form a promising class of emitters for future display applications, however their lifetime continues to be a significant issue that hampers commercialization. Modelling of degraded PLEDs revealed that under a constant driving current, both the typical degradation characteristics of a voltage increase as well as a decrease of the light output during degradation could be linked to the formation of hole traps,[1] as was already suggested earlier.[2] In the yellow emitting polymer super-yellow poly(*p*-phenylene vinylene (SY-PPV) the dynamics of the trap formation revealed that the interaction between excitons and polarons is responsible for the creation of these degradation traps.[3] The exciton-polaron interaction correctly predicted the scaling of the formed hole trap density P_t with stress time: initially, when the amount of free holes (p) is still larger than P_t, the amount of hole traps exhibits a linear increase with time, combined with a scaling of the aging current density (J_{age}) of $J_{age}^{3/2}$. Subsequently, at later times when $P_t > p$, the hole-trap formation follows a square-root dependence with stress time, in combination with a linear dependence on J_{age}. In addition, we've seen in chapter 3 that a similar scaling on stress time and J_{age} were found in the orange/red emitting polymer poly[2-methoxy-5-(2′-ethyl-hexyloxy)-1,4-phenylenevinylene] (MEH-PPV). That study further confirmed that from the two excitonic species, triplet excitons are the ones responsible for the interaction with charges to form traps,[4] as suggested before.[5]

In contrast to PLEDs (section 1.7 and chapter 3), the main mechanism behind TADF OLED degradation is still controversial. Several strategies to enhance the lifetime of TADF OLEDs have been put forth, often revolving around device- or molecular design,[6–11] but the underlying causes of degradation are rarely quantitatively addressed. The most commonly cited responsible mechanisms that lead to TADF OLED degradation are triplet-triplet annihilation (TTA) and triplet-polaron annihilation (TPA) or a combination of both.[12–17] In a recent study, using luminescence quenching measurements TPA has been identified as a major source of degradation in TADF OLEDs.[18] Furthermore, the various degradation mechanisms in TADF OLEDs were quantitatively addressed using kinetic Monte Carlo simulations.[19] We note that both studies were carried out on multilayered OLED structures. To clarify the degradation mechanism, we study the degradation of single layer TADF OLEDs based on the model emitter 9,10-bis(4-(9H- carbazol-9-yl)−2,6-dimethylphenyl)−9,10-diboraanthracene (CzDBA).[20] After modelling of the undegraded CzDBA OLEDs with a numerical drift-diffusion simulator, from which we've seen in chapters 4 and 5 that TTA is the dominant roll-off mechanism,[21,22] we quantitatively explain the current-voltage (*J-V*) and efficiency curves after degradation. Due to balanced transport, the degraded OLED data is consistent with the formation of both hole and electron traps. The scaling of these traps with time and aging current are consistent with TPA as trap formation mechanism. Here, a polaron absorbs the energy of a triplet exciton, thereby promoting the polaron to a higher excited state, whereas the triplet gets demoted to the ground state. The energetic polaron then has the ability to break specific bonds in the molecule, fragmenting it. The fragmented products have been reported to react further to form traps.[23] Other trap formation mechanisms, such as TTA and STA, cannot reproduce the experimental characteristics of the degraded OLEDs. Moreover, the interaction coefficient for TPA leading to degradation traps is found to be almost the same to the coefficient found in PLEDs, displaying the universality of the degradation mechanism across various types of OLEDs. Following the

predictions of the degradation model, we experimentally confirm that increasing the OLED thickness results in reduced triplet-polaron interactions, increasing the LT_{80} lifetime up to 1050 hours at an initial luminance of 1000 cd/m^2. This lifetime of a single layer TADF OLED stands out even among reported lifetimes of multilayer devices.

6.2 Modelling degraded CzDBA OLEDs

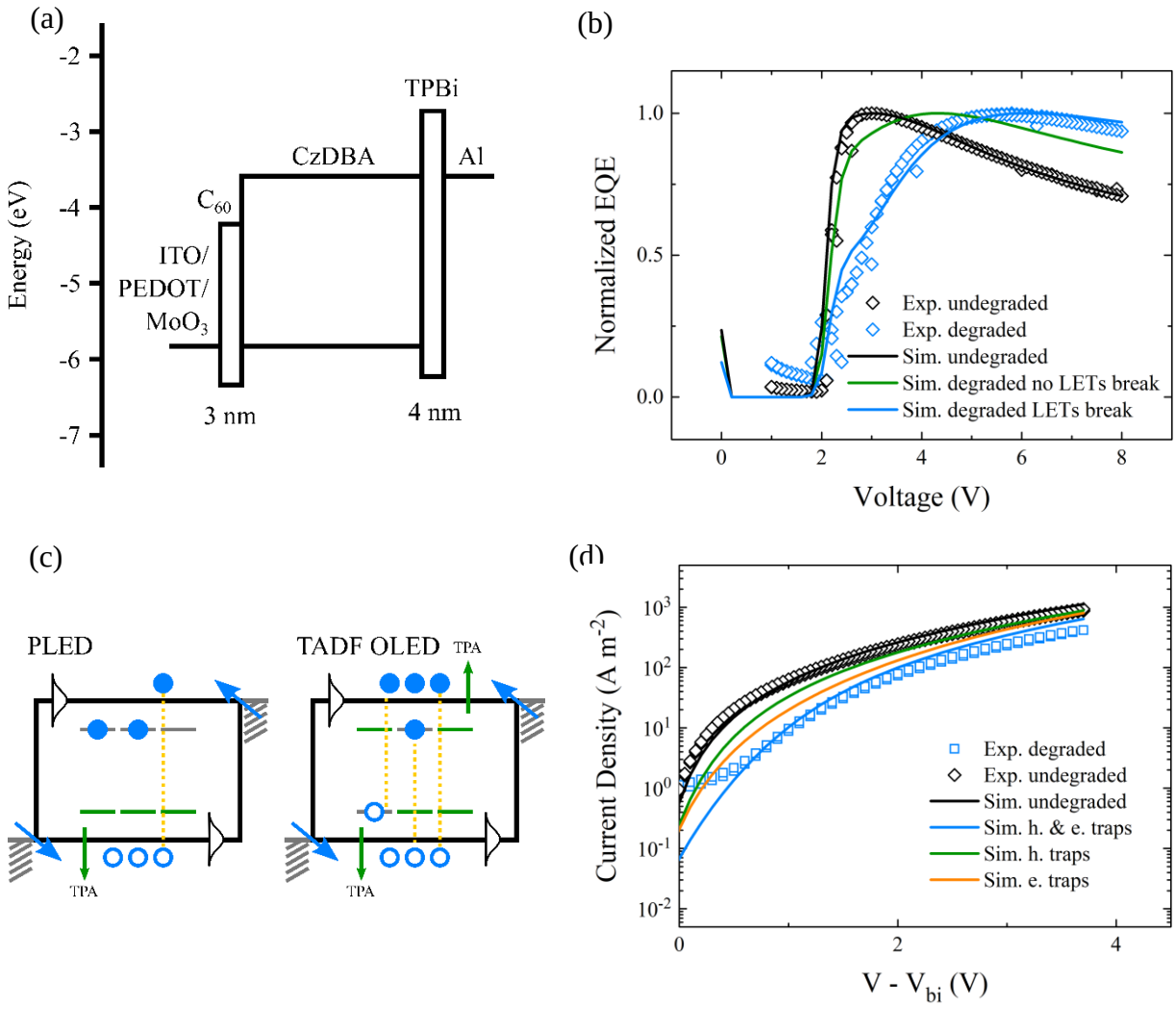

Figure 6.1: Device structure, energy diagram and electrical characteristics of pristine and degraded CzDBA OLEDs. (a) device structure and energy diagram of CzDBA OLEDs. (b) Normalized experimental (Exp.) EQE as function of voltage for an OLED with a 300 nm CzDBA layer, accompanied by simulations (Sim.) that show the effect of light-emitting traps (LETs) becoming nonradiative after degradation. (c) Schematic representation of the TPA process in a PLED (left) and TADF OLED (right). The blue solid and empty circles represent holes and electrons respectively, which are residing either in the HOMO/LUMO (indicated with a Gaussian DOS) or in the trap states before degradation (grey energy levels). Injection is represented by the blue arrows and recombination by the yellow dotted lines. TPA generates

the trap states during degradation, which are indicated by the green energy levels. (d) *J-V* characteristics (corrected for V_{bi}) of a 140 nm CzDBA OLED both undegraded and degraded (symbols) accompanied by simulations (lines)

The device structure of the single-layer CzDBA OLED device is presented in figure 6.1(a). In this device, a neat film of the TADF emitter CzDBA is sandwiched between two electrodes, without charge-transport or blocking layers. As a starting point we model the undegraded 300 nm CzDBA OLED with the device model that was outlined in chapter 5. Similar as the earlier reported results,[22] also the undegraded OLEDs used in the present study show a fast initial increase in efficiency above the built-in voltage (V_{bi}), as shown in figure 6.1(b) (black symbols), this being one of the fingerprints of emissive trap states. Together with the inclusion of TTA the voltage dependence of the EQE of a 300 nm TADF OLED is quantitatively well described (figure 6.1(b), black line). For completeness I mention here that the simulation parameters that lead to the fit of the undegraded device are given in chapter 5, table 5.1 and 5.2.

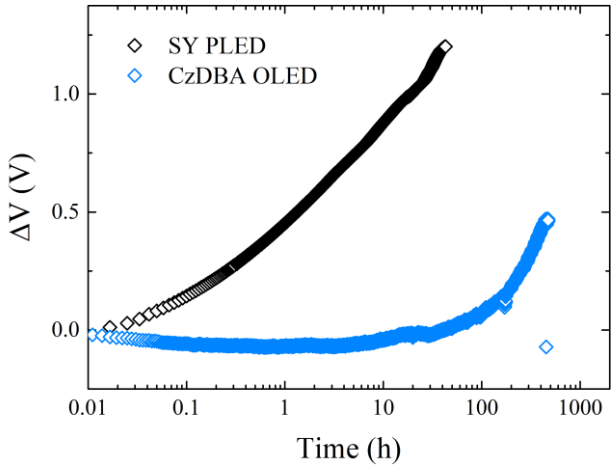

Figure 6.2 Voltage increase versus time for a typical Super Yellow and a CzDBA TADF OLED aged at 10 and 20 mA cm^{-2} respectively.

A fundamental question is whether the conclusions from degradation studies on PLEDs, namely hole trap formation by triplet-polaron annihilation, also applies to TADF OLEDs. When comparing the voltage increase (ΔV) of PLEDs and TADF OLEDs (figure 6.2), we observe that they display different behaviour: whereas PLEDs exhibit a fast initial voltage increase, which slows down in time, TADF OLEDs have in contrast a very weak voltage increase in the first few hours, followed by a sharp rise at a certain point in time. One fundamental difference between a SY-PPV PLED and CzDBA OLED is that in pristine SY-PPV the hole current is several orders of magnitude higher than the electron current, since electron traps are present with a density of around 1-3 × 10^{23} m^{-3},[24] already before degradation. As schematically indicated in figure 6.1(c) (left), the free electron concentration is strongly reduced, since most electrons reside in a trap. For CzDBA both the electron and hole current are nearly trap free, meaning that the concentration of free electrons and holes is much larger and nearly equal. The trap formation originating from the interaction between free charge carriers and triplet excitons in both materials possesses significantly different effects on the device performance during the degradation. In a PLED, due to the much higher concentration of holes than electrons in a pristine device, mainly hole traps would be formed in the first place. The low concentration of

free electrons would strongly limit the formation of electron traps. Consequently, the small amount of electron traps generated during aging is negligible as compared to the extrinsic electron traps already present in a pristine device. The dominance of hole-trap generation during PLED degradation was also found experimentally.[1] In contrast, in CzDBA the electron and hole trap formation is expected to be equally strong, as schematically indicated in figure 6.1(c) (right)**.** Formation of both electron and hole traps can be confirmed by modelling of the *J-V* characteristics of a CzDBA OLED after degradation. As shown in figure 6.1(d), good agreement between the experimental and modelled *J-V* characteristics of a 140 nm degraded CzDBA OLED is only obtained when both hole and electron traps are present. To illustrate the effect of electron and hole trapping on the OLED current, we consider the effect of homogeneously distributed hole *and* electron traps in the CzDBA layer with a similar concentration of 1.2×10^{23} m^{-3}, respectively (see figure 6.1(d), blue line). For comparison, merely hole (figure 6.1(d), green line) or electron traps (figure 6.1(d), orange line) with a density of 2.4×10^{23} m^{-3} cannot model the *J-V* curves after degradation. When only considering the effect of a single type of traps (either hole or electron traps), the modelled current density is comparable to the pristine device, higher than the experimental aged one. This can be explained by the fact that both electron and hole transport are nearly trap-free in the pristine device, trapping of just one type of carrier does not sufficiently impact the current density, as the other trap-free charge carrier quickly dominates the total current. Therefore, trapping of both electrons and holes is required to explain the degraded *J-V*, which is thus a consequence of the balanced bipolar transport. The fact that the formation of traps correlates with the presence of free polarons is a first indication that degradation is governed by TPA.

A second fundamental difference between a SY-PPV PLED and CzDBA OLED is that in the PLED the light emission solely comes from bimolecular Langevin recombination between free electrons and holes. Trap-assisted recombination via extrinsic traps present in pristine devices is of non-radiative nature. In contrast, trap-assisted recombination from the low amount of traps present in unaged CzDBA OLEDs is radiative, dominating the light emission at low voltages as we've seen in section 5.4. In case that degradation processes that involve excitons, such as TPA, result in the breaking of chemical bonds, also the light-emitting traps (LETs) will be destroyed and converted into non-radiative degradation traps. Here, we have to take into account that the number of LETs is limited (~10^{22} m^{-3}).

We include the conversion of a LET into a non-radiative trap in our model when calculating the SRH recombination (R_{SRH}). Initially, in the undegraded state, all traps are emissive, resulting in a high internal quantum efficiency.[22] The trap density N_{to}, is obtained from the analysis of CzDBA electron- and hole-only devices. We note that N_{to} is time- and position independent. During degradation, the radiative recombination on LETs (R_{LET}) is reduced by the density of LETs that are converted to non-radiative dark traps (N_{DT}), which grows in time during the degradation experiment:

$$R_{LET}[x,t] = R_{SRH\_0}[x] - \frac{N_{DT}[x,t]}{N_{t0}} R_{SRH\_0}[x]. \quad (6.1)$$

Here, $N_{DT}[x,t]/N_{t0}$ represents the local fraction of traps that is converted from radiative to non-radiative, whereas (1- $N_{DT}[x,t]/N_{t0}$) is the local fraction of traps that still emits light. R_{SRH_0}

represents the initial SRH recombination rate when all traps are still emissive in the undegraded state. Quantities with [x] are taken as position-dependent quantities and [t] as time-dependent quantities. We note that $R_{SRH\_0}[x]$ depends on position since the densities of free and trapped electrons and holes are position dependent. At the moment that all initially emissive traps N_{t0} are converted to dark traps N_{DT}, eq. (6.1) ensures that the contribution of the LETs to the total light-output of the OLED goes to zero. By decreasing the LET recombination with the traps obtained from the *EQE-V*, as shown in figure 6.1(c)**,** good agreement between modelling and experimental results can be reached. In case that all LETs remain intact upon degradation, the modelled efficiency rises too fast (green line), due to (emissive) trap-assisted recombination being dominant at low voltages.

6.3 Extracting the trap formation mechanism

As a next step, the voltage and light output versus aging time under current stress is discussed. During the aging tests, the OLEDs were kept at a constant current density, the aging current, while simultaneously the voltage and light output were monitored. To extract the trap-formation mechanism during degradation we model the voltage increase with the same drift-diffusion approach explained above. For an accurate description, it is important to take the formation of both hole and electron traps as well as the breaking of LETs into account, and we will now outline how this is done for the degradation simulations. In our previous study on the degradation of PLEDs,[3] it was assumed that traps generated during degradation would be homogeneously distributed over the active layer. With this assumption, the voltage increase in time could be modelled and described as an increase of formed traps in time. From the observed dynamics of trap formation, it was then concluded that hole trap formation via TPA was the dominant mechanism.[3] As a refinement, in the present study, both hole and electron traps generated during ageing are now modelled as a function of position. This is rationalized by the non-uniform distribution of charge-carrier and exciton densities throughout the emissive layer in working OLEDs. In this way, for every degradation mechanism we can model the voltage increase during aging and compare that with experimental results. The modelled voltage versus time is therefore dependent on different models, i.e., different physical mechanisms to simulate trap formation.

As a first step, we take the local product of charge carriers and triplet excitons to simulate the local trap formation via TPA. The hole trap density (P_t in [m^{-3}]) (in case of TPA) for a given time step (t_{step}) is then given by:

$$P_t[x] = \kappa * p[x] * T[x] * t_{step}. \tag{6.2}$$

With κ [$m^3\ s^{-1}$] the interaction parameter between the triplet density T [m^{-3}] and the hole density p [m^{-3}]. An analogous equation is used for electrons with the same value of κ. All quantities that are considered position dependent inside the device are denoted by [x]. The interaction coefficient in eq. (6.2) controls the trap formation rate, which can be treated as a fitting parameter for different experimental aging currents. We note that the assumption of using an equal value of κ for electrons and holes is supported by the fact that we need (nearly) equal

amount of electron and hole traps formed after degradation to describe the *J-V* characteristics of degraded OLEDs, as shown in figure 6.1(b). If the κ values would strongly deviate, meaning either electron or hole traps would be preferentially formed, the current would be dominated by the nearly trap-free transport of the unaffected carrier, which does not match the experiment. In order to limit the number of fit parameters we find it reasonable to assume that $\kappa_p = \kappa_n$ can be used as a first approximation, although we cannot rule out the possibility that they might slightly differ in reality. Here we also take into account that triplets quenched via TPA to form a degradation trap or break a LET do not participate in the efficiency roll-off through TTA. For alternative degradation mechanisms such as TTA or STA, *p[x]* in eq. (6.2) is replaced by *T[x]* or *S[x]* respectively.

We will now turn our attention to the destruction of LETs during degradation. We note that there are two degradation processes taking place that affect the efficiency of the OLED. In one process, similar to a PLED, a free carrier absorbs the energy of a triplet exciton formed by Langevin recombination, leading to the formation of new dark degradation traps by fragmentation of the CzDBA molecules. Next to this, LETs consisting of aggregated or dimerized species of the CzDBA molecules,[25] are converted into dark traps by breaking of their chemical bonds via an interaction of triplets residing on these species with free carriers. The respective trap formation rates of each process depend on the ratio of the recombination rate of LETs (R_{LET}) versus normal Langevin recombination rate (R_{Lan}). This ratio namely represents the proportion of triplet excitons residing on a trap vs regular 'free' triplet excitons. The drift-diffusion simulations can be used to model the recombination strength at the sites of emissive traps via SRH and bimolecular Langevin recombination, from which we define the ratio of the emissive SRH recombination rate via LETs (R_{LET}) to the total recombination rate as $\alpha = R_{LET}/(R_{LET} + R_{Lan})$. We then scale the formed trap density for each time step (eq. (6.2)) such that $\alpha * P_t$ destroys LETs, whereas $(1-\alpha) * P_t$ is the amount of 'regular' degradation traps created. In time, the broken LETs reduce the emissive SRH recombination according to eq. (6.1).

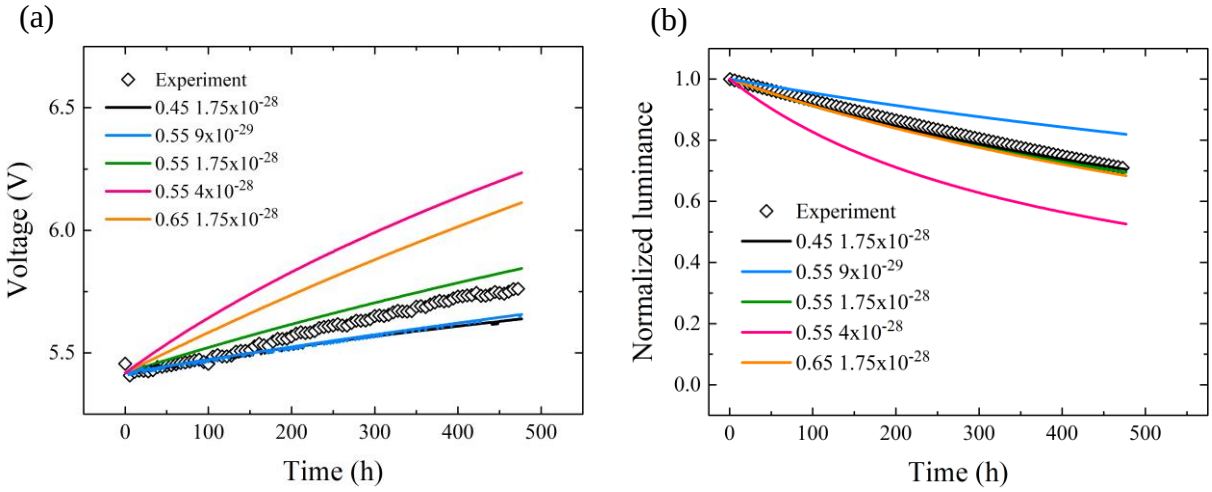

Figure 6.3: (a) Voltage versus time and (b) normalized luminance versus time for a 300 nm CzDBA OLED aged at 10 mA cm^{-2} (symbols). In the legend, first the trap depths are given in eV, followed by the value of κ [m^3 s^{-1}].

After explaining the basic idea about different models for describing the trap generation, we now simulate the trap formation via the mechanism of TPA. The calculated voltage rise as a function of aging time is influenced by the value of κ as well as the trap depth of the degradation traps. Figure 6.3(a) shows the interplay between the two, where it becomes clear that higher trap depths cause a larger voltage increase for the same interaction coefficient. In figure 6.3(b) we see that the different trap depths show no large influence on the light output *for the same value* of κ. However, the overshooting voltage should be corrected by lowering κ until it fits the voltage increase, which we can do for each trap depth. The situation will then be such that deeper traps need a lower κ to fit the experiment, meaning that the less degradation traps are generated, the deeper the degradation trap is. Consequently, *for different values of* κ the simulated light output will move upwards with increasing trap depth. By considering both the voltage increase as well as the light output, a unique combination of the trap depth and κ can be found.

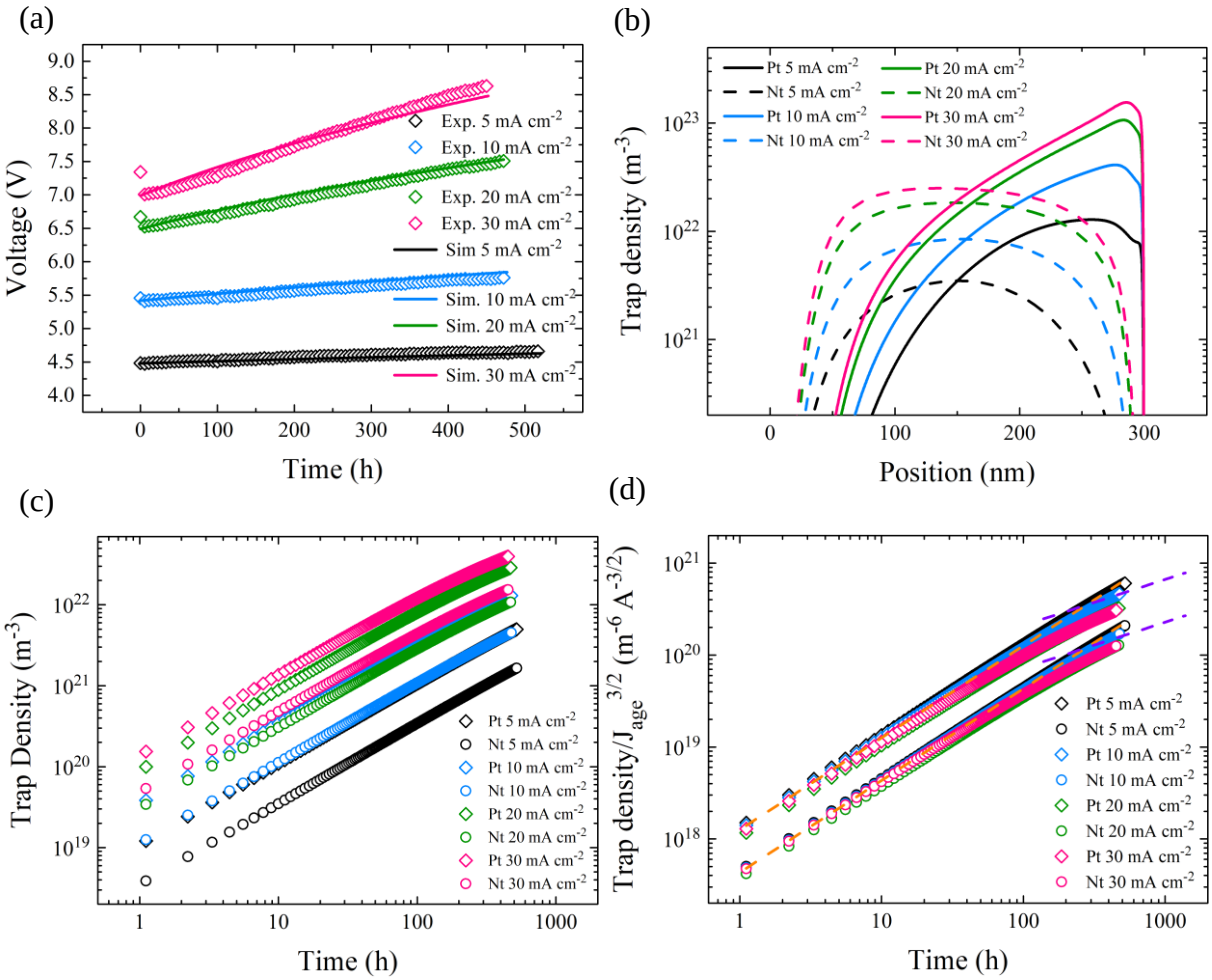

Figure 6.4: Ageing behavior of CzDBA OLEDs. Ageing behavior of 300 nm CzDBA OLEDs, modelled with the TPA mechanism. (a) driving voltage versus time under constant current density, where the experiments (Exp.) in symbols are complimented by simulations (Sim.). (b) Trap density versus distance to the cathode in the device for all values of J_{age} (5-30 mA cm^{-2}) at the end of the aging test. (c) The extracted hole (h.) and electron (e.) trap density versus aging time. (d) The trap density scaled with $J_{age}^{3/2}$. The dashed orange and violet lines have a slope of

1 and 0.5 respectively as a guide to the eye. Note that the experimental time step is 10 seconds, but for readability several points were skipped between the data points shown here.

The modelling of the voltage in time can be seen in figure 6.4(a) for four different values of J_{age}, where we achieve a good fit with a degradation trap depth of 0.55 eV and $\kappa = 1.75 \times 10^{-28}$ m^3 s^{-1}. The same combination of trap depth and κ describe the degradation of the 140 nm OLED.[26] This is a strong indication that TPA is responsible for device degradation. To our knowledge, this is the first time the interaction coefficient between triplets and charge carriers that leads to trap formation has been reported for TADF OLEDs. By kinetic Monte Carlo simulations on TADF multilayer OLEDs Hauenstein et al. reported an annihilation rate per site in the range 10^{-2} to 1 as function of position in the emissive layer,[19] which in combination with a site density of 10^{27} m^{-3} would translate in an interaction parameter in the 10^{-29} to 10^{-27} m^3 s^{-1} range, similar to what we have found.

At the end of the degradation tests, the position dependent trap profiles are plotted in figure 6.4(b), where the trap distribution can clearly be seen. The hole trap density peaks near the anode, while electron traps are more homogenously distributed, with a slight increase in trap density towards the cathode at higher aging currents. The average trap density within these profiles versus time is shown in figure 6.4(c). The number of generated trap density stays low, below 1×10^{22} m^{-3} at early times. It is known that such a low trap density does not impact the *J-V* characteristics at room temperature,[3] consequently we see an almost flat voltage curve at early times, as shown in figure 6.4(a) and figure 6.2. Only when the trap density exceeds 1×10^{22} m^{-3}, for example around 30 hours for J_{age} = 30 mA cm^{-2}, the voltage rise starts to become experimentally significant. In figure 6.4(d) we plot all created defects (both broken LETs and degradation traps) with their $J_{age}^{3/2}$-scaling, which causes the curves for P_t and N_t to collapse on a single curve, consistent with the TPA mechanism.[3,4] Also consistent with TPA is the linear dependence on the stress time at early times, as indicated by the dashed orange line. The square root dependence (dashed violet line) at longer aging times is not reached for most aging currents, except for the highest aging current of 30 mA cm^{-2} and only later during the degradation, where the trap density starts to pass the free carrier density.

6.4 Other degradation mechanisms

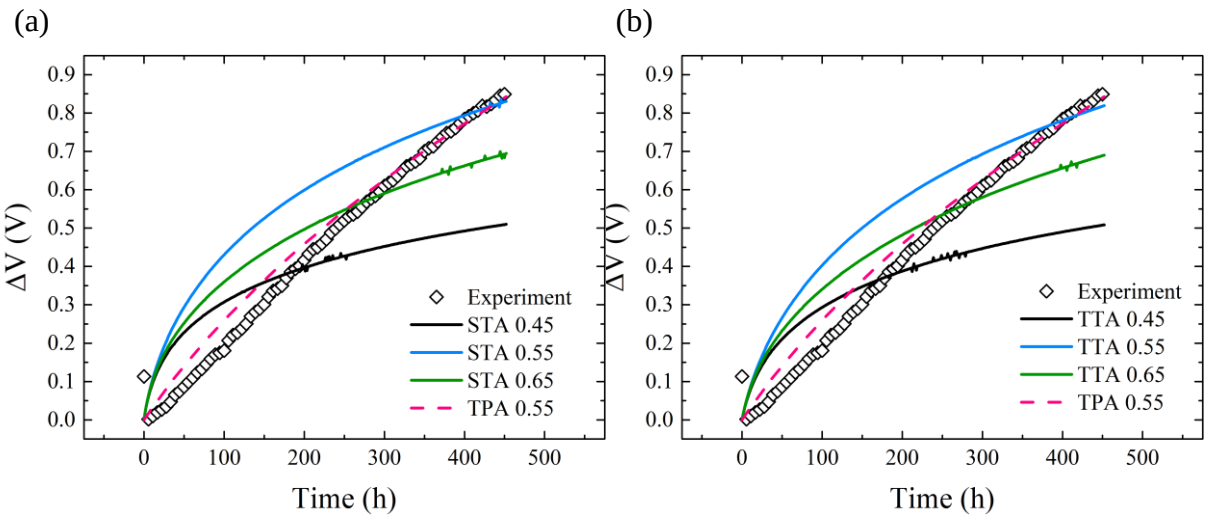

Figure 6.5: Voltage increase over time during current stress. ΔV versus time for a 140 nm OLED aged at J_{age} = 30 mA cm^{-2}. The lines show the simulated voltage increase predicted from the trap formation based on (a) STA and (b) TTA. The colours correspond to different trap depths (in eV), as written in the legend. The interaction coefficient for the different trap depths was kept constant at 6x10^{-26} m^3 s^{-1} for STA and 1.8x10^{-27} m^3 s^{-1} for TTA. Note that the experimental time step is 10 seconds, but for readability several points were skipped between the data points shown here. As a comparison the results from the TPA model is shown as a dashed pink line.

To rule out other possible degradation mechanisms we tested how the voltage will increase if traps are created via TTA or STA. As seen in figure 6.5, both do not match the shape of the experimental voltage increase, plotted here for 30 mA cm^{-2}. Here, the increase of voltage is steep at the beginning and then saturates too strongly at later times, largely deviating from the experimental results. It should be noted that such a strong saturation is a universal consequence from the STA or TTA model, since trap formation through TTA or STA depends on the product of the emissive species, while in the case of TPA it depends only linearly on the triplet concentration. In a continuous cycle, the non-radiative SRH recombination from the created degradation traps will reduce the singlet density *S* and triplet density *T*, which in turn slows the trap formation down. In STA/TTA this affects both constituents of the process, whereas in TPA only the triplets are affected. The outcome being, that for STA and TTA the voltage increase saturates too quickly as compared to the experiment. These results furthermore confirm the dominance of TPA as the main mechanism of TADF OLED degradation.

6.5 Comparing PLED and TADF OLED degradation

As mentioned, we find the parameter κ governing the interaction between charge carriers and triplet excitons to be around 1.75x10^{-28} m^3 s^{-1} for every aging current density. To compare this number with the interaction parameter found previously for PLEDs, the κ from this work needs to be multiplied with the effective triplet lifetime of 4.5 µs.[20] For PLEDs we find a proportionality constant of trap formation of around 2x10^{-33} m^3, whereas the value for TADF is around 8x10^{-34} m^3. Remarkably, these two values are very close, differing only a factor of

2.5, indicating that the intrinsic degradation mechanism, breaking of bonds by excited charge carries, is not different. With nearly equal interaction strength it also follows why in a CzDBA OLED the voltage increase and trap formation is much slower as compared to a SY-PPV PLED (figure 6.2): In PLEDs triplet excitons have a lifetime of ~100 µs,[9] resulting in a large build-up of triplets in steady-state operation. In contrast, in CzDBA the effective triplet lifetime is only around 4 µs due to efficient rISC. In CzDBA OLEDs the build-up of triplets under steady-state operation is thus much smaller and consequently, with similar interaction parameter the amount of interactions and thus the formed trap density is much less. This underlines the pivotal role of rISC in the context of OLED lifetime.

6.6 Quantitative modelling of degraded OLEDs

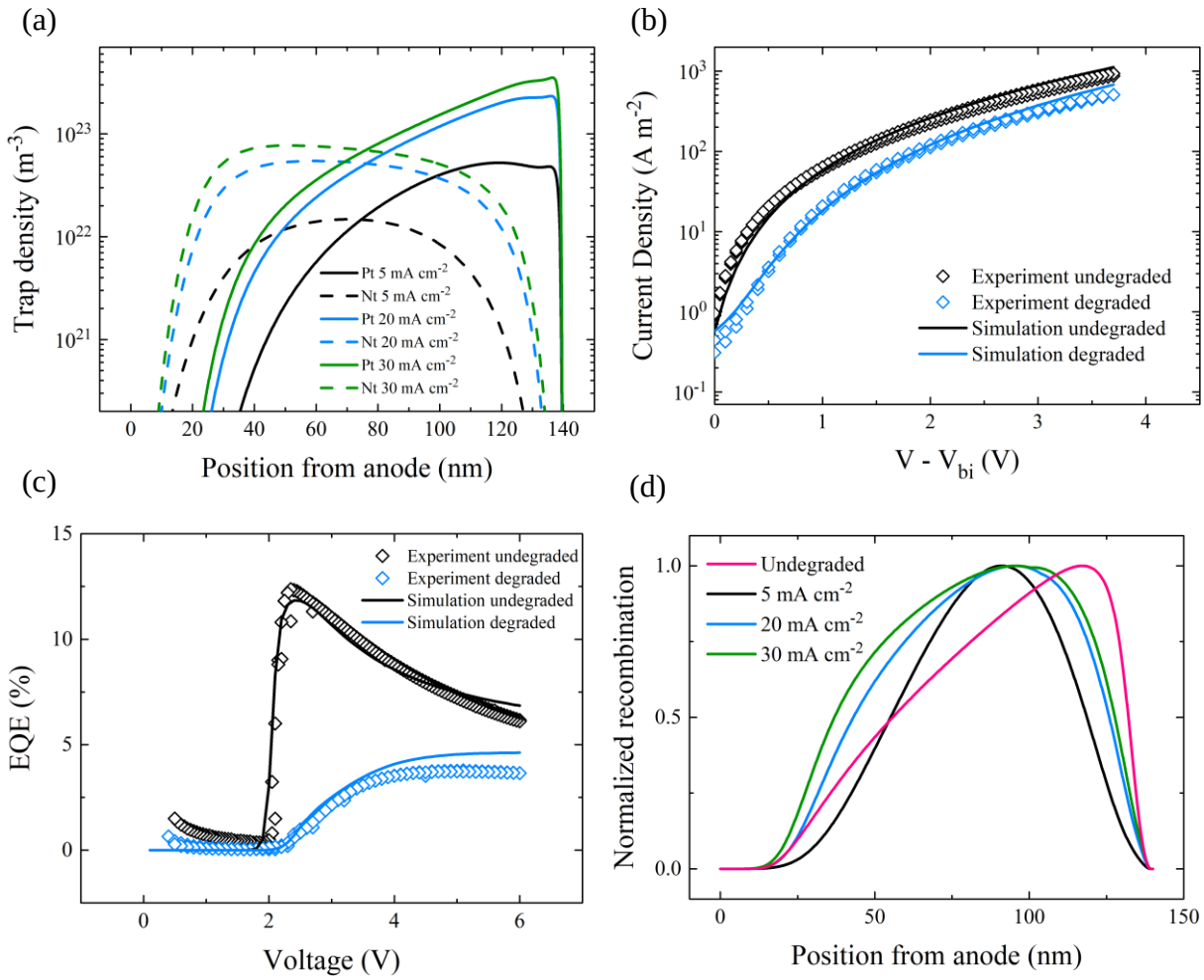

Figure 6.6: Current and EQE vs voltage for pristine and degraded 140 nm OLEDs. (a) Position dependent trap profiles for various aging current densities. (b) *J-V* (corrected for V_{bi}) and (c) EQE of (un)degraded OLEDs (symbols) complemented by simulations (lines) (J_{age} =20 mA/cm^2). The position dependent trap profiles in (a) are taken as input for the simulations in (b) & (c). (d) the recombination zone after aging for various aging current densities.

With the degradation in time modelled we can move back to the *J-V* and absolute efficiency curves after degradation with a quantitative approach. The trap profiles for the 140 nm OLEDs are shown in figure 6.6(a). For quantitative modelling we can use these trap profiles as an input, in order to predict the *J-V* and efficiency after degradation. Position averaged values are often considered in OLED modelling as an approximation, but the advantage of such a position dependent approach is that it is ultimately more realistic. In thin emissive layers neglecting the position dependence might be valid,[27] however, earlier modeling on undegraded CzDBA OLEDs with thicker emission zones revealed that neglecting the position dependence lead to inconsistencies in the values of k_{TTA} with varying temperature.[22] As shown in figure 6.6(b) and (c) the resulting simulations are able to consistently describe the *J-V* and *EQE-V* characteristics after degradation well, considering these are predictions, not fits. We would like to underline the noticeable difference between undegraded and degraded samples in terms of roll-off, which depends strongly on the number of triplets in the active layer. The additional SRH recombination from the degradation traps and the breaking of LETs removes triplets, therefore competing with other triplet decay channels such as TTA that is responsible for the roll-off.[22] As a result the degraded efficiency curves will have less roll-off and look more like PLED efficiency curves instead, where roll-off is also absent due to the dark nature of triplet states. Figure 6.6(d) shows the effect of degradation traps on the recombination profile inside the device. We also plotted the undegraded profile to show that the maximum of the recombination zone is pulled slightly towards the center of the device, a consequence of the creation of hole as well as electron traps.

6.7 Lifetime enhancement strategies

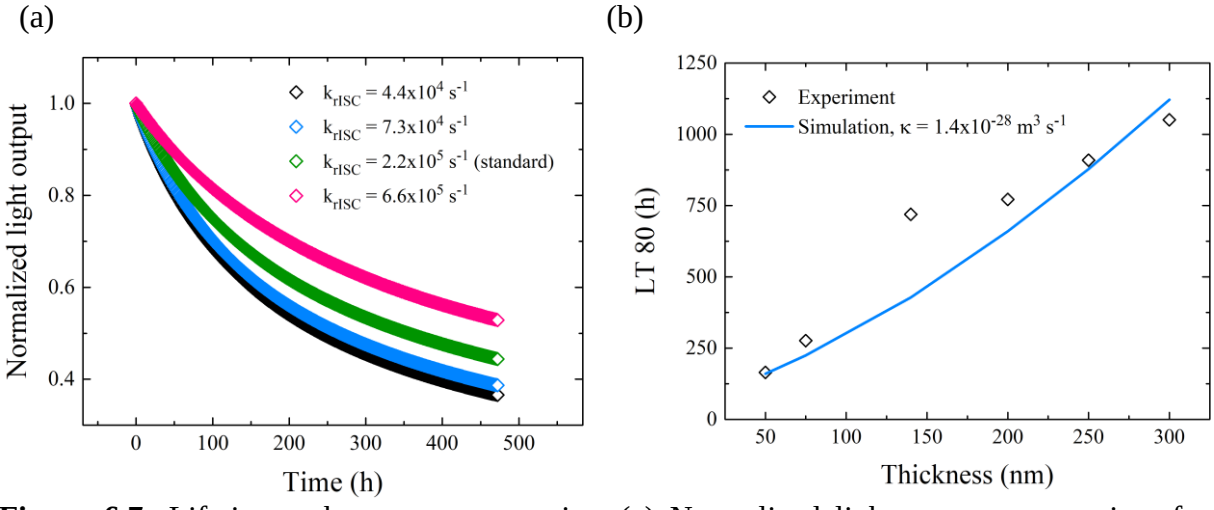

Figure 6.7: Lifetime enhancement strategies. (a) Normalized light output versus time for different simulated values of k_{rISC}. The indication of 'standard' means this value of k_{rISC} is used throughout the simulations. (b) LT_{80} versus active layer thickness for CzDBA OLEDs.

Our numerical model can now quantitatively predict several scenarios that lead to a lifetime enhancement. The first strategy that is often mentioned is increasing the value of k_{rISC}, as this will lower the triplet population and thus the TPA interaction.[28] Figure 6.7(a) shows that increasing k_{rISC} from the standard value by a factor of 3 leads to an increase in LT_{50} (time it

takes to reach 50% of the initial luminance) of about 1.5 times, whereas lowering k_{rISC} indeed worsens the lifetime. Unfortunately, many variables go into the molecular design of TADF emitters. Enhancing k_{rISC} without affecting properties like charge transport is not straightforward, although promising efforts have been made through attaching multiple electron donating units to a donor-acceptor type TADF system.[29] As expected, the calculated lifetime is improved through the enhancement in k_{rSIC}.

As reported before,[7,30,31] controlling the distribution of triplets and carriers inside the active layer is another way to mitigate their interaction that leads to trap formation. The lifetime has the potential to be enhanced through broadening the recombination zone. This allows us to formulate a rather straightforward strategy to achieve a higher lifetime, namely, to make a device with a thicker emissive layer, something that does not require additional molecular design. As a last point of discussion we will quantitatively address the influence of the active layer thickness on the OLED lifetime. For this purpose, we consider the LT_{80} lifetime at an initial luminescence of 1000 cd m^{-2}: the time it takes to reach 80% of the initial luminance. Using the experimentally obtained HO and EO parameters and $\kappa = 1.4 \times 10^{-28}$ m^3 s^{-1}, we predict the LT_{80} values for CzDBA layer thicknesses ranging from 50 to 300 nm. The theoretical curve from the TPA degradation mechanism is shown in figure 6.7(b) and the experimental LT_{80} lifetime for different thicknesses is well matched. The fact that we see a lifetime variation with thickness in the first place proves that the degradation of our CzDBA OLEDs is an effect that comes from the bulk, as injection related effects will not show a thickness dependent lifetime.[28] The thick 300 nm OLED achieves a record stability of 1050 h for LT_{80}, to our knowledge an unprecedented number for the lifetime of single layer TADF OLEDs, even exceeding many of the lifetimes reported for multilayer OLEDs.[17,20,32] Our results correspond to a LT_{95} of about 200hrs, which, however, it is still an order of magnitude below the present record for TADF OLEDS, namely a LT_{95} lifetime of 4500hrs, recently reported for a multilayer architecture,[33] with a different emitter, however.

6.8 Conclusions

In conclusion, we have quantitatively described the degradation of OLEDs based on the TADF emitter CzDBA. We use a position-dependent model where we incorporate the degradation-induced formation of both hole and electron traps by means of TPA, with the consideration of the disabling of emissive trap states. The model accurately describes the *J-V* and efficiency-voltage characteristics after degradation as well as the voltage and light output versus time under current stress. Despite the observed aging behavior between PLEDs and TADF OLEDs, we demonstrate that they both exhibit the same degradation mechanism resulting from TPA dominated trap formation, in agreement with recent findings on multi-layer TADF OLEDs.[19] Other mechanisms like TTA and STA fail to describe the degradation curves under current stress. Finally, we demonstrated that strategies which reduce the triplet concentration in the steady state, either by enhancing k_{rISC} or broadening the recombination zone, can significantly elongate the operation stability. Thick single-layer OLEDs with a broadened emission zone can reach an LT_{80} of 1050 h at an initial luminescence of 1000 cd m^{-2}.

6.9 Experimental section

Materials

CzDBA was obtained from Luminescence Technology Corporation and used without further purification.

Simulation

Our drift-diffusion simulations use an iterative scheme to calculate *n* and *p* with a tolerance of $1x10^{-6}$ on an active layer that contains 1000 points on an exponential symmetric grid normalized to unity. The simulation parameters for an undegraded device are given in table 5.1 and 5.2 of the supplementary information. Further notable input parameters include the electrical bandgap of CzDBA, which was determined from OLED data to be 2.8 eV, and the relative permittivity, which was set to 3. Both current and charge carrier density values have converged if their values between loops vary less than the said tolerance. For stability, the iterative loop is usually repeated five times and the calculated mobility values are averaged over all iterative loops. Once convergence is reached, the SRH and Langevin recombination rate are combined into the generation rate in order to take the effect of LETs into account. The singlet and triplet populations are then calculated according to their formula documented in chapter 5, taking the effect of TTA into account. The simulation for the degradation characteristics in time uses the same procedure as above, but done for each time step, which is generally kept at 4000 s. As stated in the manuscript, at the end of each time-loop the formed degradation traps as well as how many LETs are broken are calculated according to equation (6.2).

References

[1] Q. Niu, G. J. A. H. Wetzelaer, P. W. M. Blom, N. I. Crăciun, *Adv. Electron. Mater.* **2016**, *2*, 1.

[2] G. C. M. Silvestre, M. T. Johnson, A. Giraldo, J. M. Shannon, *Appl. Phys. Lett.* **2001**, *78*, 1619.

[3] Q. Niu, R. Rohloff, G. A. H. Wetzelaer, P. W. M. Blom, N. I. Crăciun, *Nat. Mater.* **2018**, *17*, 557.

[4] B. vander Zee, S. Paulus, R. Q. Png, P. K. H. Ho, L. L. Chua, G. J. A. H. Wetzelaer, P. W. M. Blom, *Adv. Electron. Mater.* **2020**, *6*.

[5] O. Pekkola, A. Gassmann, F. Etzold, F. Laquai, H. Von Seggern, *Phys. Status Solidi Appl. Mater. Sci.* **2014**, *211*, 2035.

[6] D. Zhang, M. Cai, Y. Zhang, D. Zhang, L. Duan, *Mater. Horizons* **2016**, *3*, 145.

[7] L. S. Cui, S. Bin Ruan, F. Bencheikh, R. Nagata, L. Zhang, K. Inada, H. Nakanotani, L. S. Liao, C. Adachi, *Nat. Commun.* **2017**, *8*, 1.

[8] I. Rörich, A. K. Schönbein, D. K. Mangalore, A. Halda Ribeiro, C. Kasparek, C. Bauer, N. I. Crăciun, P. W. M. Blom, C. Ramanan, *J. Mater. Chem. C* **2018**, *6*, 10569.

[9] A. S. Dhoot, D. S. Ginger, D. Beljonne, Z. Shuai, N. C. Greenham, *Chem. Phys. Lett.* **2002**, *360*, 195.

[10] D. P. K. Tsang, C. Adachi, *Sci. Rep.* **2016**, *6*, 1.

[11] S. Kothavale, W. J. Chung, J. Y. Lee, *J. Mater. Chem. C* **2021**, *9*, 528.

[12] Y. J. Cho, S. K. Jeon, J. Y. Lee, *Adv. Opt. Mater.* **2016**, *4*, 688.

[13] M. Kim, S. K. Jeon, S. H. Hwang, J. Y. Lee, *Adv. Mater.* **2015**, *27*, 2515.

[14] S. Scholz, D. Kondakov, B. Lüssem, K. Leo, *Chem. Rev.* **2015**, *115*, 8449.

[15] J. Lee, C. Jeong, T. Batagoda, C. Coburn, M. E. Thompson, S. R. Forrest, *Nat. Commun.* **2017**, *8*, 1.

[16] M. Tanaka, R. Nagata, H. Nakanotani, C. Adachi, *Commun. Mater.* **2020**, *1*, 1.

[17] C. Y. Chan, M. Tanaka, H. Nakanotani, C. Adachi, *Nat. Commun.* **2018**, *9*, 2.

[18] M. Hasan, S. Saggar, A. Shukla, F. Bencheikh, J. Sobus, S. K. M. McGregor, C. Adachi, S. C. Lo, E. B. Namdas, *Nat. Commun.* **2022**, *13*, 1.

[19] C. Hauenstein, S. Gottardi, E. Torun, R. Coehoorn, H. van Eersel, *Front. Chem.* **2022**, *9*, 1.

[20] T.-L. Wu, M.-J. Huang, C.-C. Lin, P.-Y. Huang, T.-Y. Chou, R.-W. Chen-Cheng, H.-W.

Lin, R.-S. Liu, C.-H. Cheng, *Nat. Photon.* **2018**, *12*, 235.

[21] B. van der Zee, Y. Li, G. J. A. H. Wetzelaer, P. W. M. Blom, *Adv. Opt. Mater.* **2021**, *n/a*, 2100249.

[22] B. van der Zee, Y. Li, G. J. A. H. Wetzelaer, P. W. M. Blom, *Adv. Electron. Mater.* **2022**, *8*.

[23] D. Y. Kondakov, W. C. Lenhart, W. F. Nichols, *J. Appl. Phys.* **2007**, *101*.

[24] D. Abbaszadeh, A. Kunz, G. A. H. Wetzelaer, J. J. Michels, N. I. Craciun, K. Koynov, I. Lieberwirth, P. W. M. Blom, *Nat. Mater.* **2016**, *15*, 628.

[25] M. K. Etherington, N. A. Kukhta, H. F. Higginbotham, A. Danos, A. N. Bismillah, D. R. Graves, P. R. McGonigal, N. Haase, A. Morherr, A. S. Batsanov, C. Pflumm, V. Bhalla, M. R. Bryce, A. P. Monkman, *J. Phys. Chem. C* **2019**, *123*, 11109.

[26] B. van der Zee, Y. Li, G.-J. A. H. Wetzelaer, P. W. M. Blom, accepted for publication in *Phys. Rev. Appl.*

[27] M. A. Baldo, C. Adachi, S. R. Forrest, *Phys. Rev. B - Condens. Matter Mater. Phys.* **2000**, *62*, 10967.

[28] H. J. Lee, H. L. Lee, S. H. Han, J. Y. Lee, *J. Chem. Eng.* **2022**, *427*, 130988.

[29] H. Noda, H. Nakanotani, C. Adachi, *Sci. Adv.* **2018**, *4*, 1.

[30] H. Nakanotani, K. Masui, J. Nishide, T. Shibata, C. Adachi, *Sci. Rep.* **2013**, *3*, 1.

[31] N. B. Kotadiya, P. W. M. Blom, G.-J. A. H. Wetzelaer, *Nat. Photonics* **2019**, 1.

[32] M. Tanaka, H. Noda, H. Nakanotani, C. Adachi, *Adv. Electron. Mater.* **2019**, *5*, 1.

[33] R. Mac Ciarnáin, H. W. Mo, K. Nagayoshi, H. Fujimoto, K. Harada, R. Gehlhaar, T. H. Ke, P. Heremans, C. Adachi, *Adv. Mater.* **2022**, *34*.

Chapter details

Publication

This chapter is based on the publication:

Bas van der Zee, Yungui Li, Gert-Jan A. H. Wetzelaer and Paul W. M. Blom, Triplet-Polaron Annihilation Induced Degradation of Organic Light-Emitting Diodes Based on Thermally Activated Delayed Fluorescence, *accepted for publication in Phys. Rev. Applied*.

Author contributions

B. v. d. Zee and Y. Li made the devices and performed the experiments. Y. Li made the long lifetime device. B. v. d. Zee wrote the code for the degradation model and performed the simulations. B. v. d. Zee wrote the manuscript with input from the co-authors. Gert-Jan A. H. Wetzelaer and P. W. M. Blom supervised the project.

Appendix A: Rate equation derivations

Parameters:

[S]/[T] = singlet/triplet density [m^{-3}]

τ_s/τ_t = singlet/triplet lifetime [s]

G = generation rate [$m^3\ s^{-1}$]

k_{ISC} = ISC rate [s^{-1}]

k_{rISC} = RISC rate [s^{-1}]

k_{TTA} = TTA rate constant [$m^3\ s^{-1}$]

k_{TPA} = TPA rate constant [$m^3\ s^{-1}$]

n/p = electron/hole density [m^{-3}]

η = efficiency

A.1 Efficiency of a PLED with TTA (complementary to chapter 3)

The efficiency (η) of an OLED is given by:

$$\eta = \left(\frac{[S(x)]}{\tau_s}\right) \Big/ G(x).$$

With *[S(x)]* the singlet density and *G(x)* the generation rate, the *'x'* represents position dependence. The 'standard' TTA process is represented as:

$$T_1 + T_1 \xrightarrow{3/4 * k_{TTA}} {}^3(TT) \rightarrow S_0 + T_n \rightarrow S_0 + T_1,$$

$$T_1 + T_1 \xrightarrow{1/4 * k_{TTA}} {}^1(TT) \rightarrow S_0 + S_n \rightarrow S_0 + S_1.$$

With *^{3}(TT)* as the triplet intermediate and *^{1}(TT)* as the singlet intermediate, $T_1/S_1/S_0$ as triplet/singlet excited and singlet ground state respectively. k_{TTA} is the triplet-triplet annihilation constant. Here we assume that the triplet state and singlet state intermediate can form with their respective probability of ¾ and ¼. Furthermore we omit the formation of the quantum mechanically allowed quintet state, since its energy is too high to be accessible under room temperature conditions[1].

We start from the rate equation for singlets, and solve it in steady state to get an expression for the singlet density over the singlet lifetime τ_s.

$$\frac{d[S(x,t)]}{dt} = \frac{1}{4} \cdot G(x,t) - \frac{[S(x,t)]}{\tau_s} + \frac{1}{4} \cdot k_{TTA} \cdot [T(x,t)]^2 = 0,$$

$$\frac{[S(x,t)]}{\tau_s} = \frac{1}{4} \cdot G(x,t) + \frac{1}{4} \cdot k_{TTA} \cdot [T(x,t)]^2.$$

With *[T(x,t)]* the triplet density and *'t'* representing time dependence. Using the approximation of a uniform generation rate, it follows directly from the current density as:

$$G = \frac{J}{q \cdot d}.$$

With *J* the current density and *d* the thickness of the device. The only unknown is the triplet density, which we can solve in a similar fashion from the triplet rate equation.

$$\frac{d[T(x,t)]}{dt} = \frac{3}{4} \cdot G(x,t) - \frac{[T(x,t)]}{\tau_t} - \frac{5}{4} \cdot k_{TTA} \cdot [T(x,t)]^2 = 0,$$

$$[T(x,t)]^2 + \frac{4 \cdot [T(x,t)]}{5 \cdot k_{TTA} \cdot \tau_t} - \frac{4 \cdot 0.75 \cdot G(x)}{5 \cdot k_{TTA}} = 0.$$

With τ_t the triplet lifetime. This has the positive valued solution:

$$[T(x)] = \frac{-2 \cdot \tau_t^{-1}}{5 \cdot k_{TTA}} + \sqrt{4 \cdot \left(\frac{\tau_t^{-1}}{5 \cdot k_{TTA}}\right)^2 + 4 \cdot \frac{0.75 \cdot G(x)}{5 \cdot k_{TTA}}}.$$

The maximum efficiency is reached when no triplets decay via phosphorescence. Mathematically this is implemented in the expression for the triplet density as $\tau_t \to \infty$. The triplet density then reduces to:

$$[T(x)] = \sqrt{4 \cdot \frac{0.75 \cdot G(x)}{5 \cdot k_{TTA}}}.$$

From which the maximum efficiency follows as:

$$\eta_{max} = 0.25 + 0.15 = 0.4.$$

Alternatively, we can show that triplet fusion increases this efficiency to 62.5%. Triplet fusion is represented as:

$$T_1 + T_1 \to S_1 + S_0.$$

Here we assume here that the triplet state intermediate cannot form or its pathway is deactivated. This specific condition can occur if the triplet intermediate is lower than T_2, in which case the intermediate will dissociate again into $2T_1$. This situation is found for example in rubrene or particular anthracene derivatives[2,3].

From which it follows that:

$$\frac{d[S(x,t)]}{dt} = \frac{1}{4} \cdot G(x,t) - \frac{[S(x,t)]}{\tau_s} + k_{TTAUPC} \cdot [T(x,t)]^2 = 0,$$

$$\frac{[S(x,t)]}{\tau_s} = \frac{1}{4} \cdot G(x,t) + k_{TTAUPC} \cdot [T(x,t)]^2,$$

$$\frac{d[T(x,t)]}{dt} = \frac{3}{4} \cdot G(x,t) - \frac{[T(x,t)]}{\tau_t} - 2 \cdot k_{TTAUPC} \cdot [T(x,t)]^2 = 0,$$

$$[T(x,t)]^2 + \frac{[T(x,t)]}{2 \cdot k_{TTAUPC} \cdot \tau_t} - \frac{0.75 \cdot G(x)}{2 \cdot k_{TTAUPC}} = 0,$$

$$[T(x)] = \frac{-\tau_t^{-1}}{2 \cdot k_{TTAUPC}} + \sqrt{\frac{1}{16}\left(\frac{\tau_t^{-1}}{k_{TTAUPC}}\right)^2 + \frac{0.75 \cdot G(x)}{2 \cdot k_{TTAUPC}}}.$$

If every triplet gets upconverted ($\tau_t \to \infty$), the expression for the triplet density becomes:

$$[T(x)] = \sqrt{\frac{0.75 \cdot G(x)}{2 \cdot k_{TTAUPC}}}.$$

From which the maximum efficiency is given by:

$$\eta_{max} = 0.25 + 0.375 = 0.625.$$

A.2 Efficiency of a TADF OLED, simplified (complementary to chapter 4)

Analytical efficiency with TTA, excluding ISC

We start from the rate equation of the singlet population.

$$\frac{d[S]}{dt} = 0.25 \cdot G - \frac{[S]}{\tau_s} + k_{rISC} \cdot [T] = 0,$$

$$\frac{[S]}{\tau_s} = 0.25 \cdot G + k_{rISC} \cdot [T].$$

For the second term in the expression above, we need an expression of the triplet density, which we derive from the rate equation for triplets.

$$\frac{d[T]}{dt} = 0.75 \cdot G - \frac{[T]}{\tau_t} - k_{rISC} \cdot [T] - k_{TTA} \cdot [T] \cdot [T] = 0,$$

$$0.75 \cdot G - \frac{[T]}{\tau_t} - k_{rISC} \cdot [T] - k_{TTA} \cdot [T] \cdot [T] = 0.$$

This quadratic equation can be slightly re-written and solved.

$$[T]^2 + \left(\frac{1 + k_{rISC} \cdot \tau_t}{k_{TTA} \cdot \tau_t}\right)[T] - \frac{0.75 \cdot G}{k_{TTA}} = 0.$$

With the positive valued solution given by:

$$[T] = -\frac{1 + k_{rISC} \cdot \tau_t}{2 k_{TTA} \cdot \tau_t} + \sqrt{\frac{1}{4} \cdot \left(\frac{1 + k_{rISC} \cdot \tau_t}{k_{TTA} \cdot \tau_t}\right)^2 + \frac{0.75 \cdot G}{k_{TTA}}}.$$

We assume that $\tau_t \to \infty$ such that the solution simplifies to:

$$[T] = -\frac{k_{rISC}}{2k_{TTA}} + \sqrt{\frac{1}{4}\cdot\left(\frac{k_{rISC}}{k_{TTA}}\right)^2 + \frac{0.75\cdot G}{k_{TTA}}}.$$

Re-arranging terms we obtain:

$$[T] = \frac{k_{rISC}}{2k_{TTA}}\left(-1 + \sqrt{1 + \frac{4k_{TTA}\cdot 0.75G}{k_{rISC}^2}}\right).$$

Substituting this in the equation for this singlet decay rate we obtain our final expression for the efficiency as:

$$\eta = \frac{\frac{[S]}{\tau_s}}{G} = 0.25 + \frac{k_{rISC}^2}{2k_{TTA}\cdot G}\left(-1 + \sqrt{1 + \frac{4k_{TTA}\cdot 0.75\cdot G}{k_{rISC}^2}}\right).$$

Analytical efficiency with TPA

We start again from the rate equation of singlets, and work our way to an expression of the efficiency, where we consider the influence of TPA.

$$\frac{d[S]}{dt} = 0.25\cdot G - \frac{[S]}{\tau_s} + k_{rISC}\cdot[T] = 0,$$

$$\frac{[S]}{\tau_s} = 0.25\cdot G + k_{rISC}\cdot[T].$$

The rate equation for triplet reads:

$$\frac{d[T]}{dt} = 0.75\cdot G - \frac{[T]}{\tau_t} - k_{rISC}\cdot[T] - k_{TPA}\cdot[T]\cdot(n+p) = 0.$$

With k_{TPA} being the TPA rate constant [$m^3\ s^{-1}$] and *n/p* the electron and hole density respectively [m^{-3}].

$$\left(\frac{1}{\tau_t} + k_{rISC} + k_{TPA}\cdot(n+p)\right)[T] = 0.75\cdot G.$$

With the assumption that $\tau_t \to \infty$ we obtain for the triplet density:

$$[T] = \frac{0.75\cdot G}{k_{rISC} + k_{TPA}\cdot(n+p)}.$$

Using the expression for the triplet density we can derive an analytical expression for the efficiency, which reads:

$$\eta = \frac{\frac{[S]}{\tau_s}}{G} = 0.25 + \frac{k_{rISC}}{k_{rISC} + k_{TPA}\cdot(n+p)}.$$

Analytical efficiency with STA

The influence of STA is included in the rate equation for singlets as follows:

$$\frac{d[S]}{dt} = 0.25 \cdot G - \frac{[S]}{\tau_s} + k_{rISC} \cdot [T] - k_{STA} \cdot [S] \cdot [T] = 0,$$

$$0.25 \cdot G - \frac{[S]}{\tau_s} + k_{rISC} \cdot [T] - k_{STA} \cdot [S] \cdot [T] = 0.$$

With k_{STA} being the singlet-triplet annihilation constant [$m^3\ s^{-1}$]. The rate equation for triplets reads:

$$\frac{d[T]}{dt} = 0.75 \cdot G - \frac{[T]}{\tau_t} - k_{rISC} \cdot [T] = 0.$$

With $\tau_t \to \infty$ the triplet density becomes:

$$[T] = \frac{0.75 \cdot G}{k_{rISC}}.$$

With this expression for the triplet density, the efficiency can be deduced as follows:

$$0.25 \cdot G - \frac{[S]}{\tau_s} + k_{rISC} \cdot \frac{0.75 \cdot G}{k_{rISC}} - k_{STA} \cdot [S] \cdot \frac{0.75 \cdot G}{k_{rISC}} = 0,$$

$$G - \frac{[S]}{\tau_s} - k_{STA} \cdot [S] \cdot \frac{0.75 \cdot G}{k_{rISC}} = 0,$$

$$[S]\left(\frac{1}{\tau_s} + k_{STA} \cdot \frac{0.75 \cdot G}{k_{rISC}}\right) = G,$$

$$\eta = \frac{\frac{[S]}{\tau_s}}{G} = \frac{1}{1 + \frac{k_{STA} \cdot \tau_s \cdot 0.75 \cdot G}{k_{rISC}}}.$$

Analytical efficiency with TTA, including ISC

We start again from the rate equation of the singlet density, now with a term including ISC.

$$\frac{d[S]}{dt} = 0.25 \cdot G - \frac{[S]}{\tau_s} + k_{rISC} \cdot [T] - k_{ISC} \cdot [S] = 0.$$

Through ISC, we have an extra dependence on [S] in the expression above. The singlet density than becomes:

$$[S] = \frac{0.25 \cdot \tau_s \cdot G + k_{rISC} \cdot \tau_s \cdot [T]}{1 + k_{ISC} \cdot \tau_s}.$$

The rate equation for triplets now reads:

$$\frac{d[T]}{dt} = 0.75 \cdot G - \frac{[T]}{\tau_t} - k_{rISC} \cdot [T] + k_{ISC} \cdot [S] - k_{TTA} \cdot [T] \cdot [T] = 0.$$

We will now work our way to an expression for the triplet density. Because of the extra dependence on the singlet density through ISC, we will insert the expression for [S] in the rate equation for the triplet density and solve it. Again with $\tau_t \to \infty$ we obtain after some algebraic manipulation:

$$\frac{d[T]}{dt} = \frac{-0.75 \cdot G}{k_{TTA}} + \frac{k_{rISC}}{k_{TTA}} \cdot [T] - \frac{0.25 \cdot G \cdot \tau_s \cdot k_{ISC}}{k_{TTA} + k_{TTA} \cdot k_{ISC} \cdot \tau_s} - \frac{k_{ISC} \cdot k_{rISC} \cdot \tau_s \cdot [T]}{k_{TTA} + k_{TTA} \cdot k_{ISC} \cdot \tau_s} + [T] \cdot [T] = 0.$$

Grouping terms with $[T]^2$, [T], and G we are eventually left with:

$$[T]^2 + \frac{k_{rISC}}{k_{TTA}+k_{TTA}\cdot k_{ISC}\cdot\tau_s}[T] - \frac{0.75+k_{ISC}\cdot\tau_s}{k_{TTA}+k_{TTA}\cdot k_{ISC}\cdot\tau_s}G = 0.$$

Which has a positive valued solution for the triplet density, given by:

$$[T] = -\frac{k_{rISC}}{2(k_{TTA}+k_{TTA}\cdot k_{ISC}\cdot\tau_s)} + \sqrt{\frac{1}{4}\cdot\left(\frac{k_{rISC}}{k_{TTA}+k_{TTA}\cdot k_{ISC}\cdot\tau_s}\right)^2 + \frac{0.75\cdot G+k_{ISC}\cdot\tau_s\cdot G}{k_{TTA}+k_{TTA}\cdot k_{ISC}\cdot\tau_s}}.$$

Note that the solution above simplifies to the solution of the triplet density without ISC (see '*Derivation of the analytical efficiency with TTA*') if k_{ISC} is set to 0. The efficiency is again given by:

$$\eta = \frac{\frac{[S]}{\tau_S}}{G}.$$

A.3 Rate equations for TADF OLEDs, comprehensive (complementary to chapter 5)

No quenching

We start with the rate equation for singlets with the dynamics appropriate to TADF:

$$\frac{d[S(x,t)]}{dt} = 0.25\cdot G(x,t) - \frac{[S(x,t)]}{\tau_s} + k_{rISC}\cdot[T(x,t)] - k_{ISC}\cdot[S(x,t)].$$

Which we can solve in steady state (=0) to obtain an expression for the singlet density.

$$[S(x)] = \frac{0.25\cdot G(x)+[T(x)]\cdot k_{rISC}}{\tau_s^{-1}+k_{ISC}}.$$

Similarly, the rate equation for triplets reads:

$$\frac{d[T(x,t)]}{dt} = 0.75\cdot G(x,t) - \frac{[T(x,t)]}{\tau_t} - k_{rISC}\cdot[T(x,t)] + k_{ISC}\cdot[S(x,t)].$$

Which has the solution:

$$[T(x)] = \frac{k_{ISC}\cdot G(x)\cdot\tau_s+0.75\cdot G(x)}{\tau_t^{-1}+k_{ISC}\cdot\tau_s\cdot\tau_t^{-1}+k_{rISC}}.$$

TTA

We start with the rate equation for singlets, and work our way to an expression for the singlet density.

$$\frac{d[S(x,t)]}{dt} = 0.25\cdot G(x,t) - \frac{[S(x,t)]}{\tau_s} + k_{rISC}\cdot[T(x,t)] - k_{ISC}\cdot[S(x,t)] + 0.25\cdot k_{TTA}\cdot [T(x,t)]^2.$$

In steady state, in which we measure our device, we can equate this rate equation to 0, and solve the equation for $[S(x,t)]$.

$$\left(\frac{1}{\tau_s} + k_{ISC}\right)[S(x)] = 0.25 \cdot G(x) + k_{rISC} \cdot [T(x)] + 0.25 \cdot k_{TTA} \cdot [T(x)]^2,$$

$$[S(x)] = \frac{0.25 \cdot \tau_s \cdot G(x) + k_{rISC} \cdot \tau_s \cdot [T(x)] + 0.25 \cdot k_{TTA} \cdot \tau_s \cdot [T(x)]^2}{1 + k_{ISC} \cdot \tau_s}.$$

The rate equation for triplet reads:

$$\frac{d[T(x,t)]}{dt} = 0.75 \cdot G(x,t) - \frac{[T(x,t)]}{\tau_t} - k_{rISC} \cdot [T(x,t)] + k_{ISC} \cdot [S(x,t)] - 1.25 \cdot k_{TTA} \cdot [T(x,t)]^2.$$

We can fill in our expression for the singlet density, and separate the terms according to their power of $[T(x,t)]$.

$$\frac{d[T(x,t)]}{dt} = 0.75 \cdot G(x,t) - \frac{[T(x,t)]}{\tau_t} - k_{rISC} \cdot [T(x,t)] + \frac{0.25 \cdot k_{ISC} \cdot \tau_s \cdot G(x)}{1 + k_{ISC} \cdot \tau_s} + \frac{k_{rISC} \cdot k_{ISC} \cdot \tau_s \cdot [T(x)]}{1 + k_{ISC} \cdot \tau_s} + \frac{0.25 \cdot k_{ISC} \cdot k_{TTA} \cdot \tau_s \cdot [T(x)]^2}{1 + k_{ISC} \cdot \tau_s} - 1.25 \cdot k_{TTA} \cdot [T(x,t)]^2.$$

We multiply by $(-1.25 \cdot k_{TTA})^{-1}$, and collect several terms with the denominator of $5 \cdot k_{TTA} + 5 \cdot k_{TTA} \cdot k_{ISC} \cdot \tau_s$. After some algebraic manipulation we obtain:

$$\frac{d[T(x,t)]}{dt} = \left(\frac{5 \cdot k_{TTA} + 4 \cdot k_{TTA} \cdot k_{ISC} \cdot \tau_s}{5 \cdot k_{TTA} + 5 \cdot k_{TTA} \cdot k_{ISC} \cdot \tau_s}\right)[T(x,t)]^2 + \left(\frac{4 \cdot \tau_t^{-1} + 4 \cdot k_{ISC} \cdot \tau_s \cdot \tau_t^{-1} + 4 \cdot k_{rISC}}{5 \cdot k_{TTA} + 5 \cdot k_{TTA} \cdot k_{ISC} \cdot \tau_s}\right)[T(x,t)] - \left(\frac{4 \cdot 0.75 + 4 \cdot k_{ISC} \cdot \tau_s}{5 \cdot k_{TTA} + 5 \cdot k_{TTA} \cdot k_{ISC} \cdot \tau_s}\right) G(x,t).$$

We multiply by the inverse of the first term in front of $[T(x,t)]^2$.

$$\frac{d[T(x,t)]}{dt} = [T(x,t)]^2 + \left(\frac{4 \cdot \tau_t^{-1} + 4 \cdot k_{ISC} \cdot \tau_s \cdot \tau_t^{-1} + 4 \cdot k_{rISC}}{5 \cdot k_{TTA} + 4 \cdot k_{TTA} \cdot k_{ISC} \cdot \tau_s}\right)[T(x,t)] - \left(\frac{4 \cdot 0.75 + 4 \cdot k_{ISC} \cdot \tau_s}{5 \cdot k_{TTA} + 4 \cdot k_{TTA} \cdot k_{ISC} \cdot \tau_s}\right) G(x,t).$$

In steady state we can equate this to 0, and the resulting quadratic equation has a positive valued solution for the triplet density given by:

$$[T(x)] = -2\frac{\tau_t^{-1} + k_{ISC} \cdot \tau_s \cdot \tau_t^{-1} + k_{rISC}}{5 \cdot k_{TTA} + 4 \cdot k_{TTA} \cdot k_{ISC} \cdot \tau_s} + \sqrt{4 \cdot \left(\frac{\tau_t^{-1} + k_{ISC} \cdot \tau_s \cdot \tau_t^{-1} + k_{rISC}}{5 \cdot k_{TTA} + 4 \cdot k_{TTA} \cdot k_{ISC} \cdot \tau_s}\right)^2 + 4 \cdot \frac{0.75 \cdot G(x) + k_{ISC} \cdot \tau_s \cdot G(x)}{5 \cdot k_{TTA} + 4 \cdot k_{TTA} \cdot k_{ISC} \cdot \tau_s}}.$$

TPA

We can follow a similar procedure for TPA where we start from the rate equation for singlets.

$$\frac{d[S(x,t)]}{dt} = 0.25 \cdot G(x,t) - \frac{[S(x,t)]}{\tau_s} + k_{rISC} \cdot [T(x,t)] - k_{ISC} \cdot [S(x,t)].$$

Where in steady state the solution for the singlet density is given by:

$$[S(x)] = \frac{0.25 \cdot \tau_s \cdot G(x) + k_{rISC} \cdot \tau_s \cdot [T(x)]}{1 + k_{ISC} \cdot \tau_s}.$$

The rate equation for triplets in the presence of TPA reads:

$$\frac{d[T(x,t)]}{dt} = 0.75 \cdot G(x,t) - \frac{[T(x,t)]}{\tau_t} - k_{rISC} \cdot [T(x,t)] + k_{ISC} \cdot [S(x,t)] - k_{TPA} \cdot \big(n(x) + p(x)\big) \cdot [T(x,t)] = 0.$$

We fill in the expression for the singlet density, and separate the terms again, now on the one hand we have terms connected to $[T(x)]$ and on the other hand terms in $G(x)$.

$$\left(-\tau_t^{-1} - k_{TPA} \cdot \big(n(x) + p(x)\big) + \frac{k_{rISC} \cdot k_{ISC} \cdot \tau_s}{1 + k_{ISC} \cdot \tau_s} - k_{rISC}\right)[T(x)] = \left(-0.75 - \frac{0.25 \cdot k_{ISC} \cdot \tau_s}{1 + k_{ISC} \cdot \tau_s}\right) G(x).$$

We can write everything as one fraction. After some rearrangement we obtain:

$$\left(\frac{k_{rISC} + \tau_t^{-1} + k_{ISC} \cdot \tau_s \cdot \tau_t^{-1} + k_{TPA} \cdot \big(n(x)+p(x)\big) + k_{TPA} \cdot \big(n(x)+p(x)\big) \cdot k_{ISC} \cdot \tau_s}{1 + k_{ISC} \cdot \tau_s}\right)[T(x)] = \frac{k_{ISC} \cdot \tau_s \cdot G(x) + 0.75 \cdot G(x)}{1 + k_{ISC} \cdot \tau_s}.$$

The expression for the triplet density is therefore:

$$[T(x)] = \frac{k_{ISC} \cdot \tau_s \cdot G(x) + 0.75 \cdot G(x)}{k_{rISC} + \tau_t^{-1} + k_{ISC} \cdot \tau_s \cdot \tau_t^{-1} + \Big(k_{TPA} \cdot \big(n(x)+p(x)\big)\Big) \cdot (1 + \cdot k_{ISC} \cdot \tau_s)}.$$

STA

For STA, the roll-off term appears in the rate equation for singlets, which is given by:

$$\frac{d[S(x,t)]}{dt} = 0.25 \cdot G(x,t) - \frac{[S(x,t)]}{\tau_s} + k_{rISC} \cdot [T(x,t)] - k_{ISC} \cdot [S(x,t)] - k_{STA} \cdot [S(x,t)] \cdot [T(x,t)].$$

In steady state this gives the following solution:

$$[S(x)] = \frac{0.25 \cdot \tau_s \cdot G(x) + k_{rISC} \cdot \tau_s \cdot [T(x)]}{1 + k_{ISC} \cdot \tau_s + k_{STA} \cdot \tau_s \cdot [T(x)]}.$$

We can again fill in the expression for the singlet density in the triplet rate equation and solve it in steady state for the triplet density.

$$\frac{d[T(x,t)]}{dt} = 0.75 \cdot G(x,t) - \frac{[T(x,t)]}{\tau_t} - k_{rISC} \cdot [T(x,t)] + k_{ISC} \cdot [S(x,t)].$$

$$\frac{d[T(x,t)]}{dt} = 0.75 \cdot G(x,t) - \frac{[T(x,t)]}{\tau_t} - k_{rISC} \cdot [T(x,t)] + \frac{0.25 \cdot \tau_s \cdot k_{ISC} \cdot G(x)}{1 + k_{ISC} \cdot \tau_s + k_{STA} \cdot \tau_s \cdot [T(x)]} + \frac{k_{rISC} \cdot k_{ISC} \cdot \tau_s \cdot [T(x)]}{1 + k_{ISC} \cdot \tau_s + k_{STA} \cdot \tau_s \cdot [T(x)]} = 0.$$

Multiplying by $(1 + k_{ISC} \cdot \tau_s + k_{STA} \cdot \tau_s \cdot [T(x)])$ and grouping terms we arrive at:

$$(k_{rISC} \cdot k_{STA} \cdot \tau_s + \tau_s \cdot \tau_t^{-1} \cdot k_{STA})[T(x)]^2 + (-0.75 \cdot G(x) \cdot k_{STA} \cdot \tau_s + \tau_t^{-1} + \tau_s \cdot \tau_t^{-1} \cdot k_{ISC} + k_{rISC})[T(x)] - (k_{ISC} \cdot \tau_s + 0.75) G(x) = 0,$$

$$[T(x)]^2 + \left(\frac{-0.75 \cdot G(x) \cdot k_{STA} \cdot \tau_s + \tau_t^{-1} + \tau_s \cdot \tau_t^{-1} \cdot k_{ISC} + k_{rISC}}{k_{rISC} \cdot k_{STA} \cdot \tau_s + \tau_s \cdot \tau_t^{-1} \cdot k_{STA}}\right)[T(x)] - \left(\frac{k_{ISC} \cdot \tau_s + 0.75}{k_{rISC} \cdot k_{STA} \cdot \tau_s + \tau_s \cdot \tau_t^{-1} \cdot k_{STA}}\right) G(x) = 0.$$

This has the positive valued solution:

$$[T(x)] = -\frac{1}{2}\left(\frac{-0.75\cdot G(x)\cdot k_{STA}\cdot\tau_s+\tau_t^{-1}+\tau_s\cdot\tau_t^{-1}\cdot k_{ISC}+k_{rISC}}{k_{rISC}\cdot k_{STA}\cdot\tau_s+\tau_s\cdot\tau_t^{-1}\cdot k_{STA}}\right) + \sqrt{\frac{1}{4}\left(\frac{-0.75\cdot G(x)\cdot k_{STA}\cdot\tau_s+\tau_t^{-1}+\tau_s\cdot\tau_t^{-1}\cdot k_{ISC}+k_{rISC}}{k_{rISC}\cdot k_{STA}\cdot\tau_s+\tau_s\cdot\tau_t^{-1}\cdot k_{STA}}\right)^2 + \left(\frac{k_{ISC}\cdot\tau_s+0.75}{k_{rISC}\cdot k_{STA}\cdot\tau_s+\tau_s\cdot\tau_t^{-1}\cdot k_{STA}}\right) G(x)}.$$

Appendix B: Complementary information for chapter 3, trap formation pathways

Monomolecular pathway

The number of excitons created per unit time due to Langevin recombination (*L(t)*) will provide the light output and for a monomolecular pathway, they will act as the instigator of hole trap formation. During aging, L(t) has to be corrected with an efficiency factor due to the presence of SRH recombination. Since the Langevin recombination rate scales with the hole density (*p*), and the SRH recombination scales with the hole trap density (P_t), we obtain for *L(t)*:

$$L(t) \propto J * \frac{p(t)}{p(t) + P_t(t)}.$$

For long aging times we make the simplification that $P_t >> p$, and for a PLED in the SCLC regime we know that $p \sim J^{1/2}$, thus we can write *L(t)* as:

$$L(t) \propto \frac{J^{\frac{3}{2}}}{P_t(t)}.$$

For a monomolecular pathway, the rate of trap formation can be written as:

$$\frac{dP_t}{dt} \propto L(t) \propto \frac{J^{3/2}}{P_t(t)},$$

$$\frac{dP_t}{dt} = \gamma' \frac{J^{3/2}}{P_t(t)}.$$

Where γ is a proportionality constant that will indicate how fast the trap formation proceeds. We can integrate the last expression to find an expression for P_t.

$$\int P_t(t)\, dP_t = \int \gamma' J^{3/2}\, dt,$$

$$\frac{1}{2} P_t^2 = \gamma' J^{3/2}\, t.$$

Where the integration constant is 0, since at t = 0 s we do not have hole traps. Here $\gamma = \sqrt{2\gamma'}$. It follows that:

$$P_t = \gamma J^{3/4} \sqrt{t}.$$

Exciton-Exciton interaction

Following the same derivation as presented above we arrive at an expression for the rate of trap formation as:

$$\frac{dP_t}{dt} \propto L(t) * L(t) \propto \frac{J^3}{P_t^2(t)}.$$

$$\frac{dP_t}{dt} = \beta' \frac{J^3}{P_t^2(t)}.$$

$$\int P_t^2(t)\, dP_t = \int \beta' J^3\, dt.$$

$$\frac{1}{3} P_t^3 = \beta' J^3\, t.$$

$$P_t = \beta J\, t^{1/3}.$$

Where $\beta = (3\beta')^{1/3}$.

Appendix C: Complementary information to chapter 5, TrPL analysis

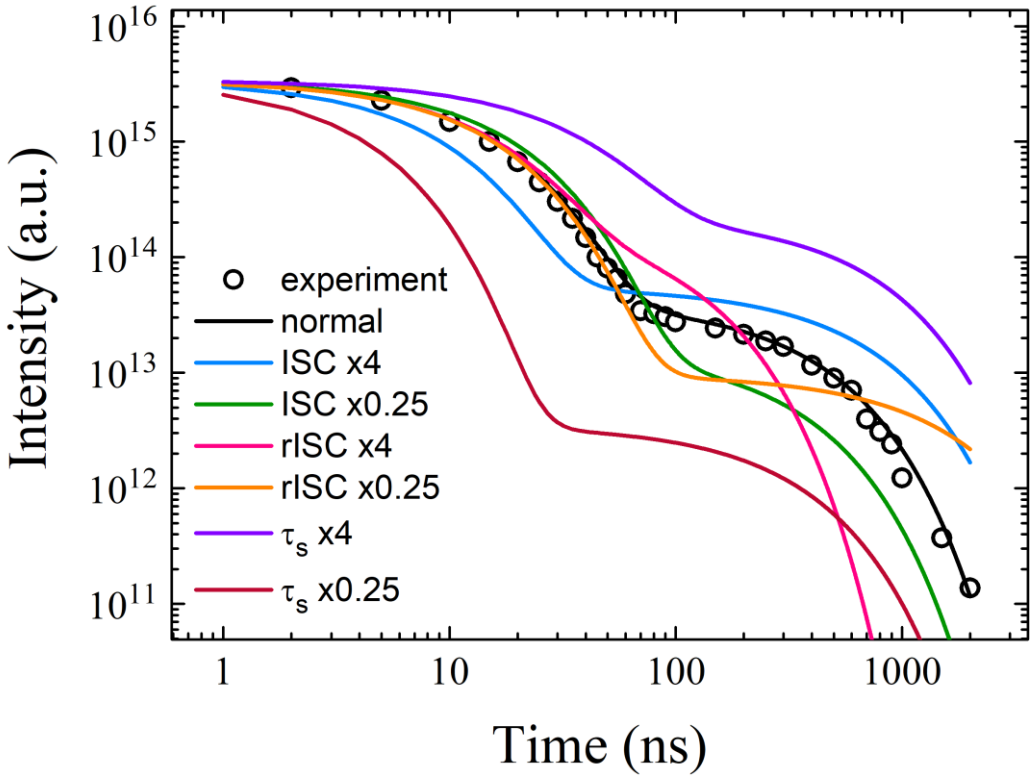

Figure C.1: Influence of various photophysical parameters on the TrPL decay of 4CzIPN in solution.

Appendix C details:

Kai Philipps measured the TrPL of 4CzIPN in solution.

List of Publications

1. Thakur, K., **van der Zee, B.**, Sachnik, O., Constantin, H., Graf, R., Michels, J., Wetzelaer, G.-J. A. H., Ramanan, C., Blom, P. W. M., Effect of tert-butylation group on the photophysics of solution processable thermally activated delayed fluorescent emitters. (*Manuscript under prepration*)

2. Wu, Y, **van der Zee, B** et al. Reduced bimolecular charge recombination in efficient organic solar cells comprising non-fullerene acceptors (*Manuscript submitted)*

3. **Bas van der Zee**, Yungui Li, Gert-Jan A. H. Wetzelaer and Paul W. M. Blom, Triplet-polaron annihilation induced degradation of organic light-emitting diodes based on thermally activated delayed fluorescence. (*Manuscript accepted at Phys. Rev. Appl.*)

4. Philipps, K., Ie, Y., **van der Zee, B.**, Png, R.-Q., Ho, P. K. H., Chua, L.-L., del Pino, E., Ramanan, C., Wetzelaer, G.-J. A. H., Blom, P. W. M., Michels, J. J., Role of Linker Functionality in Polymers Exhibiting Main-Chain Thermally Activated Delayed Fluorescence. *Adv. Sci.* 2022, 2200056.

5. **van der Zee, B.**, Li, Y., Wetzelaer, G.-J. A. H., Blom, P. W. M., Numerical Device Model for Organic Light-Emitting Diodes Based on Thermally Activated Delayed Fluorescence. Adv. Electron. Mater. 2022, 2101261.

6. **Van der Zee, B.**, Li, Y., Wetzelaer, G.-J. A. H., Blom, P. W. M., Efficiency of Polymer Light-Emitting Diodes: A Perspective. Adv. Mater. 2022, 2108887.

7. Thakur, K., **van der Zee, B.**, Wetzelaer, G.-J. A. H., Ramanan, C., Blom, P. W. M., Quantifying Exciton Annihilation Effects in Thermally Activated Delayed Fluorescence Materials. *Adv. Optical Mater.* 2022, 10, 2101784.

8. Li, Y., **van der Zee, B.**, Wetzelaer, G.-J. A. H., Blom, P. W. M., Optical Outcoupling Efficiency in Polymer Light-Emitting Diodes. Adv. Electron. Mater. 2021, 7, 2100155.

9. Li, Y., Kotadiya, N. B., **van der Zee, B.**, Blom, P. W. M., Wetzelaer, G.-J. A. H., Optical Outcoupling Efficiency of Organic Light-Emitting Diodes with a Broad Recombination Profile. Adv. Optical Mater. 2021, 9, 2001812.

10. Li, Y., Sachnik, O., **van der Zee, B.**, Thakur, K., Ramanan, C., Wetzelaer, G.-J. A. H., Blom, P. W. M., Universal Electroluminescence at Voltages below the Energy Gap in Organic Light-Emitting Diodes. Adv. Optical Mater. 2021, 9, 2101149.

11. **Van der Zee, B.**, Li, Y., Wetzelaer, G.-J. A. H., Blom, P. W. M., Origin of the Efficiency Roll-Off in Single-Layer Organic Light-Emitting Diodes Based on Thermally Activated Delayed Fluorescence. Adv. Optical Mater. 2021, 9, 2100249.

12. Anirban Mondal, Leanne Paterson, Jaeyoung Cho, Kun-Han Lin, **Bas van der Zee**, Gert-Jan A. H. Wetzelaer, Andrei Stankevych, Alexander Vakhnin, Jang-Joo Kim, Andrey Kadashchuk, Paul W. M. Blom, Falk May, and Denis Andrienko, "Molecular library of OLED host materials—Evaluating the multiscale simulation workflow", Chem. Phys. Rev. 2, 031304 (2021).

13. Jian Liu, **Bas Van der Zee**, Diego R. Villava, Gang Ye, Simon Kahmann, Max Kamperman, Jingjin Dong, Li Qiu, Giuseppe Portale, Maria Antonietta Loi, Jan C. Hummelen, Ryan C. Chiechi, Derya Baran, and L. Jan Anton Koster, Molecular Doping Directed by a Neutral Radical, ACS Applied Materials & Interfaces 2021 13 (25), 29858-29865.

14. **van der Zee, B.**, Paulus, S., Png, R.-Q., Ho, P. K. H., Chua, L.-L., Wetzelaer, G.-J. A. H., Blom, P. W. M., Role of Singlet and Triplet Excitons on the Electrical Stability of Polymer Light-Emitting Diodes. Adv. Electron. Mater. 2020, 6, 2000367.

15. G. Ricciardulli, **B. van der Zee**, K. Philipps, G. A. H. Wetzelaer, R.-Q. Png, P. K. H. Ho, L.-L. Chua, and Paul W. M. Blom, "Polymer–perovskite blend light-emitting diodes using a self-compensated heavily doped polymeric anode", APL Materials 8, 021101 (2020).

16. Anielen H. Ribeiro, Ahmed Fakih, **Bas van der Zee**, Lothar Veith, Gunnar Glaser, Alexander Kunz, Katharina Landfester, Paul W. M. Blom and Jasper J. Michels, Green and stable processing of organic light-emitting diodes from aqueous nanodispersions, J. Mater. Chem. C, 2020,8, 6528-6535 .

17. Rörich, I., Niu, Q., **van der Zee, B.**, del Pino, E., Crăciun, N. I., Ramanan, C., Blom, P. W. M., Exciton Quenching due to Hole Trap Formation in Aged Polymer Light-Emitting Diodes. Adv. Electron. Mater. 2020, 6, 1700643.

18. Liu, J., **van der Zee, B.**, Alessandri, R. et al. N-type organic thermoelectrics: demonstration of ZT > 0.3. Nat Commun 11, 5694 (2020).

19. Jian Liu, Matt P. Garman, Jingjin Dong, **Bas van der Zee**, Li Qiu, Giuseppe Portale, Jan C. Hummelen, and L. Jan Anton Koster, Doping Engineering Enables Highly Conductive and Thermally Stable n-Type Organic Thermoelectrics with High Power Factor, ACS Applied Energy Materials 2019 2 (9), 6664-6671.

20. Liu, J., Ye, G., **van der Zee, B.**, Dong, J., Qiu, X., Liu, Y., Portale, G., Chiechi, R. C., Koster, L. J. A., N-Type Organic Thermoelectrics of Donor-Acceptor Copolymers: Improved Power Factor by Molecular Tailoring of the Density of States, Adv. Mater. 2018, 30, 1804290.

Acknowledgements

First, I would like to express my gratidute to my supervisor, Prof. Paul Blom, for the opportunity to do a PhD in his group. The level of supervision I have received from you is outstanding. Despite how busy you were, there was always a fast reply to my questions, manuscripts, and everything else. The same holds for Dr. Gert-Jan Wetzelaer, you were very approachable, answering all my (sometimes basic) questions whenever they came up. I only wish there was a Panda Express in Mainz we could go to.

I would also like to thank AK Blom in general, for welcoming me to the group and making my PhD a truly memorable experience. In particular, Kai and Anie, thank you very much for all the good times, during and outside of work! I'm glad we are keeping in contact. All the amazing coffee breaks I had with you Anie were extremely funny. Also, sharing an office with you, Kai, was fantastic. I will never forget the compelementary ITO substrates and the 'catch me if you can' challenge. Okan, it was great sharing an office with you, we started our PhD around the same time, so I am grateful we got a lot of time that we could spend together.

Petra, you were great help, and it was always nice to chat with you.

Also thanks to the many people who showed me around the labs and provided various trainings. Elham, you basically taught me how to make OLEDs, which is much appreciated.

There are many more MPIP members and people in Mainz that have contributed to my good time here (in no particular order): Constantin, Mateusz, Katharina, Imke, Xiao, Carla, Yue, Pranav, Kaveri, Suthir, Sten, Mohammad, Esther, Franziska, Naresh, Ricardo, Ke, Max, Morteza, Antonio, Oskar, David, Felix, Mahni, and Shuanglong.

Thanks to the technicians and lab supervisors of AK Blom as well: Frank, Christian, Verona, and Michelle. You were always there to fix the setups, and I have had great talks with you.

Ik wil ook graag mijn ouders en zusje bedanken voor hun onvoorwaardelijke steun tijdens mijn tijd hier in Mainz. Hetzelfde geldt natuurlijk voor al mijn familie en vrienden.

Finally, I've met the love of my life here in Mainz. Kalyani, thank you so very much for all the time we've spend here. I'm looking forward to a long and happy life together.

I'm sorry if I forgot anyone.